Aggregation and Charge Transport

in Thin Films of Conjugated Polymers

Anjar Taufik HIDAYAT

2020

Aggregation and charge transport

in thin films of conjugated polymers

Anjar Taufik HIDAYAT

2020

Table of Contents

Chapter 1.

General Introduction

1.1. Background and motivation

Organic semiconductors had been active materials for a wide variety of organic electronics applications such as xerography, organic lasers, electrochromic devices, organic thin-film transistors (OTFTs), organic light-emitting diodes (OLEDs), organic photovoltaics (OPVs), circuit inks, and sensors.[1–7] The wide range of applicability is rooted in its tunable properties in a scale of molecules to a macroscopic device. This tunability brings continuous development in each new class of organic semiconductors from amorphous molecular crystals to conductive polymers. The development of conductive polymers was started from the discovery in 1977 by Heeger, MacDiarmid, and Shirakawa that high conductivity could be attained by using doped π-conjugated polymers.[8] Later, on the 1980s, the importance of the undoped conjugated polymers started to emerge due to excellent stability in air and the charge transporting ability, polythiophene for OTFTs,[9] and polyphenylenevinylene (PPV) for OLEDs.[10]

1.1.1. Microstructures of conjugated polymer

Microstructures of conjugated polymers vary in chain conformations and molecular packing due to the weak bonding and high degree of conformational freedom. This nature of conjugated polymer leads to the coexistence of two distinctive regions, disordered (amorphous) and ordered[11] (**Figure 1-1**). The ordered region can be divided into two categories based on the range, long-range ordered (crystallites/crystalline), or short-range ordered (aggregates/aggregation).

The amorphous regions are the region that only contains disorder chains. Disorder chains are bent chains or entangled between each other chains. Due to its disordered polymer chains. This region has a larger bandgap compared to the ordered one.[11]

The crystallites are the ordered region, which comprises of packs of ordered lamellas. These lamellas are consist of co-facially stacked chains that exhibit π-orbital overlap. The size of crystallites is calculated from the scattering of the X-ray characterization result. The length is about ~~in~~ several to tens of nanometers in π-stacking direction[11,12].

The definition of aggregates is still unclear. Duong et al. suggested that aggregates are defined as π-conjugated segments that do not participate in the lamellar stacking.[13] In the specific report about locally-ordered conjugated polymer, Noriega defined aggregates as ordered structures with a smaller size than crystallites.[12] The agreeable opinion about aggregate is that it consists of a π-conjugated polymer chain segment. Some aggregates ~~which~~ having enough π-conjugated segments can be detected by strong X-ray diffraction peak. Some others give a weak or can not give any diffraction peak. However, both conditions can give a characteristic of photophysical properties, which are different from the disordered chain.[14–16]

1.1.2. Classes of conjugated polymers

Nowadays, conjugated polymers can be classified into three classes based on the film state microstructures: Highly-ordered conjugated polymers, amorphous conjugated polymers, and weakly-ordered conjugated polymers (**Figure 1-1**). Highly-ordered conjugated polymers are a class of polymers which comprise of largely-developed crystallites region. Amorphous conjugated polymers are consist of complete disorder chains. Weakly-ordered conjugated polymers have structural features between amorphous and highly-ordered semicrystalline counterparts. They consist of aggregates and amorphous chains. The weakly-ordered conjugated polymers in this class are based on donor-acceptor copolymer architecture.[12]
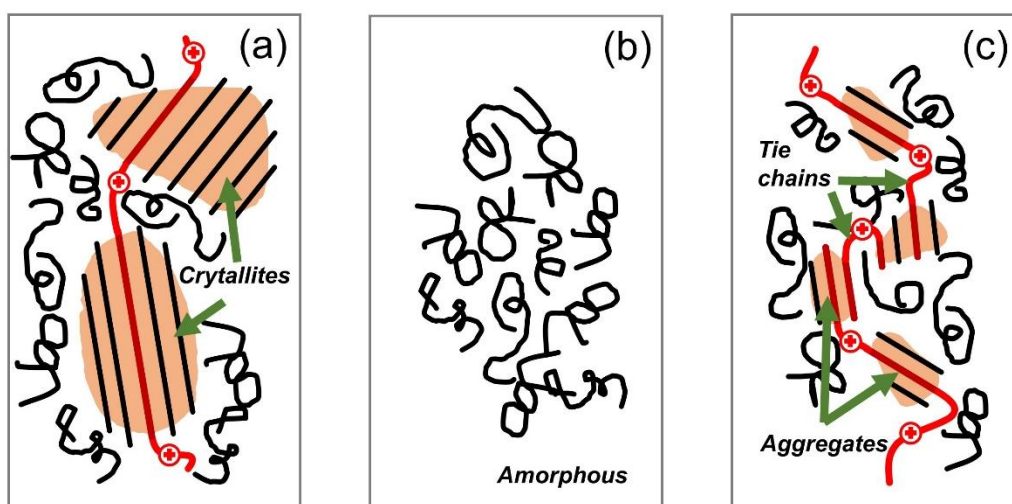
Figure 1-1. Illustration of microstructures of conjugated polymer thin films, (a) Highly-ordered semicrystalline, (b) completely amorphous, and (c) weakly-ordered semicrystalline. When the molecular weight is high enough, and the device contains a high fraction of ordered structure, the long polymer chains (red-solid line) would connect the ordered region without losing conjugation and transporting charges.

1.1.3. Charge transport in conjugated polymers

Charge transport in the ordered region was depicted in **Figure 1-2**. Charge transfer integral is the highest in the chain backbone direction, followed by π-stacking direction, and then it is the lowest in the side-chain direction.[17,18]

If the distance between neighboring order regions is only a few persistence lengths, the chains connecting them should not suffer from large bends and retain conjugation. Such chain segments even lie in the amorphous region and do not belong to one of the ordered regions, act as tie-chains that provide efficient charge transport path between the ordered regions[11] (**Figure 1-1c**).

In the amorphous region, the electronic traps exist as the effect of tilted monomer, significant bent of polymer chains, or from entangled polymer chain. The charges in the trap states need some amount of energy to overcome the energetic barrier between trap states to the conducting states.

Therefore, in the semicrystalline conjugated polymers, the ordered regions are highly responsible for charge transport. Long-range and high-oriented ordered structures are favorable for charge transport in the device scale level.[11]
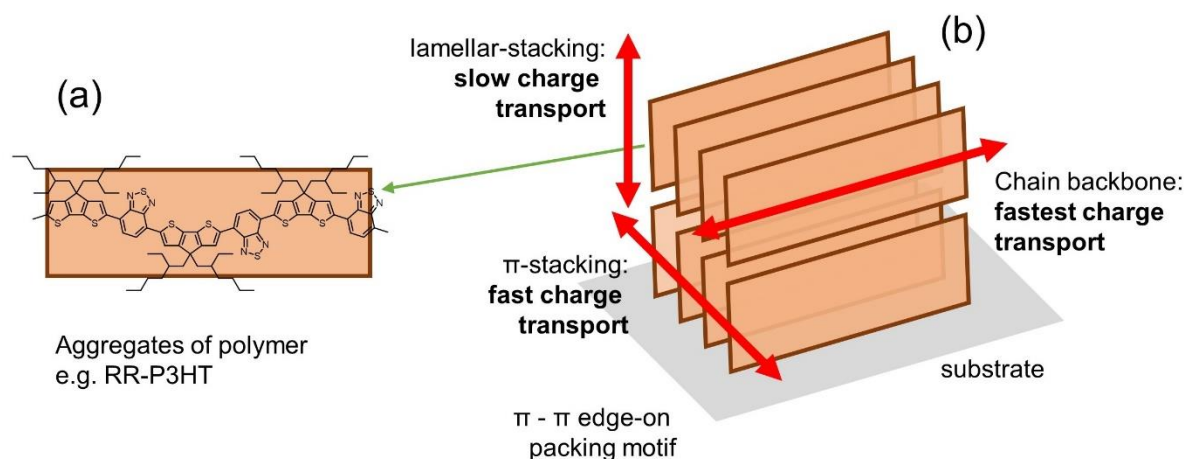
Figure 1-2. Illustration of charge transport in conjugated polymer thin films

1.2. Research purpose

Based on excellent charge transport property in the ordered structure, a class of highly-ordered conjugated polymers shows high charge transport property. On the other hand, some members of the weakly-ordered conjugated polymers class are also shown high charge transport mobility.[12] In this regard, both classes of conjugated polymer with the different microstructure characteristics (long-range order: highly ordered conjugated polymer class, short-range order: weakly-ordered conjugated polymer class) are essential subjects for the development of polymer semiconductors.

A long-time study of the highly-ordered conjugated polymer has resulted in the rich knowledge of the structure-function relationship to improve the charge transport. However, the knowledge and strategies are not directly transferable to the weakly-ordered conjugated polymer systems.[19] For example, the long-range ordered structures must attain high charge

transport in the highly-ordered conjugated polymer. However, short-range ordered structures, which are characteristic for weakly-ordered conjugated polymers, were also proved to support high charge transport.[20] Why and how the short-range ordered structures can support efficient charge transport is the question that needs to be answered to optimize the potential of the weakly-ordered conjugated polymer.

This thesis aims to investigate the microstructures and charge transport of weakly-ordered conjugated polymer thin films. This thesis focuses on aggregates (short-range ordered structures) of hole-transport and electron transport polymer in the neat films and blends films.

1.3. General approach to characterize microstructures and charge transport in thin films of conjugated polymers

Grazing Incidence Wide-Angle Scattering (GIWAX)

As has been mention before in the previous section, the charge transport of semicrystalline conjugated polymers is highly correlated with the ordered domains. These domains are consist of long-range ordering in each direction

Optical microscopy, atomic force microscopy (AFM), and scanning electron microscopy (SEM) provide an overview of the surface structure on a larger scale. However, several films of conjugated polymers show a structural difference between the surface and the internal film.[21–24] In the OPVs application, the Donor/Acceptor interface and the ordered structure in the internal films are the significant parameters that dictate the overall device performance. Therefore, the characterization of the internal structure is required.

Grazing incidence small-angle scattering (GISAXS) and (GIWAXS) are the X-ray scattering techniques to characterize the internal film structure in the nanometer scale and the molecular scale, respectively.[25–28] The 2D detector provides scattering intensity in the horizontal and

vertical direction, which enables us to measure the degree of crystallinity, the size, and the orientation of the ordered structure.

The scattering intensity pattern in both directions carries structural information. The center position q of the scattering peaks bring the information of the spacing d of molecular packing and stacking according to **Equation 1-1**.

$$d = \frac{2\pi}{q}$$

Equation 1-1

The full width at half maximum (FWHM) of scattering peaks carries the information of coherence length L_c based on the Scherrer equation (**Equation 1-2**, where K is the shape factor).[27,28]

$$L_c = \frac{2\pi K}{\text{FWHM}}$$

Equation 1-2

UV-visible spectroscopy

UV-visible absorption spectroscopy is able to reveal the formation of aggregates, short-range ordering, which are characteristic of structure for charge transport in the weakly-ordered conjugated polymers. The shape of the absorption spectrum varies depending on the conformation of polymer chains, disordered and ordered structure.[29] Therefore, the change in the degree of disorder and order of polymer chains can be estimated from the shape and intensity of the spectra.

The absorption spectra of semicrystalline polymers consisted of two contributions, amorphous at the shorter wavelength formed by intra-chain interaction and crystalline at the longer wavelength formed by inter-chain interaction, such as H-aggregate states.[30] In the longer wavelength, two prominent peaks exist. The ratio of these peaks has been popularly used to measure the exciton bandwidth of highly-ordered semicrystalline Regioreguler Poly(3-hexylthiophene-2,5-diyl) (RR-P3HT).[31] By the exciton bandwidth, the conjugation length of

the polymer, which correlates with the charge transport, can be estimated based on the empirical[32] and modeling[33] correlation approach. In short, the knowledge on how the absorptions describe aggregates of highly-ordered RR-P3HT has been known in this research field. However, the knowledge of highly-ordered conjugated polymers is still limited for the weakly-ordered polymers

Macroscopic current-voltage characterization

The mobility of the charge carrier is the key parameter to describe the charge transport property of polymer films. An ideal current-voltage characteristic of conjugated polymers shows two regions: the ohmic region and space charge limited region (SCLC) (**Figure 1-3**). Both regions can be differentiated by a slope. The ohmic region shows slope 1, and the SCLC region shows slope 2. The transition from ohmic to SCLC region takes place at a specific voltage termed as threshold voltage V_T. The simplest SCLC model is the classical Mott-Gunrey law (**Equation 1-3**):

$$J = \frac{9}{8}\varepsilon\mu\frac{V_0^2}{L^3}$$

Equation 1-3

J is current density, ε is permittivity, V_0 is applied voltage, L is film thickness, and μ is mobility.
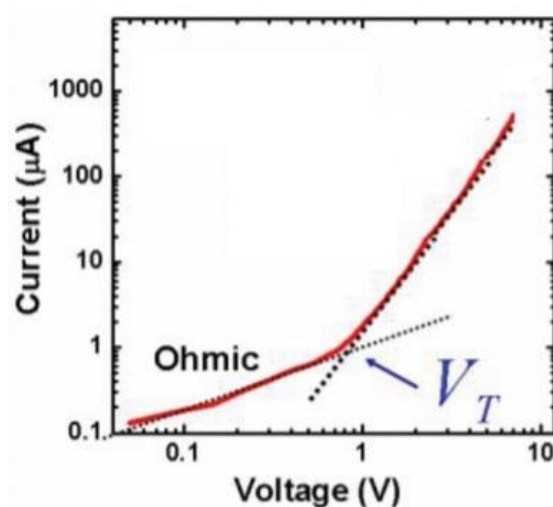
Figure 1-3. Ideal current-voltage characteristics of conducting polymer diode[34]

For polymers with shallow traps and energetically disordered, the mobility varies with the electric field, and the SCLC region has a slope higher than 2. The SCLC model fit for these polymers is:

$$J = \frac{9}{8}\varepsilon\mu_0 \frac{V_0^2}{L^3} e^{(0.89\gamma\sqrt{E})}$$ **Equation 1-4**

Where μ_0 is mobility at zero electric fields, E is the electric field, and γ is a fitting parameter which is related to the characteristic of the polymers (the higher the γ, the higher the energetic disorder of the polymer)[35].

Conductive-Atomic Force Microscopy (C-AFM)

C-AFM is an analytical tool for the characterization of local charge transport properties in a nanometer-scale resolution. In this approach, the electrode coated probe acts as an electrode to inject or collect charges from the surface of the film (
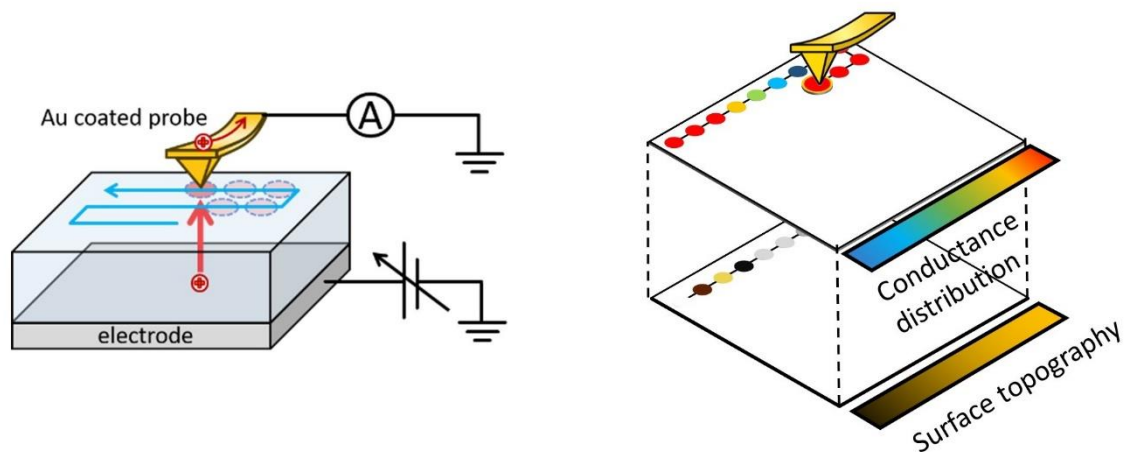
Figure 1-4). The probe is moved along the surface of the materials while taking current and topographical data from each point. The collected information on surface topography and charge current is collected and processed by the software to produce topographic and current images simultaneously. The resulting image can have a resolution better than 20 nm. This nanoscale resolution is an advantage to draw local-current characteristics of conjugated

8

polymer films. This advantage enables us to directly correlating morphological and macroscopic characterization.[36,37]
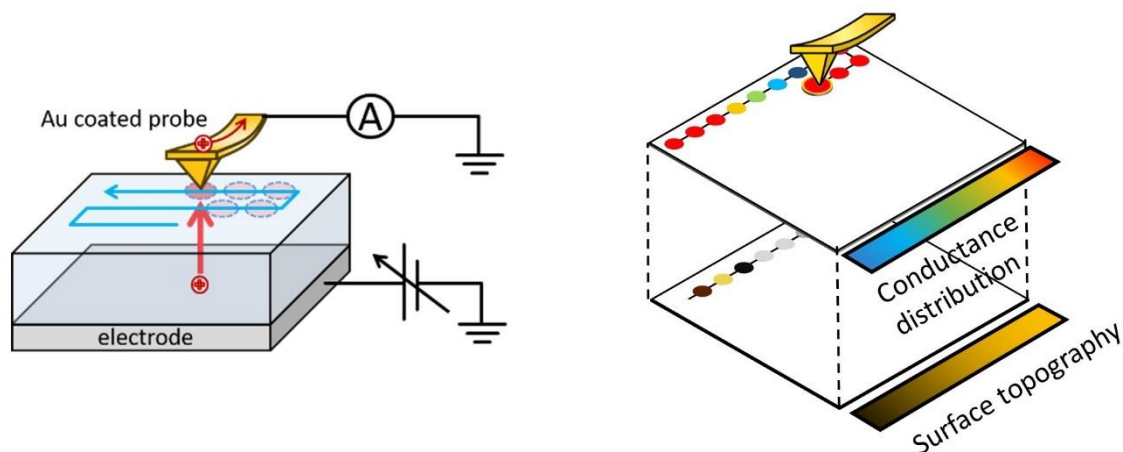
Figure 1-4. The schematic principle of C-AFM measurement

1.4. Outline of the thesis

This thesis aims to investigate the microstructures and charge transport of weakly-ordered conjugated polymer thin films. The conjugated polymers used in this thesis were electron donor (hole transporting) polymer in chapter 2 and 3, and the electron acceptor (electron-transporting) polymer in chapter 3 (**Figure 1-5**). The chapters relate ~~one to another~~ in the manner shown in **Figure 1-5**. The thesis consists of five chapters. The first chapter describes the background and motivation of the thesis: Microstructures of conjugated polymers, charge transport of conjugated polymers, and general approaches to characterize microstructures and charge transport in thin films of the conjugated polymers.

In chapter 2, The effect of aggregates on the charge transport of the weakly-ordered conjugated donor polymer has been investigated. The change in the microstructures at the segmental level of polymer chains was characterized by the analysis of UV-visible absorption spectra. The UV-visible absorption of the polymer film consists of two contributions,

amorphous and aggregates. The intensity ratio between these two contributions represents the relative fraction of aggregates to the amorphous structure inside the film. The increase of the fraction of aggregate leads to an increase in hole mobility. This positive correlation indicates that aggregates are an important structure for charge transport, where a higher fraction of aggregates in the films leads to better charge transport.

Chapter 3 discusses the change of microstructures and the hole transport in a blend film of conjugated polymers. The results from UV-visible absorption spectra analysis and XRD measurement indicated that the fraction and the size of aggregates are increased by blending. The C-AFM current images revealed that the interconnected enhanced aggregation of donor polymer provided higher current than in the neat film.

Chapter 4 focuses on the microstructures and electron transport of the conjugated acceptor polymer thin film. Firstly, a shallow work-function electrode was ~~being~~ developed by using a polymer-based surface modifier. The local electrical conductivity was visualized for thin films of small molecule, Perylene-diimide (PDI) based dimer, and polymer acceptors by C-AFM, using a modified substrate as an electron-injecting electrode. Densely and homogeneously distributed small molecule nano-aggregates leads to the excellent and uniform electron transport throughout the film. The introduction of the twisted dimeric structure of the PDI-dimer resulted in the uniform morphology for electron transport, but the suppressed intermolecular stacking resulted in the limited electron transport. On the other hand, polymer acceptor P(PDI-2T) formed spatially inhomogeneous electron-conducting morphology composed of relatively high conductive domains due to aggregation among conjugated polymer chains. The current distribution images depicted the role of the local ordering and aggregation behavior of the acceptor molecules in the electrically conductive properties of the films on a macroscale.

Chapter 5 is the general conclusion for this thesis. This thesis clears the correlation between microstructure and the charge transport of conjugated polymer thin films. An approach to estimate the fraction of aggregates has been developed from the simple UV-visible absorption spectroscopy. A mechanism of enhanced aggregation in polymer/polymer blend films was proposed. The development of an electron injecting electrode combined with the C-AFM approach enables to visualize electron transport characteristic of conjugated acceptor polymers. These results will contribute to the further development of organic electronic devices made by both conjugated donor and acceptor polymers.
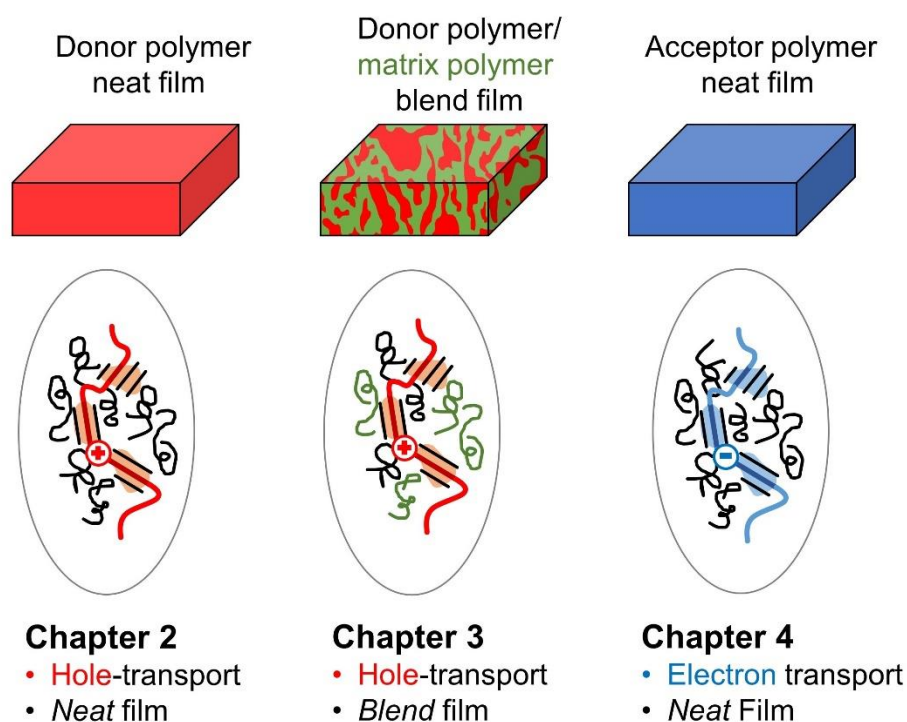
Figure 1-5. Schematic illustration of the objects of each chapter in this thesis

1.5. Reference

(1)   Law, K. Y. Organic Photoconductive Materials: Recent Trends and Developments. *Chem. Rev.* **1993**, *93* (1), 449–486. https://doi.org/10.1021/cr00017a020.

(2)   Kuehne, A. J. C.; Gather, M. C. Organic Lasers: Recent Developments on Materials, Device Geometries, and Fabrication Techniques. *Chem. Rev.* **2016**, *116* (21), 12823–12864. https://doi.org/10.1021/acs.chemrev.6b00172.

(3)   Beaujuge, P. M.; Reynolds, J. R. Color Control in π-Conjugated Organic Polymers for Use in Electrochromic Devices. *Chem. Rev.* **2010**, *110* (1), 268–320. https://doi.org/10.1021/cr900129a.

(4)   Facchetti, A. π-Conjugated Polymers for Organic Electronics and Photovoltaic Cell Applications. *Chem. Mater.* **2011**, *23* (3), 733–758. https://doi.org/10.1021/cm102419z.

(5)   Clark, J.; Lanzani, G. Organic Photonics for Communications. *Nat. Photonics* **2010**, *4* (7), 438–446. https://doi.org/10.1038/nphoton.2010.160.

(6)   Dodabalapur, A. Organic and Polymer Transistors for Electronics. *Mater. Today* **2006**, *9* (4), 24–30. https://doi.org/10.1016/S1369-7021(06)71444-4.

(7)   Li, G.; Zhu, R.; Yang, Y. Polymer Solar Cells. *Nat. Photonics* **2012**, *6* (3), 153–161. https://doi.org/10.1038/nphoton.2012.11.

(8)   Shirakawa, H.; Louis, E. J.; MacDiarmid, A. G.; Chiang, C. K.; Heeger, A. J. Synthesis of Electrically Conducting Organic Polymers: Halogen Derivatives of Polyacetylene, (CH)X. *J. Chem. Soc. Chem. Commun.* **1977**, No. 16, 578–580. https://doi.org/10.1039/C39770000578.

(9)   Koezuka, H. Field-Effect Transistor with Polythiophene Thin Film. *Synth. Met.* **1987**, *18*, 699–704.

(10)   Burroughes, J. H.; Bradley, D. D. C.; Brown, A. R.; Marks, R. N.; Mackay, K.; Friend, R. H.; Burns, P. L.; Holmes, A. B. Light-Emitting Diodes Based on Conjugated Polymers.

Nature **1990**, *347* (6293), 539–541. https://doi.org/10.1038/347539a0.

(11) Noriega, R.; Rivnay, J.; Vandewal, K.; Koch, F. P. V.; Stingelin, N.; Smith, P.; Toney, M. F.; Salleo, A. A General Relationship between Disorder, Aggregation and Charge Transport in Conjugated Polymers. *Nat. Mater.* **2013**, *12* (11), 1038–1044. https://doi.org/10.1038/nmat3722.

(12) Noriega, R. Efficient Charge Transport in Disordered Conjugated Polymer Microstructures. **2018**, *1800096*, 1–9. https://doi.org/10.1002/marc.201800096.

(13) Duong, D. T.; Toney, M. F.; Salleo, A. Role of Confinement and Aggregation in Charge Transport in Semicrystalline Polythiophene Thin Films. *Phys. Rev. B - Condens. Matter Mater. Phys.* **2012**, *86* (20), 1–5. https://doi.org/10.1103/PhysRevB.86.205205.

(14) Spano, F. C. Modeling Disorder in Polymer Aggregates: The Optical Spectroscopy of Regioregular Poly(3-Hexylthiophene) Thin Films. *J. Chem. Phys.* **2005**, *122* (23). https://doi.org/10.1063/1.1914768.

(15) Clark, J.; Silva, C.; Friend, R. H.; Spano, F. C. Role of Intermolecular Coupling in the Photophysics of Disordered Organic Semiconductors: Aggregate Emission in Regioregular Polythiophene. *Phys. Rev. Lett.* **2007**, *98* (20), 1–4. https://doi.org/10.1103/PhysRevLett.98.206406.

(16) Clark, J.; Chang, J.; Spano, F. C.; Friend, R. H.; Silva, C. Supplementary Information for " Determining Exciton Bandwidth and Film Microstructure in Polythiophene Films Using Linear Absorption Spectroscopy ": Determination of the Relative Absorption Cross-Section in Aggregated and Amorphous Phases of P3HT . *America (NY).* No. 2, 3–4.

(17) Malliaras, G.; Friend, R. An Organic Electronics Primer. *Phys. Today* **2005**, *58* (5), 53–58. https://doi.org/10.1063/1.1995748.

(18) Northrup, J. E. Mobility Enhancement in Polymer Organic Semiconductors Arising from

Increased Interconnectivity at the Level of Polymer Segments. *Appl. Phys. Lett.* **2015**, *106* (2). https://doi.org/10.1063/1.4906061.

(19) Kleinschmidt, A. T.; Root, S. E.; Lipomi, D. J. Poly(3-Hexylthiophene) (P3HT): Fruit Fly or Outlier in Organic Solar Cell Research? *J. Mater. Chem. A* **2017**, *5* (23), 11396–11400. https://doi.org/10.1039/c6ta08317j.

(20) Wang, S.; Fabiano, S.; Himmelberger, S.; Puzinas, S.; Crispin, X.; Salleo, A.; Berggren, M. Experimental Evidence That Short-Range Intermolecular Aggregation Is Sufficient for Efficient Charge Transport in Conjugated Polymers. *Proc. Natl. Acad. Sci. U. S. A.* **2015**, *112* (34), 10599–10604. https://doi.org/10.1073/pnas.1501381112.

(21) Ruderer, M. A.; Prams, S. M.; Rawolle, M.; Zhong, Q.; Perlich, J.; Roth, S. V.; Müller-Buschbaum, P. Influence of Annealing and Blending of Photoactive Polymers on Their Crystalline Structure. *J. Phys. Chem. B* **2010**, *114* (47), 15451–15458. https://doi.org/10.1021/jp106972s.

(22) Ruderer, M. A.; Guo, S.; Meier, R.; Chiang, H. Y.; Körstgens, V.; Wiedersich, J.; Perlich, J.; Roth, S. V.; Müller-Buschbaum, P. Solvent-Induced Morphology in Polymer-Based Systems for Organic Photovoltaics. *Adv. Funct. Mater.* **2011**, *21* (17), 3382–3391. https://doi.org/10.1002/adfm.201100945.

(23) Hoppe, H.; Sariciftci, N. S. Morphology of Polymer/Fullerene Bulk Heterojunction Solar Cells. *J. Mater. Chem.* **2006**, *16* (1), 45–61. https://doi.org/10.1039/b510618b.

(24) Ruderer, M. A.; Wang, C.; Schaible, E.; Hexemer, A.; Xu, T.; Müller-Buschbaum, P. Morphology and Optical Properties of P3HT:MEH-CN-PPV Blend Films. *Macromolecules* **2013**, *46* (11), 4491–4501. https://doi.org/10.1021/ma4006999.

(25) Müller-Buschbaum, P. The Active Layer Morphology of Organic Solar Cells Probed with Grazing Incidence Scattering Techniques. *Adv. Mater.* **2014**, *26* (46), 7692–7709. https://doi.org/10.1002/adma.201304187.

(26) Rogers, J. T.; Schmidt, K.; Toney, M. F.; Kramer, E. J.; Bazan, G. C. Structural Order in Bulk Heterojunction Films Prepared with Solvent Additives. *Adv. Mater.* **2011**, *23* (20), 2284–2288. https://doi.org/10.1002/adma.201003690.

(27) Smilgies, D. M. Scherrer Grain-Size Analysis Adapted to Grazing-Incidence Scattering with Area Detectors. *J. Appl. Crystallogr.* **2009**, *42* (6), 1030–1034. https://doi.org/10.1107/S0021889809040126.

(28) Rivnay, J.; Mannsfeld, S. C. B.; Miller, C. E.; Salleo, A.; Toney, M. F. Quantitative Determination of Organic Semiconductor Microstructure from the Molecular to Device Scale. *Chem. Rev.* **2012**, *112* (10), 5488–5519. https://doi.org/10.1021/cr3001109.

(29) Scharsich, C.; Fischer, F. S. U.; Wilma, K.; Hildner, R.; Ludwigs, S.; Köhler, A. Revealing Structure Formation in PCPDTBT by Optical Spectroscopy. *J. Polym. Sci. Part B Polym. Phys.* **2015**, *53* (20), 1416–1430. https://doi.org/10.1002/polb.23780.

(30) Panzer, F.; Bässler, H.; Köhler, A. Temperature Induced Order-Disorder Transition in Solutions of Conjugated Polymers Probed by Optical Spectroscopy. *J. Phys. Chem. Lett.* **2017**, *8* (1), 114–125. https://doi.org/10.1021/acs.jpclett.6b01641.

(31) Clark, J.; Chang, J. F.; Spano, F. C.; Friend, R. H.; Silva, C. Determining Exciton Bandwidth and Film Microstructure in Polythiophene Films Using Linear Absorption Spectroscopy. *Appl. Phys. Lett.* **2009**, *94* (16), 2007–2010. https://doi.org/10.1063/1.3110904.

(32) Pingel, P.; Zen, A.; Abellón, R. D.; Grozema, F. C.; Siebbeles, L. D. A.; Neher, D. Temperature-Resolved Local and Macroscopic Charge Carrier Transport in Thin P3HT Layers. *Adv. Funct. Mater.* **2010**, *20* (14), 2286–2295. https://doi.org/10.1002/adfm.200902273.

(33) Gierschner, J.; Huang, Y. S.; Van Averbeke, B.; Cornil, J.; Friend, R. H.; Beljonne, D. Excitonic versus Electronic Couplings in Molecular Assemblies: The Importance of

Non-Nearest Neighbor Interactions. *J. Chem. Phys.* **2009**, *130* (4). https://doi.org/10.1063/1.3065267.

(34) Syed, A.; Moiz, A.; Karimov, K. S. Space Charge – Limited Charge – Limited Current Current Model Space Model for for Polymers Polymers And. **2016**.

(35) Martens, H.; Blom, P. Comparative Study of Hole Transport in Poly(p-Phenylene Vinylene) Derivatives. *Phys. Rev. B - Condens. Matter Mater. Phys.* **2000**, *61* (11), 7489–7493. https://doi.org/10.1103/PhysRevB.61.7489.

(36) Osaka, M.; Benten, H.; Ohkita, H.; Ito, S. Intermixed Donor/Acceptor Region in Conjugated Polymer Blends Visualized by Conductive Atomic Force Microscopy. *Macromolecules* **2017**, *50* (4), 1618–1625. https://doi.org/10.1021/acs.macromol.6b02604.

(37) Osaka, M.; Mori, D.; Benten, H.; Ogawa, H.; Ohkita, H.; Ito, S. Charge Transport in Intermixed Regions of All-Polymer Solar Cells Studied by Conductive Atomic Force Microscopy. *ACS Appl. Mater. Interfaces* **2017**, *9* (18), 15615–15622. https://doi.org/10.1021/acsami.7b00979.

Chapter 2.

Microstructures and Hole Transport of Weakly-Ordered Conjugated Polymer Film

2.1. Introduction

Conjugated polymers have attracted attention as critical materials for the thin-films optoelectronic devices such as OPVs,[1] OLEDs,[2] and OTFTs.[3] Their color-tunability and solution-based processing are suitable for low-cost, large-scale production. The ordered and disordered structure of order-disorder polymer chains primarily impacts its charge-transporting properties.[4,5] Highly-ordered conjugated polymers are widely used in the organic electronic application due to their high charge mobility. However, a recent class of weakly-ordered conjugated polymers is gaining interest because they show comparable mobilities to the highly-ordered polymers.[4,6]

This seemingly contradictory feature of efficient charge transport property without forming long-range ordered structures needs to be cleared. One of the critical parameters in this polymer which might contribute to the high charge transport is the density of the aggregates. Not all the aggregates can be detected by X-ray diffraction because of the scale limitation. However, all of the aggregates can be detected by UV-vis absorption measurement from its vibrational spectra. However, an approach to observing aggregates by absorption measurement is still limited.

PSBTBT (**Figure 2-1**) is one of the weakly-ordered conjugated polymers. PSBTBT has a relatively shorter π-π stacking distance, which is suitable for charge transport. It also has a broad absorption band in the visible wavelengths, suitable for OPVs application[7–9].

The purpose of this chapter is to investigate the role of aggregate for the charge transport of conjugated donor polymer neat film. The fraction of aggregate inside the film was estimated by

analyzing UV-vis absorption measurement. The hole mobility of the film was extracted from the *J-V* characteristics. Finally, the correlation between the fraction of aggregate and the hole mobility was elucidated.
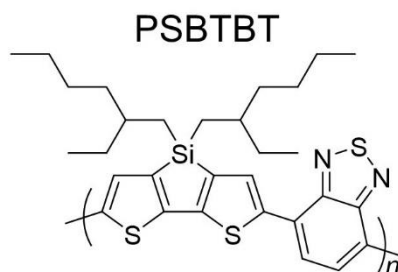
Figure 2-1. Chemical structure of PSBTBT

2.2. Experimental

2.2.1. Materials and sample preparation

Materials: Poly[4,4-bis(2-ethylhexyl)-dithieno[3,2-b:2',3'-d]silole]-2,6-diyl-alt-(2,1,3-benzothiadiazole)-4,7-diyl] (PSBTBT (Si-PCPDTBT), M_w = 50,000 g/mol, polydispersity index (PDI) = 1.9) was purchased from Ossila Ltd.

Substrates: A quartz, a Si wafer (Yamanaka Hutech, Japan), and an indium-tin-oxide (flat ITO, GEOMATEC, Japan) substrates were sequentially washed by ultrasonication with toluene, acetone, and ethanol for 10 minutes for each solvent. The substrates were then treated by UV-O_3 cleaner after being dried by N_2 flow.

Solution: The PSBTBT solution was prepared by dissolving PSBTBT in o-Dichlorobenzene (DCB) under stirring at 95 °C for overnight. The solution concentration was adjusted to 0.005 mg/ml for absorption in the solution state and 10, 12, and 20 mg/ml for spin-coating.

Polymer film: The PSBTBT solutions were spin-coated at 800 to 8000 rpm for 3 minutes on quartz substrates inside the N_2-filled glovebox. The film samples were dried in a vacuum desiccator for 2 hours.

Hole-only device:

First, PEDOT:PSS (H. C. Starck, PH500) layer was prepared on the ITO substrate. PEDOT:PSS solution was sonicated for 10 minutes and filtered by 0.45 µm diameter-pores filter. The solution was spin-coated at 400 rpm for 10 seconds, followed by 3000 rpm for 100 seconds. The PEDOT:PSS film was annealed at 140 ℃ for 10 minutes.

Second, The PSBTBT solutions were spin-coated at 800 to 8000 rpm for 3 minutes on PEDOT:PSS substrates. Inside the N_2-filled glovebox, the samples were dried in the vacuum chamber for overnight.

Finally, MoOx (10 nm) and Au (100 nm) were deposited sequentially under vacuum (3×10^{-5}) Pa.

2.2.2. Characterizations

UV-vis Absorption Measurement: UV-vis absorption was measured for PSBTBT films and solution by UV-vis Spectrophotometer (V-770DS, JASCO, Japan). The absorption spectra of films were measured at room temperature. The absorption spectra of the solution were measured at a temperature from -5 to 145 ℃. The solution temperature was controlled by computer-controlled Peltier heating and cooling cuvette holder (ETCS-761, JASO, Japan).

Film Thickness Measurement: Film thickness was measured using contact mode Atomic Force Microscopy (SPM-9700, Shimadzu Corp., Japan). The surface of each film was scratched by a

sharp needle to expose the quartz substrate. The height difference between film and substrate was defined as the film thickness.

Macroscopic J-V Measurement: Current density-voltage (*J-V*) characteristics were measured for the hole-only device where film was sandwiched between ITO/PEDOT:PSS and MoOx/Au electrodes. Samples were kept in the N_2-filled chamber at room temperature during the measurement. The bias voltage was applied to PEDOT:PSS electrode by a direct-current source/monitor (R6243, Advantest).

C-AFM Measurement: C-AFM measurement was performed by using Atomic Force Microscopy (SPM-9900, Shimadzu Corp., Japan) in a contact mode with an Au-coated silicon probe (PPP-CONTAu, NANOSENSORS[TM], Switzerland; tip radius < 50 nm; spring constant = 0.2 – 0.25 N m^{-1}). Voltage bias was applied to the PEDOT:PSS electrode, and the probe was grounded. The sample was being kept in the N_2 flow environment during the ~~current~~ measurement.

2.3. Result and discussion

2.3.1. Optical characterization of PSBTBT in DCB solution
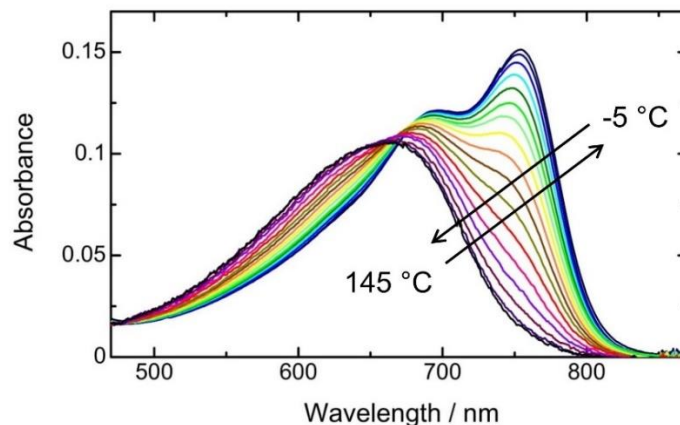
Figure 2-2. UV-visible spectra of PSBTBT in DCB (C = 0.005 mg/ml) measured at -5 to 145 ℃ (or from -5 to 145 ℃); the arrow shows increasing (or decreasing) measurement temperature.

Figure 2-2 shows the UV-visible absorption spectra of PSBTBT in DCB at various temperatures. The solution was measured stepwise from -5 ℃ (bluish color) to 145 ℃ (reddish color). The peak position and the shape of the absorption spectra were gradually changing along with the temperature measurement. The spectra from the two extreme temperatures showed different spectral features (position and shape). The spectrum from -5 ℃-temperature measurement lies at a longer wavelength with two prominent peaks, while the spectrum from 145 ℃-temperature measurement lies at a shorter wavelength with only one peak.

The change in the spectra represents the structural change of polymer chains at the segmental level.[10] At low temperature, the polymer chains are expected to be the aggregated, and planarized structures are disrupted to form disordered chains. Therefore, spectral change from narrower to the broader shape reflects the change in chain conformation from aggregated to more disordered condition.[11] The absorption at 145 ℃ was assigned to the contribution from disordered PSBTBT chains.

21

The term spectral decomposition is used in this thesis for a process to separate film or solution absorption into two contributions, amorphous (disordered) and aggregates (ordered). The spectral decomposition yielded the absorption of ~~pure~~ aggregates for each measurement temperature in **Figure A2-1** in the appendix. The same approach of using absorption measured at high temperature as absorption of complete disordered, then use it to get a relative absorption of aggregated spectra, has been reported by Clark et al.[12] This approach is based on the isosbestic point in **Figure 2-2** as the real evidence of structural transformation between disordered and aggregated phase.[13]

2.3.2. Optical characterization of PSBTBT thin films
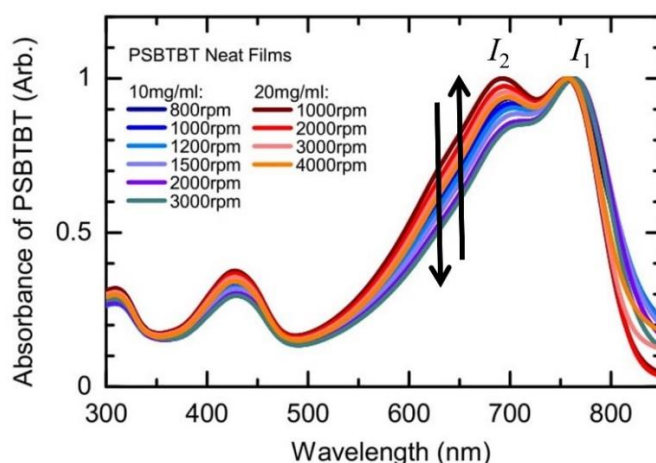
Figure 2-3. UV-visible spectra of PSBTBT Films from various preparation conditions; the spectra were normalized by the first peak from the longer wavelength.

Figure 2-3 is the UV-visible spectra of PSBTBT films from different spin-coating conditions. In this thesis, the peak at the shorter and longer wavelength was represented by I_2 and I_1, respectively. These two peaks are the peaks of total film absorption, and it was not the peak of the pure aggregated structure. The intensity ratio of I_1 to I_2 was used to describe the change in the structure of polymer chains. The black arrow in the figure shows a clear decrease

in the relative intensity of I_2. This change is related to the film preparation condition. The Films prepared from low concentration and higher spin-coating speed gives lower I_2 intensity.

The change in the shape of PSBTBT film absorption is related to the change in the microstructures. Polymer films contain both amorphous (disordered) and aggregates (ordered chain). Therefore, the film absorption in **Figure 2-3** can be separated into contributions from both amorphous chains at the shorter wavelength and aggregated chains at the longer wavelength. Therefore the decrease in the relative intensity of I_2 indicates that the fraction of amorphous polymer chains decreases.

2.3.3. Calculation approach to estimate the fraction of aggregates in the films
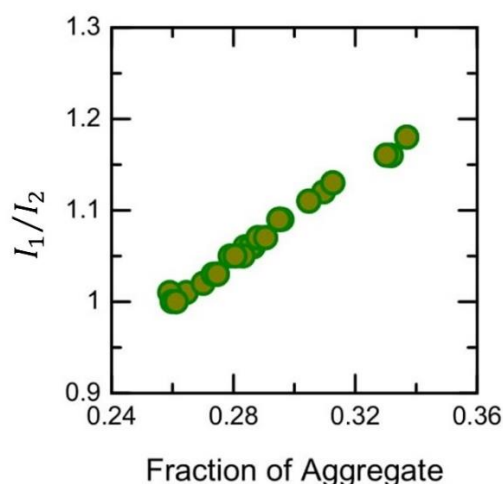
Figure 2-4. Correlation between I_1/I_2 and fraction of aggregates.

Figure 2-4 shows the correlation between I_1/I_2 and the fraction of aggregates. The value of I_1/I_2 was calculated from the absorption intensity ratio of each PSBTBT film. The fraction of aggregates was calculated by spectral decomposition for the corresponding PSBTBT film.

Figure 2-4 shows when I_1/I_2 increases, the aggregates increase. This trend is coming from the fact that I_2 peak intensity includes the amorphous contribution So that when the amorphous

contribution becomes lower and the aggregate contribution becomes higher, and the value of I_1/I_2 is increasing.

2.3.4. Hole mobility of PSBTBT thin films
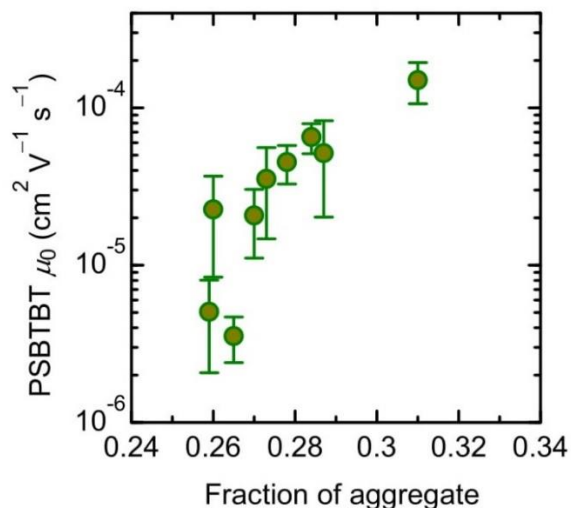
Figure 2-5. Correlation between the fraction of aggregates and macroscopic hole mobility. Macroscopic hole mobility was extracted from the field-effect SCLC model based on **Equation 1-4**.

Figure 2-5 shows the correlation between the fraction of aggregate and macroscopic hole mobility. The hole mobility was extracted from the *J-V* characteristics of each sample. One example is shown in **Figure A2-4**. The figures show a positive correlation where a higher fraction of aggregate leads to higher hole mobility. In conclusion, the ordering at the segmental level (aggregates) supports the charge transport.

2.4. Conclusions

In this chapter, the role of aggregates on the charge transport property of the weakly-ordered conjugated donor polymer has been cleared. The fraction of aggregate has been estimated by analyzing UV-vis spectra of PSBTBT neat films prepared by various spin-coating conditions.

the fraction of aggregate and I_1/I_2 shows a positive correlation: the increase in the value of I_1/I_2 from 1.0 to 1.2 corresponding to an increase in the fraction of aggregate from 0.26 to 0.34. Hole mobility extracted from the *J-V* characteristic also shows a positive correlation: The increase in the fraction of aggregate corresponded to an increase of hole mobility from 1.89×10^{-5} to 1.53×10^{-4} cm^2/Vs. This positive correlation indicates that aggregates are important for charge transport: where a higher fraction of aggregates in the films would lead to better charge transport (**Figure 2-6**).
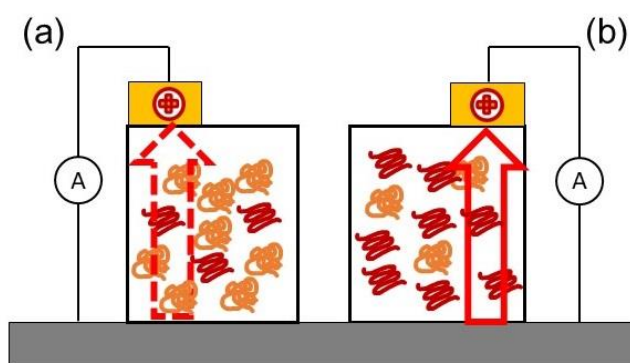
Figure 2-6. Illustration of charge transport through the weakly-ordered conjugated polymer films with (a) low fraction of aggregate and (b) high fraction of aggregate.

2.5. Reference

(1)   Cheng, Y. J.; Yang, S. H.; Hsu, C. S. Synthesis of Conjugated Polymers for Organic Solar Cell Applications. *Chem. Rev.* **2009**, *109* (11), 5868–5923. https://doi.org/10.1021/cr900182s.

(2)   Grimsdale, A. C.; Chan, K. L.; Martin, R. E.; Jokisz, P. G.; Holmes, A. B. Synthesis of Light-Emitting Conjugated Polymers for Applications in Electroluminescent Devices. *Chem. Rev.* **2009**, *109* (3), 897–1091. https://doi.org/10.1021/cr000013v.

(3)   Facchetti, A. π-Conjugated Polymers for Organic Electronics and Photovoltaic Cell Applications. *Chem. Mater.* **2011**, *23* (3), 733–758. https://doi.org/10.1021/cm102419z.

(4)   Noriega, R.; Rivnay, J.; Vandewal, K.; Koch, F. P. V.; Stingelin, N.; Smith, P.; Toney, M. F.; Salleo, A. A General Relationship between Disorder, Aggregation and Charge Transport in Conjugated Polymers. *Nat. Mater.* **2013**, *12* (11), 1038–1044. https://doi.org/10.1038/nmat3722.

(5)   Noriega, R. Efficient Charge Transport in Disordered Conjugated Polymer Microstructures. *Macromol. Rapid Commun.* **2018**, *39* (14), 1–9. https://doi.org/10.1002/marc.201800096.

(6)   Gu, K.; Loo, Y. L. The Polymer Physics of Multiscale Charge Transport in Conjugated Systems. *J. Polym. Sci. Part B Polym. Phys.* **2019**, *57* (23), 1559–1571. https://doi.org/10.1002/polb.24873.

(7)   Bin Mohd Yusoff, A. R.; Lee, S. J.; Kim, H. P.; Shneider, F. K.; Da Silva, W. J.; Jang, J. 8.91% Power Conversion Efficiency for Polymer Tandem Solar Cells. *Adv. Funct. Mater.* **2014**, *24* (15), 2240–2247. https://doi.org/10.1002/adfm.201303471.

(8)   Wang, Y.; Ohkita, H.; Benten, H.; Ito, S. Efficient Exciton Harvesting through Long-Range Energy Transfer. *ChemPhysChem* **2015**, *16* (6), 1263–1267. https://doi.org/10.1002/cphc.201402740.

(9)   Etzold, F.; Howard, I. A.; Forler, N.; Melnyk, A.; Andrienko, D.; Hansen, M. R.; Laquai, F. Sub-Ns Triplet State Formation by Non-Geminate Recombination in PSBTBT:PC70BM and PCPDTBT:PC60BM Organic Solar Cells. *Energy Environ. Sci.* **2015**, *8* (5), 1511–1522. https://doi.org/10.1039/c4ee03630a.

(10)   Reichenberger, M.; Kroh, D.; Matrone, G. M. M.; Schötz, K.; Pröller, S.; Filonik, O.; Thordardottir, M. E.; Herzig, E. M.; Bässler, H.; Stingelin, N.; et al. Controlling Aggregate Formation in Conjugated Polymers by Spin-Coating below the Critical Temperature of the Disorder–Order Transition. *J. Polym. Sci. Part B Polym. Phys.* **2018**, *56* (6), 532–542. https://doi.org/10.1002/polb.24562.

(11)   Schulz, G. L.; Fischer, F. S. U.; Trefz, D.; Melnyk, A.; Hamidi-Sakr, A.; Brinkmann, M.; Andrienko, D.; Ludwigs, S. The PCPDTBT Family: Correlations between Chemical Structure, Polymorphism, and Device Performance. *Macromolecules* **2017**, *50* (4), 1402–1414. https://doi.org/10.1021/acs.macromol.6b01698.

(12)   Clark, J.; Chang, J. F.; Spano, F. C.; Friend, R. H.; Silva, C. Determining Exciton Bandwidth and Film Microstructure in Polythiophene Films Using Linear Absorption Spectroscopy. *Appl. Phys. Lett.* **2009**, *94* (16), 2007–2010. https://doi.org/10.1063/1.3110904.

(13)   Scharsich, C.; Fischer, F. S. U.; Wilma, K.; Hildner, R.; Ludwigs, S.; Köhler, A. Revealing Structure Formation in PCPDTBT by Optical Spectroscopy. *J. Polym. Sci. Part B Polym. Phys.* **2015**, *53* (20), 1416–1430. https://doi.org/10.1002/polb.23780.

Chapter 3.

Microstructures and Hole Transport of Polymer/Polymer Blend Films

3.1. Introduction

The performance of flexible and printable electronic devices, such as organic field-effect organic solar cells (OSCs)[4,5], and transistors (OFETs)[1–3] built from solution-processed thin films of conjugated polymers, have enhanced significantly in recent years. For more than a decade, the research has primarily focused on a strategy to improve solid-state charge transport properties by increasing the crystallinity and long-range structural order of thin films. The design and synthesis of semicrystalline conjugated polymers that exhibit a substantial self-assembly tendency to increase the charge carrier mobility because of formed-crystallites by interchain interaction.[6–10]

Aside from a great deal of work on the neat film of highly-ordered conjugated polymers, blending highly-ordered conjugated polymers with other polymers is an effective strategy to control the microstructure in the films.[11,12] For the applications of OFETs, it is vastly reported that blending a highly-ordered conjugated polymer with an insulating commodity polymer is essential for the improvement of charge carrier mobility.[12–15] In the blend films, vertical phase segregations between the conjugated and insulating polymers are conducive. The conductivity properties come from high crystalline orders with continuous percolated pathways. On the other hand, the blending of the hole- and electron-transporting polymers usually increases the disordered and amorphous nature of the films in the research in polymer/polymer blend films of OSCs with highly-ordered conjugated polymers.[5,16–18] The charge transport in the blend films is disturbed both structurally and energetically. The result is the mobility becomes lower than that of the neat films of the constituent highly-ordered conjugated polymers.[5,16,17] To overcome this issue which caused by blending, several methods to improve the ordering and crystallinity

28

of the blend film have been reported. These methods include a variation of the boiling point of the spin-coating solvent, the addition of high-boiling additives, thermal annealing, and solvent-vapor annealing.[5,18,19]

The OFETs study on the weakly-ordered conjugated polymers has suggested that the short-range order in the form of aggregates, not the high degree of crystallinity of polymer chains, is sufficient to support efficient charge transport in the neat film[20] and a blend film with an insulating commodity polymer.[21] Therefore, controlling short-range ordering should have significant implications to design high-performance polymer/polymer blend OSCs. In the viewpoint of efficient charge transport, the study on the microstructures of a weakly-ordered conjugated polymer in the blend film with other conjugated polymer is essential because the film morphology designed for OSC operation is not the same as OFET achieved by the weakly-ordered conjugated polymer/insulating commodity polymer blends.[12–15,21] However, the changes in the short-range order and aggregation behavior by blending with other conjugated polymers are not fully understood.

Representative examples of the weakly-ordered conjugated polymers in the application of OSCs are found in the libraries of low-bandgap conjugated polymers comprised of donor-acceptor complex moieties as a repeat unit.[20,22–24] Among them, PCPDTBT, a copolymer of cyclopentadithiophene and benzothiadiazole, is a promising conjugated polymer which has been generally used as a hole transport and light-harvesting material for OSC applications.[25–27]

This chapter aims to investigate the change of PCPTBT aggregates after being blended with another polymer as a matrix. The matrix polymer for this research is P3M4HT. P3M4HT is a large-bandgap and amorphous conjugated polymer. The presence of a methyl group to the thiophene ring, which already includes a hexyl side chain, would cause twisting of the chain backbone due to steric hindrance and inhibit significant interaction along the backbone, disrupting π-π stacking and the associated chain ordering.[28] P3M4HT was selected as a matrix

because of its negligible absorption overlaps with PCPDTBT and its amorphous nature, which enables us to facilitate data analysis on complex microstructures of conjugated polymer blends. Further study on charge transport as the effect of blending also proceeds in this chapter by C-AFM images analysis from such blend film.
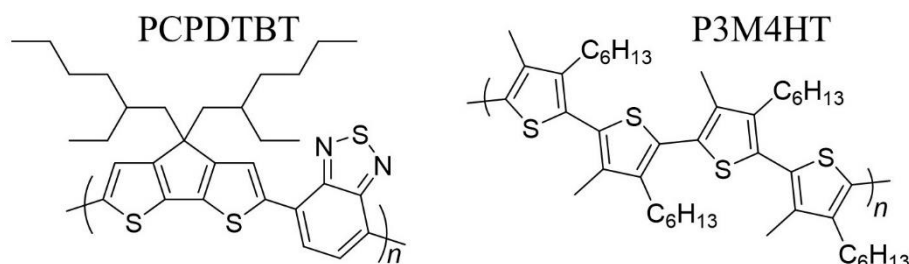
Figure 3-1. Chemical structures of PCPDTBT and P3M4HT.

3.2. Experimental

3.2.1. Materials and sample preparation

Materials:

Poly[2,6-(4,4-bis-(2-ethylhexyl)-4*H*-cyclopenta [2,1-*b*;3,4-*b*′]dithiophene)-*alt*-4,7(2,1,3-benzothiadiazole)] (PCPDTBT, M_w = 50,000 g mol^{-1}, polydispersity index (PDI) = 2.5) was purchased from 1-Material Inc. Regioregular poly(3-methyl-4-hexylthiophene-2,5-diyl) (P3M4HT, M_w = 150,000 g mol^{-1}, PDI = 2.4) was purchased from American Dye Source Inc. Poly[4,4-bis(2-ethylhexyl)-dithieno[3,2-b:2',3'-d]silole]-2,6-diyl-alt-(2,1,3-benzothiadiazole)-4,7-diyl] (PSBTBT (Si-PCPDTBT), M_w = 50,000 g/mol, polydispersity index (PDI) = 1.9) was purchased from Ossila Ltd. Polystyrene (PS, M_w = 90,900 g mol^{-1}, PDI = 1.05) and poly(methyl methacrylate) (PMMA M_w = 110,000 g mol^{-1}, PDI = 1.06) were purchased from Aldrich Chemical Co. P3M4HT, PS, and PMMA were used as amorphous matrix polymers for the PCPDTBT and PSBTBT blend films.

Sample preparation:

A quartz substrate, ITO substrate, and a-Si wafer (Yamanaka Hutech, Japan) substrate were sequentially washed via ultrasonication with toluene, acetone, and ethanol for 15 min, and then dried using a dinitrogen (N_2) flow. For hole-current measurement by C-AFM, PEDOT:PSS (H. C. Starck, PH500) layer was prepared on the ITO substrate. PEDOT:PSS solution was sonicated for 10 minutes, and filtered by 0.45 µm diameter-pores filter to avoid unwanted aggregates. The solution was spin-coated at 400 rpm for 10 seconds, followed by 3000 rpm for 100 seconds. The annealing at 140 ºC for 10 minutes was the last preparation to dry the ITO/PEDOT:PSS substrates completely.

For structure characterization, polymer neat films and blend films were prepared via spin-coating from chlorobenzene (CB) and DCB solutions onto a quartz substrate for UV-vis absorption measurements, and spin-coating from a CB solution onto a Si substrate for GIWAXS measurements. Neat films were spin-coated from a solution of 10 mg mL^{-1} of each polymer at a spinning rate of 1500 rpm for 60 s. Blend films of PCPDTBT with P3M4HT (PCPDTBT/P3M4HT), PS (PCPDTBT/PS), and PMMA (PCPDTBT/PMMA) were spin-coated from blend solutions. PCPDTBT and a matrix polymer were separately dissolved in a solvent at 10 mg mL^{-1} for both. PCPDTBT/matrix polymer solutions were obtained by mixing the respective solutions using the following volume ratios of PCPDTBT solution to matrix polymer solution: 100:0, 50:50, 20:80, 10:90, and 5:95. The polymer neat and blend film thickness was 40–50 nm.

Additionally, a CB solution of 40 mg mL^{-1} PCPDTBT was spin-coated onto a quartz substrate at a spinning rate of 4000 rpm for 120 s. The resulting PCPDTBT neat film was then melted at 310 °C for 15 min on a heating plate (its melting temperature is 293 °C)[37] and solidified from the molten state by natural cooling to room temperature in a nitrogen glove box. Before spin-coating, polymer neat and blend solutions were stirred at 80 °C for at least 12 h to

allow the complete dissolution of the samples. The solutions were spin-coated at room temperature.

For C-AFM characterization, neat and blend films of PSBTBT, and PSBTBT/P3M4HT were fabricated on the ITO/PEDOT:PSS substrates. PSBTBT and P3M4HT were dissolved in DCB at 10 mg ml^{-1}-concentration. The blend solution was prepared by blending PSBTBT and P3M4HT solution at 20/80-ratio. The neat (34 nm) and blend films (32 nm) were fabricated by spin-coating for 2 minutes at 3000 rpm and 2500 rpm, respectively.

3.2.2.   Characterizations

UV-vis characterization: UV-vis absorption spectra of polymer films on quartz substrates were measured at room temperature. The absorption of PCPDTBT CB solutions in a 1-cm quartz cuvette was also measured by a UV-vis spectrophotometer (V-770DS, JASCO, Japan) equipped with a computer-controlled Peltier heating and cooling cuvette holder (ETCS-761, JASCO, Japan). The absorption of PCPDTBT in PCPDTBT/matrix polymer blend films was obtained by subtracting the absorption of a matrix polymer from the total absorption of the blend films (see Appendix, **Figure A3-1**).

Film thickness measurements: Polymer film thickness was measured by a surface profiler (ET200, Kosaka Laboratory Ltd., Japan). Each film was scratched with a sharp needle to expose the substrate. The film thickness was defined as the height difference between the film and the substrate surface.

GIWAXS measurements: The GIWAXS measurements were carried out at room temperature for the PCPDTBT neat film (thickness of 39 nm), P3M4HT neat film (44 nm), and PCPDTBT/P3M4HT blend films (39–42 nm) using the Spring-8 BL40B2 beamline (Hyogo,

Japan). The X-ray wavelength was set to 0.1 nm, and the X-ray beam was aimed at the sample with an incident angle of 0.14° with respect to the sample surface. The X-ray exposure time was 100 s for all samples. The scattering signal was detected using a hybrid photon counting X-ray detector (Pilatus3 S 2M, Dectris Ltd., Switzerland) with a 1475×1679-pixels, which was positioned 342.8 mm away from the sample. The scattering vector magnitude q $(= (4\pi/\lambda)$ $\sin\theta$, where 2θ is the scattering angle) was calibrated using silver behenate ($q = 2\pi/5.838$ nm^{-1})).

C-AFM characterization: C-AFM measurements were performed using the microscope (SPM-9700, Shimadzu, Japan) in contact mode with an Au-coated silicon probe (PPP-CONTAu, NANO*SENSORS*^{TM}, Switzerland; tip radius < 50 nm; spring constant = 0.2–0.25 N m^{-1}). A sample bias was applied to the ITO/PEDOT:PSS electrode and the probe was. The surface topography and corresponding current images were simultaneously obtained by C-AFM measurements operating at a sample bias of: -0.4, -0.7, -1, +2, +3, +4 V. All C-AFM measurements were performed under an N$_2$ atmosphere using a controlled-environment chamber (CH-III, Shimadzu, Japan).

3.3. Results

3.3.1. Optical characterization of PCPDTBT in solution
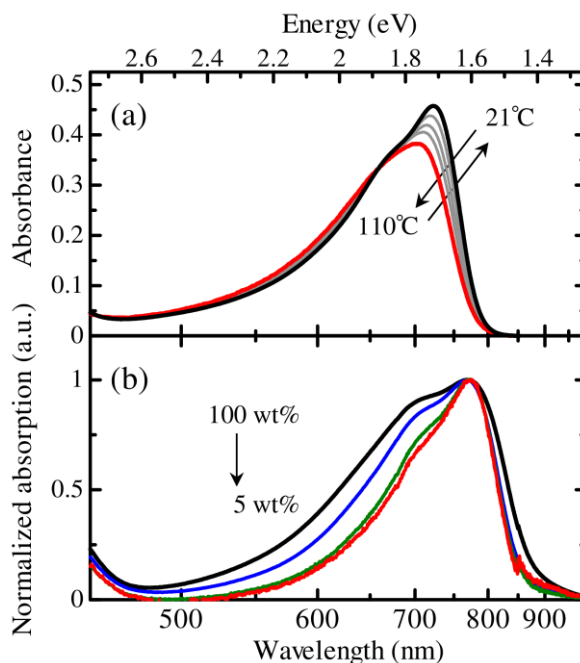
Figure 3-2. (a) UV-vis absorption spectra of PCPDTBT in solution ($c = 0.005$ mg ml^{-1} in CB) at different temperatures; the arrows indicate increasing (or decreasing) temperature from 21 to 110 °C (or 110 to 21 °C). (b) UV-vis absorption spectra of PCPDTBT in PCPDTBT/P3M4HT blend films with varying amounts of PCPDTBT, spin-coated from CB solution, and measured at room temperature. The weight percentage (wt.%) of PCPDTBT in the blend films was 100 (black line), 50 (blue line), 10 (green line), and 5 (red line). The film absorption spectra were normalized at the first absorption peak to compare the spectral shape of PCPDTBT between the blend films.

First, the UV-vis absorption spectra of PCPDTBT in a solution was measured (concentration $c = 0.005$ mg ml^{-1} in CB). The absorption spectrum at room temperature showed vibronic progression with a peak at 723 nm and a shoulder at approximately 670 nm. As the solution temperature increased, the absorption peak shifted continuously towards shorter wavelengths, and the intensity decreased (**Figure 3-2**). When the solution was heated to 110 °C, the absorption spectrum featured a broad and less-structured band peaking at 700 nm. This spectral change with increasing temperature was repeated and observed over multiple temperature

cycles. The change has been attributed to the conformational change of PCPDTBT chains from an aggregated conformation at 21 °C to a non-aggregated disordered conformation at 110 °C.[39]

As the CB solution was further diluted down to 0.001 mg ml^{-1}, the absorption features with vibronic progression had minimal variation at room temperature (see Appendix, **Figure A3-2**). At a solution concentration of 0.005 mg ml^{-1}, a sphere with a 233-nm radius contains, on average, one PCPDTBT chain coil. It indicates that there are very few interchain interactions. Therefore, we associated absorption at 21°C primarily to intra-chain (single-chain) aggregates rather than inter-chain (multichain) aggregates. Single-chain self-folded aggregation of low-bandgap donor-acceptor conjugated polymers was shown to occur in dilute solutions based on spectroscopic evidence[27,40] and molecular dynamics simulations.[35]
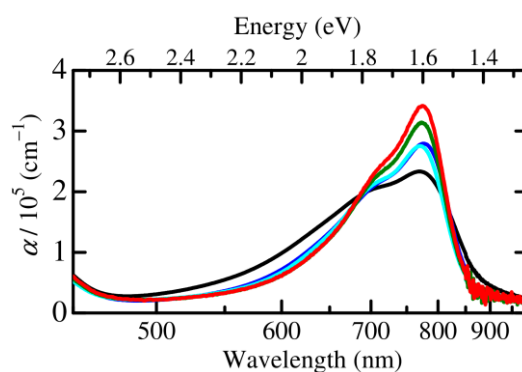
Figure 3-3. UV-vis absorption-coefficient (α) spectra of PCPDTBT in PCPDTBT/P3M4HT blend films with varying amounts of PCPDTBT, spin-coated from CB solution, and measured at room temperature. The weight percentage (wt.%) of PCPDTBT in the blend films varies from 100 (black line), 50 (blue line), 20 (light blue line), 10 (green line), and 5 (red line).

3.3.2.   Optical characterization of PCPDTBT in neat and PCPDTBT/P3M4HT blend films

Figure 3-2 shows the characterization of PCPDTBT in neat and blend films. The black line is the absorption spectrum of the PCPDTBT neat film. The neat film shows a primary absorption peak at 770 nm and a less-intense vibronic progression at around 700 nm. When the absorption of the film compared with that of the solution at room temperature, a broadening of

the spectrum and a red-shift of the primary absorption peak from 723 nm (in solution) to 770 nm (in the film) are observed. This red-shift of the absorption peak has been associated with either interchain π-stacking or chain planarization, which would be accompanied by transitions into the solid-state.[29] Next, the absorption spectra of PCPDTBT in the blend films were investigated. Upon blending with P3M4HT, the absorption of PCPDTBT varied. The primary absorption peak at 770 nm was shifted only slightly, while the absorption intensity at shorter wavelengths of 500 – 750 nm dropped. The spectral evolution became noticeable when the proportion of PCPDTBT in the blend was decreased. Consequently, in the PCPDTBT blend film with 5 wt.%, the spectral width of PCPDTBT became much narrower, exhibiting the main absorption band at ~770 nm and a shoulder at ~700 nm.

The relative drop in absorption intensity at the wavelengths corresponds to the absorption band of disordered PCPDTBT chains, as evidenced by the solution absorption at 110 °C in **Figure 3-2a**. Therefore, the spectral change in blend films shows that the fraction of disordered PCPDTBT decreases by blending with a P3M4HT matrix. We estimated the absorption-coefficient (α) of PCPDTBT in neat and the blend films using the **Equation 3-1**.

$$\alpha = \frac{\text{Absorbance}}{0.434 l_{\text{film}} \phi} \qquad \text{\textbf{Equation 3-1}}$$

The film thickness was the total thickness of a blend film and ϕ is a volume fraction of PCPDTBT in the blend film. Here, we used a weight fraction of PCPDTBT instead of the volume fraction ϕ, under the assumption that PCPDTBT and P3M4HT have the same density. The resulting α spectra were shown in **Figure 3-3**. The spectral change represents PCPDTBT chains from a mixture of disordered and aggregated in the neat film to more aggregated when it is diluted by blending with P3M4HT.

It is important to note further note that PCPDTBT absorption in the 5 wt.% blend film is well described by the absorption of aggregated PCPDTBT chains, which has been estimated by Scharsich et al. by applying Franck-Condon analysis for PCPDTBT neat film absorption[39] (see

36

Appendix, **Figure A3-3**). Using the aggregate forms of the absorption bands as a reference, it is possible to separate the absorption spectra shown in **Figure 3-2** into superpositions of absorption by the non-aggregated disordered phase and the aggregated phase of PCPDTBT. From this spectral decomposition, the fraction of PCPDTBT chains that form aggregates in each blend film was determined. The results from the spectral decomposition are shown in **Figure 3-4** (also see Appendix, **Figure A3-4**). The fraction of aggregates gradually increase from 51% in the neat film to 84% in the blend film, by diluting the PCPDTBT with P3M4HT down to 5 wt.%. These PCPDTBT aggregation observations of the polymer/polymer blend film were opposite to the behavior that has been observed when PCPDTBT is mixed with a low-molecular-weight fullerene derivative such as PCBM: in an as-cast PCPDTBT/PCBM blend film spin-coated from a CB solution, the interchain packing and aggregation of PCPDTBT is disrupted.[30] This matrix-assisted enhancement of PCPDTBT aggregation should also be fundamentally different from the attainment of higher-order polymer chains in neat film processed with high-boiling additives in the spin-coating solution.[29,31] An approach aided by the use of an additive can facilitate the ordering of PCPDTBT chains, but in the neat film, the disordered phase still accounts for 55%.[31]
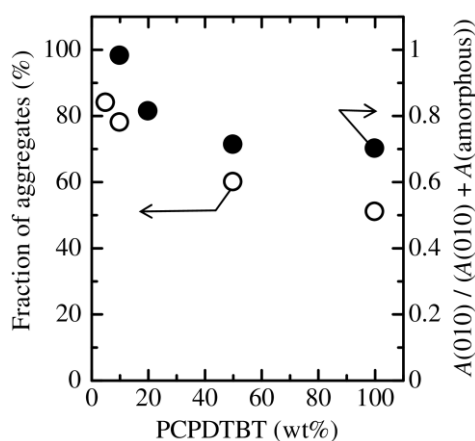
Figure 3-4. Open circles show a fraction of aggregated PCPDTBT chains as a function of the PCPDTBT weight percentage in PCPDTBT/P3M4HT blend films, as determined from UV-vis absorption spectra. Closed circles show the relative ordering of PCPDTBT chains estimated from GIWAXS profiles.

3.3.3. GIWAX measurements of PCPDTBT neat and PCPDTBT/P3M4HT blend films

To further investigate the solid-state microstructures of PCPDTBT, GIWAXS measurements were applied to the neat and blend films. For each 2-D GIWAXS image of the films, out-of-plane and in-plane 1-D GIWAXS profiles were constructed by integrating the intensity at each q value over an azimuth range of 70–110° for the out-of-plane profile and 2–22° for the in-plane profile. **Figure 3-5** shows the out-of-plane and in-plane GIWAXS profiles for PCPDTBT neat film and those for the PCPDTBT blend films. The profiles were obtained from the 2-D GIWAXS image created by subtracting the background diffraction pattern that contained amorphous P3M4HT from the total diffraction pattern of each blend film (see Appendix, **Figure A3-5**). The resulting profiles were then fitted by a superposition of Lorentzian-shaped peaks for the ordered phase (solid red lines) and Gaussian-shaped peaks for the disordered phase (solid green lines). The positions and full width at half maximum (FWHM) linewidths of the diffraction peaks are summarized in **Table A3-1** and **Table A3-2** (see Appendix). The spacings d were calculated from the center positions of the Lorentzian-shaped peaks q via $d = 2\pi/q$. The coherence length L_c was estimated from the Scherrer equation **Equation 3-2** by the FWHM value, which determined from the fit and assuming the shape factor K to be 0.9.[32,33]

$$L_c = \frac{2\pi K}{\text{FWHM}}$$ **Equation 3-2**

First, the PCPDTBT neat film diffraction peaks were assigned based on the previous reports. In the out-of-plane profile, the (100) diffraction peak was observed at $q_z = 5.69$ nm^{-1}, which corresponds to a lattice spacing of $d = 1.11$ nm. This distance was taken along the lamellar stacking direction.[30,34] An out-of-plane (010) peak was also present at $q_z = 16.50$ nm^{-1}, which corresponded to $d = 0.38$ nm and was associated with the interchain π-π stacking direction.[30,34] Additionally, broad scattering at $q_z = 14 \sim 15$ nm^{-1} was observed, which was associated with the scattering from the disordered phase of PCPDTBT.[35,36] In the in-plane profile, the (010)

peak and scattering from the disordered phase were observed. Furthermore, two additional

peaks were present at q_{xy} = 5.85 nm^{-1} and q_{xy} = 10.61 nm^{-1}, which correspond to distances of

d = 1.08 nm and 0.59 nm, respectively. These peaks were not assigned to diffraction from

lamellar stacking, but have been assigned (001) and (002) from the repetition of the monomer

along the chain backbone.[34,37] This assignment is also consistent with the fact that the (001)

distance of 1.08 nm is nearly identical to the length of the PCPDTBT repeat unit calculated

from the density functional theory (1.07 nm) (see Appendix, **Figure A3-6**).
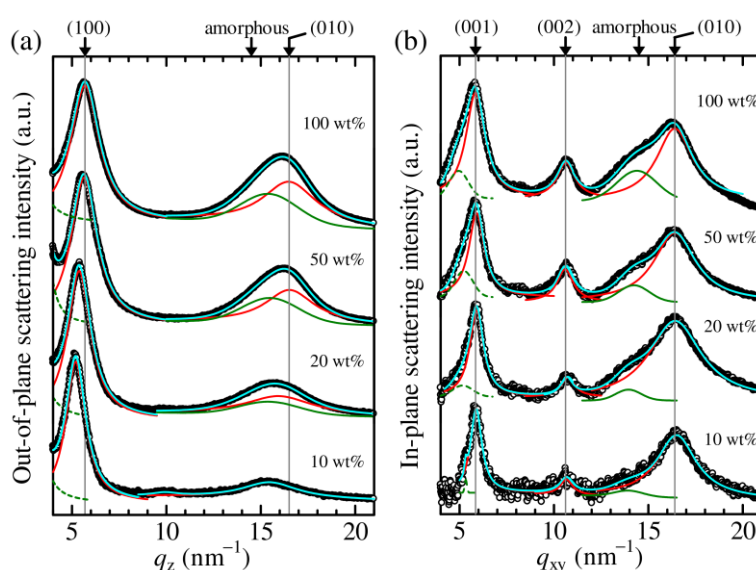
Figure 3-5. Integrated GIWAXS data (black circles) obtained from PCPDTBT neat film and PCPDTBT/P3M4HT blend films. (a) 70–110° azimuth integration for out-of-plane profile and (b) 2–22° azimuth integration for an in-plane profile. PCPDTBT contents from top to bottom: 100 wt.%, 50 wt.%, 20 wt.%, and 10 wt.%. The red and green solid lines show fitting results of individual peaks extracted from the fit (light blue solid lines) over the entire q-range measured. The broken green lines are unknown backgrounds.

Next, the PCPDTBT diffraction peaks in the blend films were characterized. The diffraction

peaks of the PCPDTBT neat film varied with P3M4HT blending. The position of the (100)

peak shifted to lower q values, and the FWHM of the peak became sharper than that in the neat

film. The (001) and (002) peaks also became shaper while their positions remained the same

as in the PCPDTBT neat film. The (010) peak underwent different changes between the out-

of-plane and in-plane profile. In the out-of-plane profile, the relative intensity of the (010) peak became weaker when compared to that of the (100) peak. On the other hand, In the in-plane profile, the (010) diffraction peak remained independent of the blending weight ratio. These results suggest that in the lower PCPDTBT concentration blend film, an edge-on structure with alkyl side chains aligned perpendicularly to the substrate becomes dominant.

Figure 3-6 shows the dependence of the d-value and the correlation length L_c on the PCPDTBT blend weight ratio. The d values of the (100) lamellar stacking expanded from 1.11 to 1.21 nm as the PCPDTBT concentration decreased to 10 wt.%, while the d-values of both the (010) interchain π-π stacking and the (001) chain backbone repeat changed only slightly. As for the correlation lengths, the L_c values in the (100) lamella stacking increased from 3.01 to 4.44 nm as the PCPDTBT concentration decreased to 10 wt.%, while the L_c value of the (010) interchain π-π stacking remained almost the same among samples. In addition, a noticeable increase in L_c values was observed for the (001) chain backbone repeat. The value was extended from 4.58 nm in PCPDTBT neat film to 7.73 nm in 10 wt.% PCPDTBT blend film.
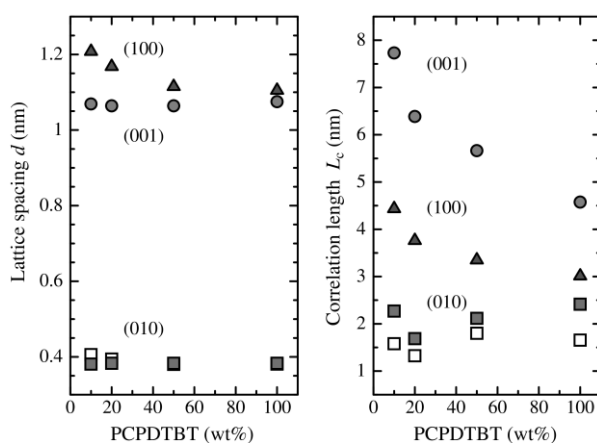
Figure 3-6. (a) Lattice spacings d and (b) correlation lengths L_c as obtained from the cake cut analysis for each 2-D GIWAXS image of PCPDTBT neat film and PCPDTBT/P3M4HT blend films. Circles: (001) mainchain backbone repeat. Triangles: (100) lamella stacking direction. Squares: (010) interchain π-π stacking direction. The closed squares are d and L_c values calculated from the out-of-plane (q_z) profile, and open squares are those from the in-plane (q_{xy}) profile.

Based on the d and L_c values, the microstructure of ordered PCPDTBT chains was quantified and schematically illustrated in **Figure 3-7**. The number of donor-acceptor type repeating units in an ordered part of a chain backbone (red rectangular thin-plate) and the number of stacking in the lamella and π-π stacking directions, N, were respectively estimated via $N = L_c/d$. Considering the fact that one PCPDTBT chain used in this study is composed of 37 repeated units, several intra-chain (single-chain) aggregates would participate in the lamellar and the π-π stacking. It can be concluded that, in the neat film, PCPDTBT forms a short-range ordered structure comprised of the alignment of a few repeat units in the chain backbone and the stacking of a few chains in both the lamellar and π-π stacking directions. The stacked aggregates primarily extended along the main chain backbone from ~4 repeat units in the neat film to ~7 repeat units in the blend film of 10 wt.% PCPDTBT on average. It grew in size along the lamellar stacking direction from ~3 stacks in the neat film to ~4 stacks in the blend film of 10 wt.% PCPDTBT on average.
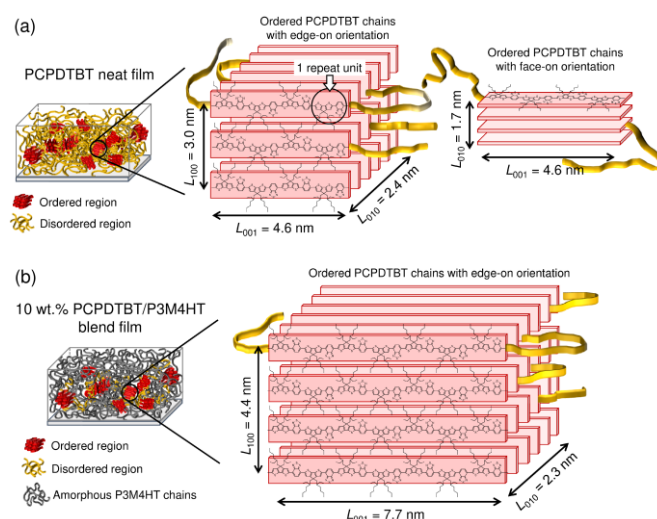
Figure 3-7. The dimensions of the ordered PCPDTBT chains (a) in neat film and (b) in PCPDTBT/P3M4HT blend film containing 10 wt.% PCPDTBT, determined by GIWAXS analysis. For the schematics, each red rectangular thin plate indicates ordered parts of a chain backbone participating in single- and multichain aggregates. Disordered parts in the same chain backbone (yellow band-like lines) that may bridge ordered parts and those that may wander successively through a series of ordered and disordered regions are almost omitted.

Finally, the diffraction from the disordered state of PCPDTBT was observed. As evidenced by **Figure 3-5**, scattering from the disordered phase ($q_z = 1.4 \sim 1.5$ nm^{-1}) became weaker in both out-of-plane and in-plane profiles after blending with P3M4HT, and the scattering was negligible in the 10 wt.% blend film. This continuous change indicates that the solid-state ordering of PCPDTBT chains is improved by blending with P3M4HT. The relative ordering was characterized in terms of a scattered intensity ratio of the (010) interchain π-π stacking to the sum of the scattered intensity from the (010) interchain π-π stacking and disordered phase To examine the impact of blending on the ordering of PCDTBT; each scattered intensity was calculated from the fitting results for the in-plane and out-of-plane GIWAXS profiles shown in **Figure 3-5**. This metric does not permit direct estimation of the ordered phase mass. However, it does give a qualitative assessment of the loss of disordered-state PCPDTBT in the blend films as has been plotted by closed circles in **Figure 3-4**. this information from GIWAXS data confirm that aggregation and ordering of PCPDTBT chains are enhanced upon blending with the P3M4HT matrix polymer, with a continuous reduction of the disordered PCPDTBT phase.

3.3.4. Effects of matrix polymers on aggregation

The UV-vis absorption spectra of PCPDTBT were examined in the blend films with other amorphous matrix polymers. Different types of insulating amorphous polymers, PS and PMMA, were used to study the generality of the aggregate enhancement by blending with polymer matrices. As shown in **Figure 3-8**, absorption intensity at shorter wavelengths of 500 – 750 nm decreased in the blend films. The drop indicates that aggregation is enhanced in blend films with PS and PMMA, which are similar to the blend film with P3M4HT. Further observations show that interactions between PCPDTBT and P3M4HT are not expected to be a driving force behind the aggregation enhancement. Instead, the results indicate that

enhancement generally occurs for films spin-coated from polymer/polymer blend solution where PCPDTBT is diluted with dissimilar polymers. Here, the term 'dissimilar polymer' was used to refer polymers, which show a positive value of free energy of mixing with PCPDTBT due to small entropy of mixing of long polymer chains and a positive value of Flory-Huggins interaction parameter χ for the PCPDTBT/polymer. The AFM images of the blend films suggested that a thin layer of highly-ordered PCPDTBT chains is not formed on the film surface. The constituent polymers are likely to be phase-separated laterally in the PCPDTBT/P3M4HT and PCPDTBT/PMMA blend films (see Appendix A3-9). The morphology differs from the vertical phase-separated results which have been typically reported for the conjugated polymer/insulating polymer blends in OFETs application.[14,15,21,38]
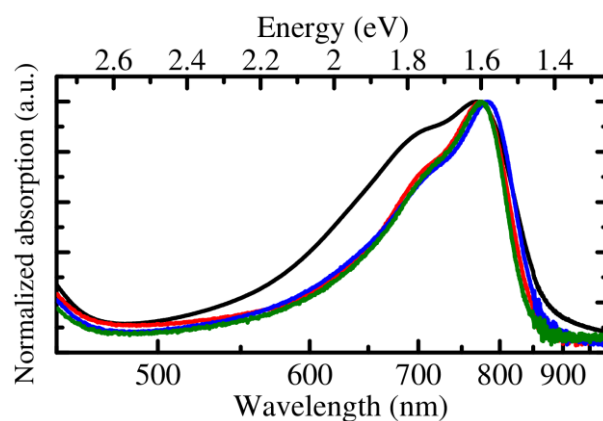
Figure 3-8. UV-vis absorption spectra of PCPDTBT in the neat film (black) and of PCPDTBT in blend films with PMMA (blue), PS (green), and P3M4HT (red) spin-coated from DCB solution. The weight percentage of the PCPDTBT in the blend films was 10 wt.%. The spectra were normalized to a peak intensity of 1.

Under the assumption that higher concentrations will increase the possibility of forming inter-chain aggregations, a PCPDTBT neat film was prepared by spin-coating from a CB solution of PCPDTBT in a concentration of up to 40 mg ml^{-1}. The neat film was melted at 310 °C for 15 min and solidified again from its molten state via natural cooling. **Figure 3-9** shows the resulting absorption spectra of the PCPDTBT neat films. For film spin-coated from

high concentration, the degree of aggregation decreased to 42%, as evidenced by the increase in absorption intensity for the wavelength range of 500–700 nm. Furthermore, for film solidified from the molten state, the absorption peak blue-shifted, and the spectrum became broader and less structured, indicating higher disordered morphology. Given that chain entanglement is most significant in the molten state, these spectral changes suggest that the crowding contact or entanglement of PCPDTBT chains during solidification hampers the formation of ordered inter-chain aggregation.
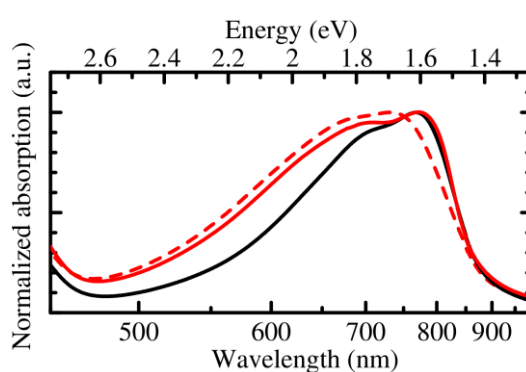
Figure 3-9. UV-vis absorption spectrum of PCPDTBT neat films spin-coated from 40 mg ml^{-1} of CB solution (solid red line) and the absorption spectrum obtained after it was melted (dashed red line). The solid black line is the spectrum of PCPDTBT neat film spin-coated from 10 mg ml^{-1} of CB solution. These spectra were measured at room temperature and normalized according to peak intensity.

3.3.5.   Current images of PSBTBT neat film and PSBTBT/P3M4HT blend film

The fraction of aggregates in the weakly-ordered PCPDTBT conjugated polymers is increased by blending. This increase is visible in the decreasing I_2 intensity in the UV-vis absorption spectra. The identical phenomena had been observed in the blend film of PSBTBT/P3M4HT. **Figure 3-10** shows an example of a current image comparison between PSBTBT neat film and PSBTBT/P3M4HT blend films.

The inhomogeneous current image of the blend film is due to the blending with the matrix polymer (P3M4HT). P3M4HT does not flow current, and therefore a blue-colored area in the

image is expected to be a matrix domain. On the contrary, interconnected-enhanced aggregates of PSBTBT flow higher current than the surrounding area and pictured as a red-colored region. This comparison of current images is the proof of better charge transport, which comes from a better aggregation of the donor polymer in the blend film.
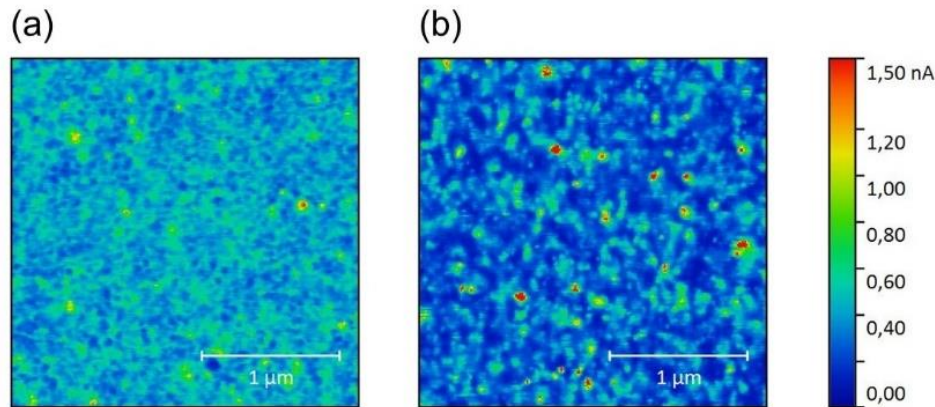
Figure 3-10. Current images of (a) PSBTBT neat film and (b) 20 wt.% of PSBTBT/P3M4HT blend film. Measured at +4 V applied voltage to the substrate electrode

In the PSBTBT/P3M4HT blend, PSBTBT is responsible for material for charge transport. Therefore, the effective current flowing through PSBTBT in the blend should be calculated by considering the weight ratio of PSBTBT in the blend as:

$$\text{Enhanced factor} = \frac{\frac{1}{0.2} \times I_{av} \text{ of Blend film}}{I_{av} \text{ of neat film}} \qquad \textbf{Equation 3-3}$$

The enhanced factor 1 means there is no enhancement in hole current by blending, while enhanced factor lower than 1 means there is current loss by blending. However, an enhanced factor higher than 1 means there is a current enhancement by blending. The current image from C-AFM measurement shows that the enhancement factor is 3.6, which means that current flowing through PSBTBT in blend film is larger than in the neat films. This increase in charge transport would come from a better aggregation of the PSBTBT in the blend film.

3.4. Discussion

Our collected set of observations suggests that short-range ordering in the form of aggregates increases when the presence of a matrix polymer weakens the crowding contact between PCPDTBT chains. Considering this matrix-assisted enhancement mechanism, our current understanding of the process is schematically depicted in **Figure 3-11**. In the PCPDTBT/solvent binary solution, PCPDTBT would form intra-chain (single-chain) aggregations in dilute solution, which have also been proposed for other weakly-ordered conjugated polymers.[24,39–41] The intra-chain aggregation that induced molecular-level ordering would be perturbed due to the chain overlap and chain interpenetration that unavoidably occur when the solution is highly concentrated in the course of solvent evaporation.[42,43] Consequently, the disordered part in a polymer chain would be increased in the concentrated solution. Therefore, the PCPDTBT neat film is simultaneously composed of not only aggregating and locally ordered stacking (red) but also disordered chains (yellow).

On the other hand, for a PCPDTBT/matrix polymer/solvent ternary solution, matrix polymer chain coils do not freely overlap and interpenetrate the PCPDTBT chain coil due to the enthalpic repulsions between the dissimilar polymer chains. The matrix polymer is expected to act as a buffer that prevents the undesired interpenetration or entanglement of PCPDTBT chains when the solution is concentrated to the point where PCPDTBT coils overlap each other. The partially segregated configuration of dissimilar coils is translated into the solid-state before complete phase separation of the blended polymers. Consequently, the PCPDTBT spin-coated from a PCPDTBT/matrix polymer/solvent ternary solution can retain intra-chain order, which then constitutes lamellar-stacked multichain aggregates in the film.

Structural disordering of PCPDTBT in the blend films with a low-molecular-weight fullerene derivative, such as PCBM, has been studied thoroughly.[29,30,34–36,44] When PCPDTBT is blended with PCBM and subsequently spin-coated from the CB solution, the packing and

aggregation of PCPDTBT chains are disrupted, as evidenced by the loss of the (010) diffraction peak and the structureless UV-vis absorption spectrum with a peak blue-shifted to around 740 nm.[30] The effects of matrix polymer presence can be compared to the negative effects resulting from blending with a small molecule as a matrix. In the case of PCPDTBT/PCBM/solvent ternary solution, the low-molecular-weight matrix may penetrate the PCPDTBT coil domain due to the significant difference in molecular weight[45] and hence relatively higher entropy of mixing, disrupting the molecular-level ordering of PCPDTBT.

The morphological change observed in the PCPDTBT/P3M4TH blend films, where the short-range ordering is enhanced, is significant to improve charge carrier mobility and optoelectronic functionality of thin-film devices, including weakly-ordered conjugated polymers. This enhancement was reflected in the enhancement factor value from the current images when measured at negative and positive applied voltage.   Similar enhancing results measured for the PCPDTBT blend films using insulating amorphous polymers PMMA and PS affirm the importance of our proposed matrix-mediated process. From the viewpoint of OSC application, research on the control of short-range ordering should be shifted from PCPDTBT/polymer blend films using P3M4HT to the films using a conjugated polymer that forms type-II heterojunctions.[46] Nevertheless, as revealed by the PCPDTBT/P3M4HT blends, understanding of the process that facilitates molecular-level self-assembly of a weakly-ordered conjugated polymer should have significant implications for the design of polymer/polymer blend OSCs, where low-bandgap donor-acceptor conjugated polymers[23,24] are used as a hole and electron transport materials with various blend ratios.[47]

Increase in polymer concentration by solvent evaporation

(a) PDPDTBT/solvent binary solution

(b) PDPDTBT/matrix polymer/solvent ternary solution

Initial dilute solution   Concentrated solution   Film
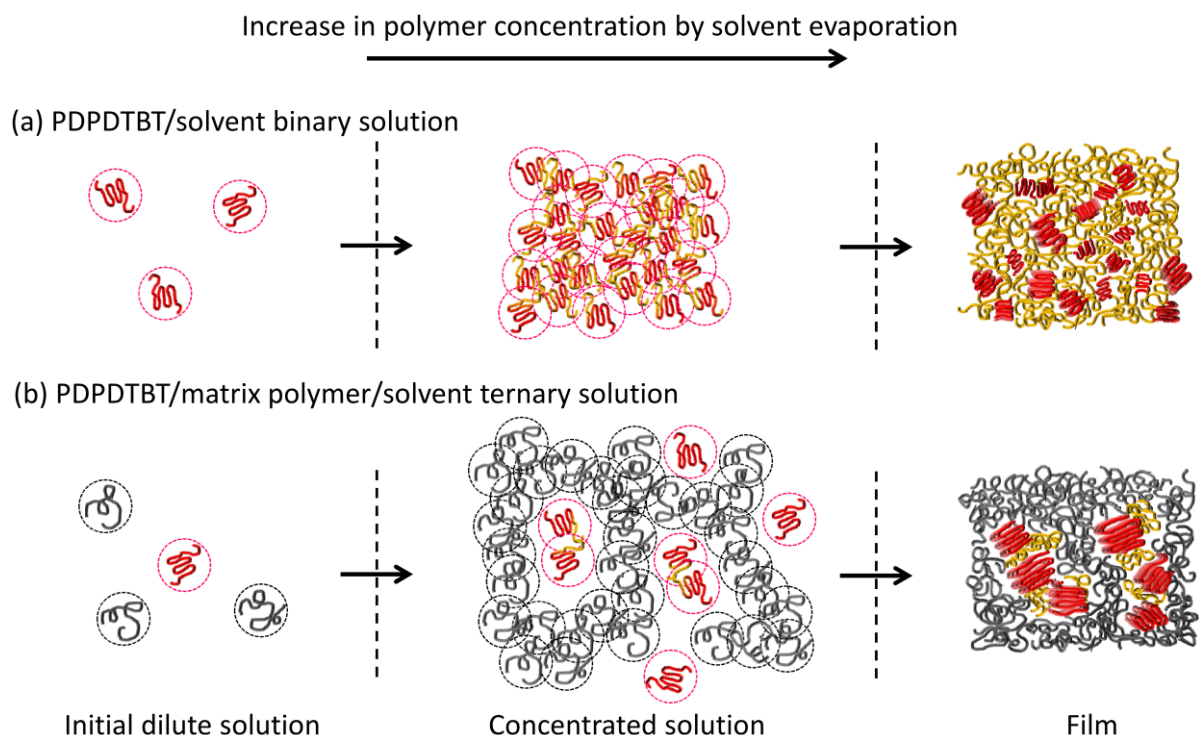
Figure 3-11. Schematic presentation of the microstructural evolution occurring in the spin-coating of (a) PCPDTBT/solvent binary and (b) PCPDTBT/matrix polymer/solvent ternary solutions. Intra-chain and inter-chain aggregations of PCPDTBT are shown in red, and the disordered state of PCPDTBT is shown in yellow. The matrix polymer chain is shown in gray. Solvent molecules are omitted. In the binary solution, the overlapping and interpenetration of coils disturb the molecular-level ordering of the intra-chain aggregation, resulting in an increase in the disordered state of PCPDTBT in the film. In the ternary solution, when the concentration reaches a point where the distance between the coils of PCPDTBT and a matrix polymer chain is equivalent to their diameters, incompatibility acts strongly against overlapping. As a result, PCPDTBT chains retain the molecular-level ordering of the intra-chain aggregation, which then constitutes multichain aggregates in the film.

3.5. Conclusion

The change in the short-range ordered structure (aggregates) of the weakly-ordered conjugated polymer has been investigated for the blend films. The aggregates were increased in the fraction and the size gradually after blending. The fraction of aggregates gradually increases from 0.51 in the neat film to 0.84 in the blend film. The size of aggregates in neat films is about ~4 repeat units and ~3 stacks in the backbone and lamellar stacking direction, respectively. In the 10 wt.% blend film, the aggregates are about ~7 repeat units and ~4 stacks

in the backbone and lamellar stacking direction. Also, C-AFM current images suggested that the current flowing through PSBTBT in the blend film is higher than in the neat film.

3.6. Reference

(1)   Yang, J.; Zhao, Z.; Wang, S.; Guo, Y.; Liu, Y. Insight into High-Performance Conjugated Polymers for Organic Field-Effect Transistors. *Chem* **2018**, *4* (12), 2748–2785. https://doi.org/10.1016/j.chempr.2018.08.005.

(2)   Kim, M.; Ryu, S. U.; Park, S. A.; Choi, K.; Kim, T.; Chung, D.; Park, T. Donor–Acceptor-Conjugated Polymer for High-Performance Organic Field-Effect Transistors: A Progress Report. *Adv. Funct. Mater.* **2020**, *30* (20), 1–25. https://doi.org/10.1002/adfm.201904545.

(3)   Paterson, A. F.; Singh, S.; Fallon, K. J.; Hodsden, T.; Han, Y.; Schroeder, B. C.; Bronstein, H.; Heeney, M.; McCulloch, I.; Anthopoulos, T. D. Recent Progress in High-Mobility Organic Transistors: A Reality Check. *Adv. Mater.* **2018**, *30* (36), 1–33. https://doi.org/10.1002/adma.201801079.

(4)   Lee, C.; Lee, S.; Kim, G. U.; Lee, W.; Kim, B. J. Recent Advances, Design Guidelines, and Prospects of All-Polymer Solar Cells. *Chem. Rev.* **2019**, *119* (13), 8028–8086. https://doi.org/10.1021/acs.chemrev.9b00044.

(5)   Benten, H.; Mori, D.; Ohkita, H.; Ito, S. Recent Research Progress of Polymer Donor/Polymer Acceptor Blend Solar Cells. *J. Mater. Chem. A* **2016**, *4* (15), 5340–5365. https://doi.org/10.1039/c5ta10759h.

(6)   Zen, A.; Pflaum, J.; Hirschmann, S.; Zhuang, W.; Jaiser, F.; Asawapirom, U.; Rabe, J. P.; Scherf, U.; Neher, D. Effect of Molecular Weight and Annealing of Poly(3-Hexylthiophene)s on the Performance of Organic Field-Effect Transistors. *Adv. Funct. Mater.* **2004**, *14* (8), 757–764. https://doi.org/10.1002/adfm.200400017.

(7)   Bao, Z.; Dodabalapur, A.; Lovinger, A. J. Soluble and Processable Regioregular Poly(3-Hexylthiophene) for Thin Film Field-Effect Transistor Applications with High Mobility. *Appl. Phys. Lett.* **1996**, *69* (26), 4108–4110. https://doi.org/10.1063/1.117834.

(8)   Bechgaard, K.; Spiering, A. J. H. Two-Dimensional Charge Transport in Conjugated Polymers. *October* **1999**, No. c, 685–688.

(9)   McCulloch, I.; Heeney, M.; Bailey, C.; Genevicius, K.; MacDonald, I.; Shkunov, M.; Sparrowe, D.; Tierney, S.; Wagner, R.; Zhang, W.; et al. Liquid-Crystalline Semiconducting Polymers with High Charge-Carrier Mobility. *Nat. Mater.* **2006**, *5* (4), 328–333. https://doi.org/10.1038/nmat1612.

(10)   Mcculloch, I.; Heeney, M.; Chabinyc, M. L.; Delongchamp, D.; Kline, R. J.; Cölle, M.; Duffy, W.; Fischer, D.; Gundlach, D.; Hamadani, B.; et al. Semiconducting Thienothiophene Copolymers: Design, Synthesis, Morphology, and Performance in Thin-Film Organic Transistors. *Adv. Mater.* **2009**, *21* (10–11), 1091–1109. https://doi.org/10.1002/adma.200801650.

(11)   Abbaszadeh, D.; Kunz, A.; Wetzelaer, G. A. H.; Michels, J. J.; Craciun, N. I.; Koynov, K.; Lieberwirth, I.; Blom, P. W. M. Elimination of Charge Carrier Trapping in Diluted Semiconductors. *Nat. Mater.* **2016**, *15* (6), 628–633. https://doi.org/10.1038/nmat4626.

(12)   Goffri, S.; Müller, C.; Stingelin-Stutzmann, N.; Breiby, D. W.; Radano, C. P.; Andreasen, J. W.; Thompson, R.; Janssen, R. A. J.; Nielsen, M. M.; Smith, P.; et al. Multicomponent Semiconducting Polymer Systems with Low Crystallization- Induced Percolation Threshold. *Nat. Mater.* **2006**, *5* (12), 950–956. https://doi.org/10.1038/nmat1779.

(13)   Lei, Y.; Deng, P.; Lin, M.; Zheng, X.; Zhu, F.; Ong, B. S. Enhancing Crystalline Structural Orders of Polymer Semiconductors for Efficient Charge Transport via Polymer-Matrix-Mediated Molecular Self-Assembly. *Adv. Mater.* **2016**, *28* (31), 6687–6694. https://doi.org/10.1002/adma.201600580.

(14)   Ford, M. J.; Wang, M.; Patel, S. N.; Phan, H.; Segalman, R. A.; Nguyen, T. Q.; Bazan, G. C. High Mobility Organic Field-Effect Transistors from Majority Insulator Blends. *Chem. Mater.* **2016**, *28* (5), 1256–1260. https://doi.org/10.1021/acs.chemmater.5b04774.

(15) Qiu, L.; Lim, J. A.; Wang, X.; Lee, W. H.; Hwang, M.; Cho, K. Versatile Use of Vertical-Phase-Separation-Induced Bilayer Structures in Organic Thin-Film Transistors. *Adv. Mater.* **2008**, *20* (6), 1141–1145. https://doi.org/10.1002/adma.200702505.

(16) Osaka, M.; Benten, H.; Ohkita, H.; Ito, S. Intermixed Donor/Acceptor Region in Conjugated Polymer Blends Visualized by Conductive Atomic Force Microscopy. *Macromolecules* **2017**, *50* (4), 1618–1625. https://doi.org/10.1021/acs.macromol.6b02604.

(17) Osaka, M.; Mori, D.; Benten, H.; Ogawa, H.; Ohkita, H.; Ito, S. Charge Transport in Intermixed Regions of All-Polymer Solar Cells Studied by Conductive Atomic Force Microscopy. *ACS Appl. Mater. Interfaces* **2017**, *9* (18), 15615–15622. https://doi.org/10.1021/acsami.7b00979.

(18) Liu, X.; Huettner, S.; Rong, Z.; Sommer, M.; Friend, R. H. Solvent Additive Control of Morphology and Crystallization in Semiconducting Polymer Blends. *Adv. Mater.* **2012**, *24* (5), 669–674. https://doi.org/10.1002/adma.201103097.

(19) Yan, H.; Collins, B. A.; Gann, E.; Wang, C.; Ade, H.; McNeill, C. R. Correlating the Efficiency and Nanomorphology of Polymer Blend Solar Cells Utilizing Resonant Soft X-Ray Scattering. *ACS Nano* **2012**, *6* (1), 677–688. https://doi.org/10.1021/nn204150f.

(20) Noriega, R.; Rivnay, J.; Vandewal, K.; Koch, F. P. V.; Stingelin, N.; Smith, P.; Toney, M. F.; Salleo, A. A General Relationship between Disorder, Aggregation and Charge Transport in Conjugated Polymers. *Nat. Mater.* **2013**, *12* (11), 1038–1044. https://doi.org/10.1038/nmat3722.

(21) Wang, S.; Fabiano, S.; Himmelberger, S.; Puzinas, S.; Crispin, X.; Salleo, A.; Berggren, M. Experimental Evidence That Short-Range Intermolecular Aggregation Is Sufficient for Efficient Charge Transport in Conjugated Polymers. *Proc. Natl. Acad. Sci. U. S. A.* **2015**, *112* (34), 10599–10604. https://doi.org/10.1073/pnas.1501381112.

(22) Hammond, M. R.; Kline, R. J.; Herzing, A. A.; Richter, L. J.; Germack, D. S.; Ro, H. W.; Soles, C. L.; Fischer, D. A.; Xu, T.; Yu, L.; et al. Molecular Order in High-Efficiency Polymer/Fullerene Bulk Heterojunction Solar Cells. *ACS Nano* **2011**, *5* (10), 8248–8257. https://doi.org/10.1021/nn202951e.

(23) Root, S. E.; Jackson, N. E.; Savagatrup, S.; Arya, G.; Lipomi, D. J. Modelling the Morphology and Thermomechanical Behaviour of Low-Bandgap Conjugated Polymers and Bulk Heterojunction Films. *Energy Environ. Sci.* **2017**, *10* (2), 558–569. https://doi.org/10.1039/c6ee03456j.

(24) Jackson, N. E.; Kohlstedt, K. L.; Savoie, B. M.; Olvera De La Cruz, M.; Schatz, G. C.; Chen, L. X.; Ratner, M. A. Conformational Order in Aggregates of Conjugated Polymers. *J. Am. Chem. Soc.* **2015**, *137* (19), 6254–6262. https://doi.org/10.1021/jacs.5b00493.

(25) Peet, J.; Kim, J. Y.; Coates, N. E.; Ma, W. L.; Moses, D.; Heeger, A. J.; Bazan, G. C. Efficiency Enhancement in Low-Bandgap Polymer Solar Cells by Processing with Alkane Dithiols. *Nat. Mater.* **2007**, *6* (7), 497–500. https://doi.org/10.1038/nmat1928.

(26) Koppe, M.; Egelhaaf, H. J.; Dennler, G.; Scharber, M. C.; Brabec, C. J.; Schilinsky, P.; Hoth, C. N. Near IR Sensitization of Organic Bulk Heterojunction Solar Cells: Towards Optimization of the Spectral Response of Organic Solar Cells. *Adv. Funct. Mater.* **2010**, *20* (2), 338–346. https://doi.org/10.1002/adfm.200901473.

(27) MacHui, F.; Rathgeber, S.; Li, N.; Ameri, T.; Brabec, C. J. Influence of a Ternary Donor Material on the Morphology of a P3HT:PCBM Blend for Organic Photovoltaic Devices. *J. Mater. Chem.* **2012**, *22* (31), 15570–15577. https://doi.org/10.1039/c2jm31882b.

(28) Watts, B.; Schuettfort, T.; McNeill, C. R. Mapping of Domain Orientation and Molecular Order in Polycrystalline Semiconducting Polymer Films with Soft X-Ray Microscopy. *Adv. Funct. Mater.* **2011**, *21* (6), 1122–1131. https://doi.org/10.1002/adfm.201001918.

(29) Peet, J.; Cho, N. S.; Lee, S. K.; Bazan, G. C. Transition from Solution to the Solid State

in Polymer Solar Cells Cast from Mixed Solvents. *Macromolecules* **2008**, *41* (22), 8655–8659. https://doi.org/10.1021/ma801945h.

(30)   Gu, Y.; Wang, C.; Russell, T. P. Multi-Length-Scale Morphologies in PCPDTBT/PCBM Bulk-Heterojunction Solar Cells.Pdf. *Adv. Energy Mater.* **2012**, *2*, 683–690. https://doi.org/10.1002/aenm.201100726.

(31)   Scharsich, C.; Fischer, F. S. U.; Wilma, K.; Hildner, R.; Ludwigs, S.; Köhler, A. Revealing Structure Formation in PCPDTBT by Optical Spectroscopy. *J. Polym. Sci. Part B Polym. Phys.* **2015**, *53* (20), 1416–1430. https://doi.org/10.1002/polb.23780.

(32)   Smilgies, D. M. Scherrer Grain-Size Analysis Adapted to Grazing-Incidence Scattering with Area Detectors. *J. Appl. Crystallogr.* **2009**, *42* (6), 1030–1034. https://doi.org/10.1107/S0021889809040126.

(33)   Rivnay, J.; Mannsfeld, S. C. B.; Miller, C. E.; Salleo, A.; Toney, M. F. Quantitative Determination of Organic Semiconductor Microstructure from the Molecular to Device Scale. *Chem. Rev.* **2012**, *112* (10), 5488–5519. https://doi.org/10.1021/cr3001109.

(34)   Agostinelli, T.; Ferenczi, T. A. M.; Pires, E.; Foster, S.; Maurano, A.; Müller, C.; Ballantyne, A.; Hampton, M.; Lilliu, S.; Campoy-Quiles, M.; et al. The Role of Alkane Dithiols in Controlling Polymer Crystallization in Small Band Gap Polymer: Fullerene Solar Cells. *J. Polym. Sci. Part B Polym. Phys.* **2011**, *49* (10), 717–724. https://doi.org/10.1002/polb.22244.

(35)   Rogers, J. T.; Schmidt, K.; Toney, M. F.; Kramer, E. J.; Bazan, G. C. Structural Order in Bulk Heterojunction Films Prepared with Solvent Additives. *Adv. Mater.* **2011**, *23* (20), 2284–2288. https://doi.org/10.1002/adma.201003690.

(36)   Buss, F.; Schmidt-Hansberg, B.; Sanyal, M.; Munuera, C.; Scharfer, P.; Schabel, W.; Barrena, E. Gaining Further Insight into the Solvent Additive-Driven Crystallization of Bulk-Heterojunction Solar Cells by in Situ X-Ray Scattering and Optical Reflectometry.

Macromolecules **2016**, *49* (13), 4867–4874. https://doi.org/10.1021/acs.macromol.6b00193.

(37)   Fischer, F. S. U.; Trefz, D.; Back, J.; Kayunkid, N.; Tornow, B.; Albrecht, S.; Yager, K. G.; Singh, G.; Karim, A.; Neher, D.; et al. Highly Crystalline Films of PCPDTBT with Branched Side Chains by Solvent Vapor Crystallization: Influence on Opto-Electronic Properties. *Adv. Mater.* **2015**, *27* (7), 1223–1228. https://doi.org/10.1002/adma.201403475.

(38)   Nikzad, S.; Wu, H. C.; Kim, J.; Mahoney, C. M.; Matthews, J. R.; Niu, W.; Li, Y.; Wang, H.; Chen, W. C.; Toney, M. F.; et al. Inducing Molecular Aggregation of Polymer Semiconductors in a Secondary Insulating Polymer Matrix to Enhance Charge Transport. *Chem. Mater.* **2020**, *32* (2), 897–905. https://doi.org/10.1021/acs.chemmater.9b05228.

(39)   Steyrleuthner, R.; Schubert, M.; Howard, I.; Klaumünzer, B.; Schilling, K.; Chen, Z.; Saalfrank, P.; Laquai, F.; Facchetti, A.; Neher, D. Aggregation in a High-Mobility n-Type Low-Bandgap Copolymer with Implications on Semicrystalline Morphology. *J. Am. Chem. Soc.* **2012**, *134* (44), 18303–18317. https://doi.org/10.1021/ja306844f.

(40)   Liang, Y.; Xu, Z.; Xia, J.; Tsai, S. T.; Wu, Y.; Li, G.; Ray, C.; Yu, L.; Wang, S.; Fabiano, S.; et al. Photophysical and Morphological Implications of Single-Strand Conjugated Polymer Folding in Solution. *Macromolecules* **2012**, *22* (20), 2814–2822. https://doi.org/10.1021/ma801945h.

(41)   Ren, J.; Li, X.; Ma, T.; Liu, B.; Zhang, H.; Li, T.; Lu, D. Dynamic Evolution from Chain Disorder to Order of PTB7 Condensed State Structures under External Fields. *ACS Appl. Mater. Interfaces* **2018**, *10* (33), 28093–28102. https://doi.org/10.1021/acsami.8b08938.

(42)   Daoud, M.; Cotton, J. P.; Farnoux, B.; Jannink, G.; Sarma, G.; Benoit, H.; Duplessix, C.; Picot, C.; de Gennes, P. G. Solutions of Flexible Polymers. Neutron Experiments and Interpretation. *Macromolecules* **1975**, *8* (6), 804–818.

https://doi.org/10.1021/ma60048a024.

(43) Chandran, S.; Baschnagel, J.; Cangialosi, D.; Fukao, K.; Glynos, E.; Janssen, L. M. C.; Müller, M.; Muthukumar, M.; Steiner, U.; Xu, J.; et al. Processing Pathways Decide Polymer Properties at the Molecular Level. *Macromolecules* **2019**, *52* (19), 7146–7156. https://doi.org/10.1021/acs.macromol.9b01195.

(44) Schaffer, C. J.; Schlipf, J.; Dwi Indari, E.; Su, B.; Bernstorff, S.; Müller-Buschbaum, P. Effect of Blend Composition and Additives on the Morphology of PCPDTBT:PC71BM Thin Films for Organic Photovoltaics. *ACS Appl. Mater. Interfaces* **2015**, *7* (38), 21347–21355. https://doi.org/10.1021/acsami.5b05939.

(45) Kent, M. S.; Tirrell, M.; Lodge, T. P. Solution Properties of Polymer Mixtures. *Macromolecules* **1992**, *25* (20), 5383–5397. https://doi.org/10.1021/ma00046a041.

(46) McNeill, C. R.; Greenham, N. C. Conjugated-Polymer Blends for Optoelectronics. *Adv. Mater.* **2009**, *21* (38–39), 3840–3850. https://doi.org/10.1002/adma.200900783.

(47) Benten, H.; Nishida, T.; Mori, D.; Xu, H.; Ohkita, H.; Ito, S. High-Performance Ternary Blend All-Polymer Solar Cells with Complementary Absorption Bands from Visible to near-Infrared Wavelengths. *Energy Environ. Sci.* **2016**, *9* (1), 135–140. https://doi.org/10.1039/c5ee03460d.

Chapter 4.

Morphology and Electron Transport of Conjugated Polymer Thin-Film Studied by Conductive Atomic Force Microscopy

4.1. Introduction

Designing efficient hole-transporting and electron-transporting materials are essential to establish high performance organic electronic devices such as thin-film field-effect transistors, organic light-emitting diode, and organic photovoltaics (OPV).[1–6] In the research field of OPVs, there is a growing interest in developing new electron acceptor materials, which replace the prevalent fullerene-based acceptors such as phenyl-C_{61}-butyric acid methyl ester (PCBM).[4–6] One of the most widely investigated non-fullerene electron acceptors for use in OPVs have been a perylene diimide (PDI) based small molecule[7] and polymer acceptors[8–12] due to their excellent thermal, chemical, and photochemical stabilities, in addition to the high absorption coefficient in the visible wavelength region. Furthermore, they have a large electron affinity (deep LUMO energy level), comparable to that of fullerene derivatives, showing a potential for high electron mobility in the film state. Relative to the optimal tuning of optoelectrical properties of a molecular level, achieving an excellent electron transport in the film state is still a challenge for the PDI-based acceptors because of the poor understanding about the local ordering and aggregation behavior of the molecules in the film and its contribution to the electrically conductive properties of the film.

The conductivity and mobility of the films can be evaluated by macroscopic current density-voltage measurement.[13] However, there is a large gap between the insights which could be derived from the ensemble conducting properties and the local conductive features subject to the nanoscale morphologies of the film. Thus an in-depth understanding of the correlation

57

between film morphology and the macroscopic conductive property is required for designing acceptor films to give efficient charge electron transport.

Conductive atomic force microscopy (C-AFM) can be applied as a powerful tool for characterizing the local electrical properties of the thin-films of organic semiconductors.[14–23] Especially, simultaneous mapping of topography and hole transport characteristics with a nanoscale spatial resolution has enabled the direct correlation of morphology and macroscopic charge transport properties of films, which has been inaccessible from macroscopic characterizations. To date, however, the observation of electron transport in the non-fullerene acceptors has not been performed sufficiently from the viewpoint of their morphological features at the nanometer scale.[24]

This chapter aims to elucidate the electron transport nanostructure of the weakly-ordered conjugated polymer acceptor by C-AFM. For acceptor polymers, donor-acceptor copolymers with bithiophene (PDI) unit (P(PDI-2T)) has been investigated. A low work function electrode was developed first for efficient electron injection. By using this electrode as a cathode, electron current flows through neat films of acceptors were characterized.
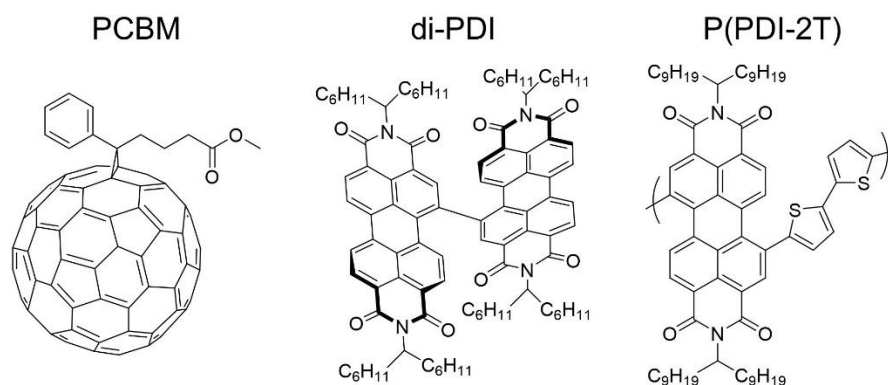
Figure 4-1. Materials for electron transport used in this chapter: (a) small molecule (PCBM), (b) dimer (di-PDI), (c) conjugated acceptor polymer P(PDI-2T), and (d) polyethyleneimine-ethoxylated (PEIE)

4.2. Experimental

4.2.1. Materials

PCBM (Frontier carbon Co.), di-PDI (1-Material Inc.), and P(PDI-2T) (1-Material Inc.) were used as acceptor materials. The acceptors were dissolved in chlorobenzene at 70°C for 12 h in the glove box; they were then used for spin-coating. The weight-average molecular weight (M_w) and polydispersity index (PDI, given by M_w/M_n, where M_n is the number-average molecular weight) provided by the Certificate of Analysis for P(PDI-2T) were > 50,000 g mol^{-1} and 2.5, respectively. A PEIE aqueous solution (35–40 wt%, M_w = 70,000 g mol^{-1}) was purchased from Aldrich Chemical Co. The aqueous solution was further diluted with 2-methoxy ethanol to a weight concentration of 2 wt%; they were then used for spin-coating. The chemical structures of acceptors are shown in **Figure 4-1.** Materials for electron transport used in this chapter: (a) small molecule (PCBM), (b) dimer (di-PDI), (c) conjugated acceptor polymer P(PDI-2T) Zinc acetate dihydrate (Aldrich, 99.99%), ethanolamine (Aldrich, ≥99.5%), and 2-methoxy ethanol (Nacalai Tesque, 99%) were used for the preparation of the zinc oxide (ZnO) precursor. The ZnO precursor was prepared by dissolving 50 mg of zinc acetate dehydrate and 14 μL of ethanolamine in 500 μL of 2-methoxy ethanol under vigorous stirring for 12 h in the air; they were then used for spin-coating.[27]

4.2.2. Electron-injecting electrode

An indium–tin-oxide (ITO) substrate (flat ITO, GEOMATEC, Japan) was sequentially washed for 10 min by ultrasonication with toluene, acetone, and ethanol, and then dried with an N_2 flow. The cleaned substrate was further treated with a UV–O$_3$ cleaner (SSP16-110, SEN LIGHT Corp., Japan) for 30 min. ZnO electrode was prepared by spin-coating the ZnO precursor solution on the ITO and annealing at 200 °C for one hour in the air.[27]

The preparation method for the thin-layer of PEIE was optimized by spin-coating, dip-rinsing, and dry-spinning method. First, PEIE was spin-coat on the ITO/ZnO substrate at a spin rate of 5000 rpm for 120 s. The film then rinses into 2-methoxy ethanol by dipping for 5 min to remove excess PEIE on the ZnO surface. The wet layer then dried by spinning again at 5000 rpm for 3 minutes, followed by vacuuming in a desiccator for 2 hours to remove 2-methoxy ethanol altogether. The PEIE-modified electrode was used for both C-AFM and Macroscopic *J-V* characteristic measurement.

4.2.3. Acceptor films ~~preparation~~

Acceptor films were prepared by spin-coating from DCB for (PCBM) and CB for (di-PDI and P(PDI-2T)) solutions onto the PEIE electrode in the N_2–filled glovebox followed by drying in a desiccator for 2 hours. The film thickness was ±44 nm (PCBM), ±40 nm (di-PDI), and ±35 nm (P(PDI-2T)), respectively.

4.2.4. Characterizations

C-AFM Measurement: C-AFM measurements were performed using the microscope (SPM-9700, Shimadzu, Japan) in contact mode with an Au-coated silicon probe (PPP-CONTAu, NANO*SENSORS*[TM], Switzerland; tip radius < 50 nm; spring constant = 0.2–0.25 N m^{-1}). A sample bias was applied to the PEIE electrode, and the probe was grounded (**Figure 4-3a**). The surface topography and corresponding current images were simultaneously obtained by C-AFM measurements operating at a constant sample bias of –5.0 V. All C-AFM measurements were performed under an N_2 atmosphere using a controlled-environment chamber (CH-III, Shimadzu, Japan).

J-V characterization: Electron-only devices were fabricated by the following procedure. Acceptor films were spin-coated onto each PEIE electrode. Thicknesses of the acceptor films were adjusted within a range of 70–110 nm. Ca (10 nm) and Ag (100 nm) were then vacuum-deposited sequentially at 3×10^{-4} Pa on top of the acceptor film (ZnO/PEIE|acceptor film|Ca/Ag). A surface area of the Ca/Ag top electrode was 0.04 cm^2. The dark *J–V* characteristics of the acceptor films were measured with a condition where the electron was injected from a Ca/Ag top electrode in an N$_2$ atmosphere at room temperature, using a direct-current voltage and a current source/monitor (R6243, Advantest). Electron mobilities (μ_e) were calculated from the *J–V* characteristics using the space-charge-limited current (SCLC) method using the Mott–Gurney equation for current density J_{SCLC}, expressed as $J_{SCLC} = \frac{9}{8} \varepsilon_0 \varepsilon_r \mu_e \frac{V^2}{L^3}$, Where ε_0 is the vacuum permittivity, ε_r is the dielectric constant of the film ($\varepsilon_r = 3$ was assumed), and L is the thickness of the active layer.[13]

GIWAXS measurements: GIWAXS measurements were carried out at room temperature for the acceptor films, PCBM (thickness of 44 nm), di-PDI (40 nm), and P(PDI-2T) (35 nm), using the Spring-8 BL40B2 beamline (Hyogo, Japan). The X-ray wavelength was set to 0.1 nm, and the X-ray beam was aimed at the sample with an incident angle of 0.14° with respect to the sample surface. The X-ray exposure time was 50 s for all samples. The scattering signal was detected using a hybrid photon counting X-ray detector (Pilatus3 S 2M, Dectris Ltd., Switzerland) with a 1475×1679-pixels, which was positioned 342.8 mm away from the sample. The scattering vector magnitude q ($= (4\pi/\lambda) \sin\theta$, where 2θ is the scattering angle) was calibrated using silver behenate ($q = 2\pi/5.838$ nm^{-1})).

4.3.   Result and discussion

4.3.1.   Development of electron-injecting electrode

Local I-V characteristics of electrodes
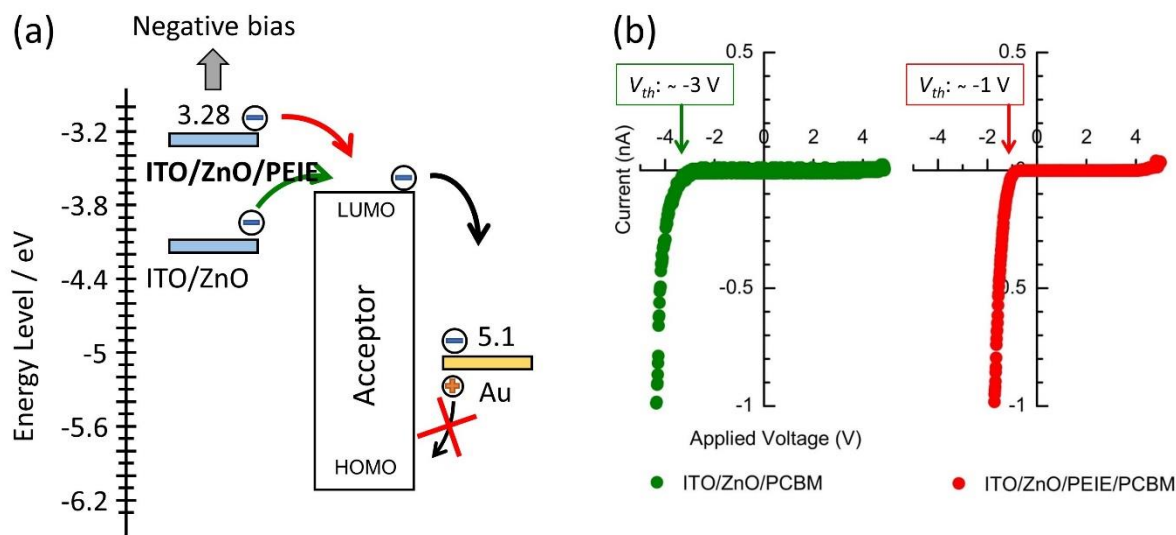
Figure 4-2. The energy level and Local I-V Characteristics of Electrodes. Each energy level is taken from the literature: 4.26 eV for ITO/ZnO,[28] 3.28 eV for ITO/ZnO/PEIE,[28] 5.1 eV for Au;[28] HOMO energy of 6.1 eV and LUMO energy of 3.7 eV for PCBM.[29]

Figure 4-2 shows a direct comparison between typical and modified electrodes. Firstly, the low-work function electrode was developed by coating a thin-layer of PEIE on the ITO/ZnO electrode. The effect of PEIE was characterized by measuring the *I-V* characteristic of PCBM film on the ITO/ZnO and ITO/ZnO/PEIE electrodes. The applied negative bias voltage, where the current started to flow, was defined as a threshold voltage (V_{th}). As shown in **Figure 4-2b**, the V_{th} of the PEIE-modified electrode (red arrow) is lower than the V_{th} of ITO/ZnO electrode (green arrow).

The lower V_{th} for the PEIE-modified electrode is due to the shallower work function. It is reported that the work function of the ITO/ZnO electrode is reduced by the existence of the PEIE thin- layer due to the robust interface molecular dipoles that induce a vacuum-level

shift.[28,30,31] This result demonstrates that the ITO/ZnO/PEIE electrode is successfully applied as a cathode, which can inject an electron into acceptors.

4.3.2. Current images of conjugated polymer

Device and energy level architecture
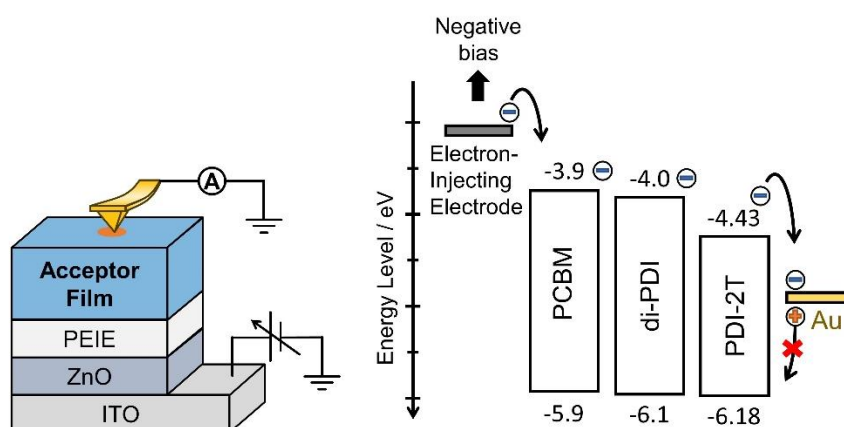
Figure 4-3. Device and energy level architecture. Each HOMO and LUMO energy level of di-PDI and P(PDI-2T) are taken from the literature.[8,32]

Figure 4-3 shows device and energy level architecture. The acceptor films of the small molecule (PCBM) and perylene diimide dimer (di-PDI) were prepared to compare with the acceptor polymer (P(PDI-2T)). The acceptor films have a deep LUMO level suitable for electron injection and transport, while the hole injection and transport are prohibited due to the injection barrier between the HOMO level of acceptors and the Au electrode work function. Au coated probe of C-AFM collected electrons at the surface of the acceptor film when the negative voltage is applied to the substrate (**Figure 4-3**).

Topography and current images from C-AFM characterization
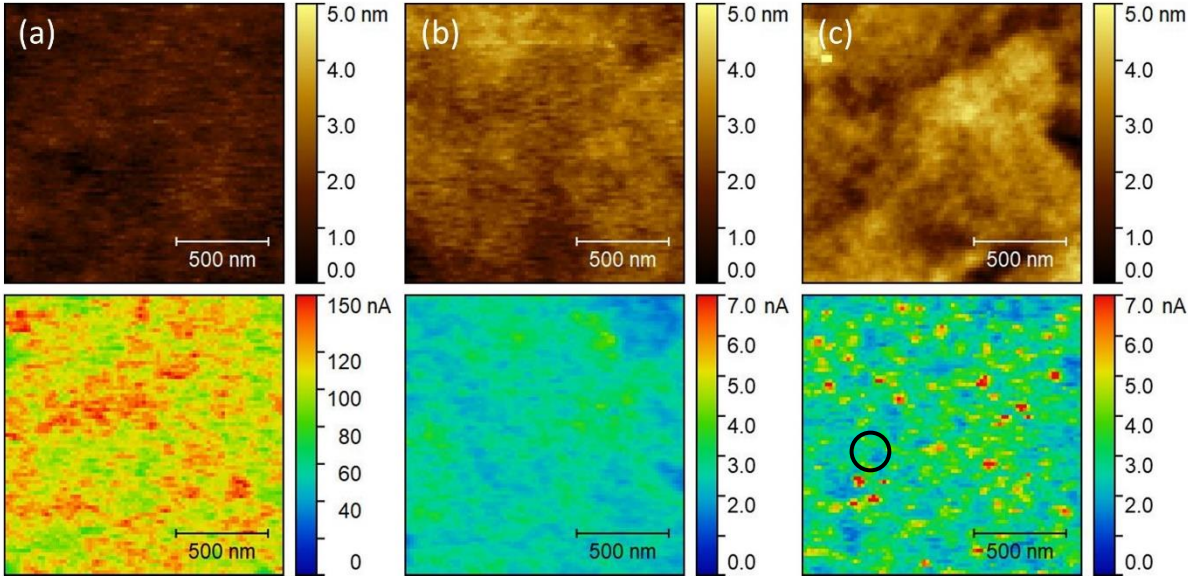
Figure 4-4. Topographic and current images of(PCBM, di-PDI, and P(PDI-2T)

Topographic and current images of PCBM, di-PDI, and P(PDI-2T) are shown in **Figure 4-4**.

The current images were obtained under a voltage of -5 V applied to the ZnO/PEIE electrode.

Local I-V characteristics
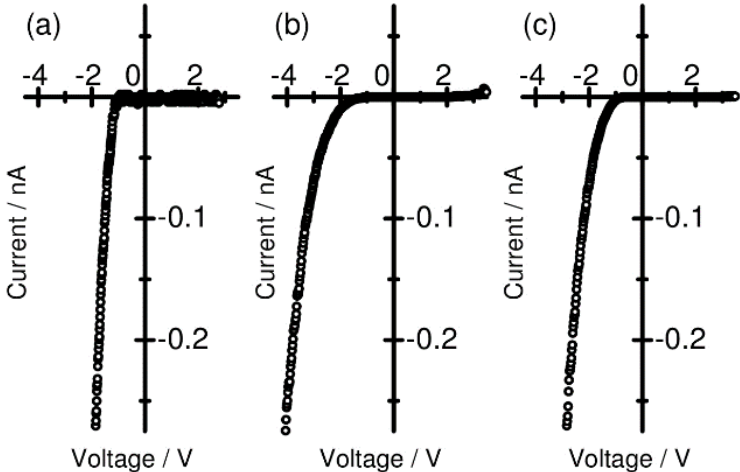
Figure 4-5. Local I-V Characteristics of: (a) PCBM, (b) di-PDI, and (c) P(PDI-2T)

Local I-V characteristics were measured for each acceptor by applying a negative and positive applied voltage in an N_2 atmosphere (**Figure 4-5**). The result showed that the current only detected when the negative voltage was applied to the ZnO/PEIE electrodes. The low work-function of bottom electrodes enabling electron injection to the LUMO level of acceptor materials. Under negative applied voltage, the rectifying *J-V* characteristics in **Figure 4-5** confirmed that the current measured by C-AFM is the electron current.

Correlation between current and surface topography
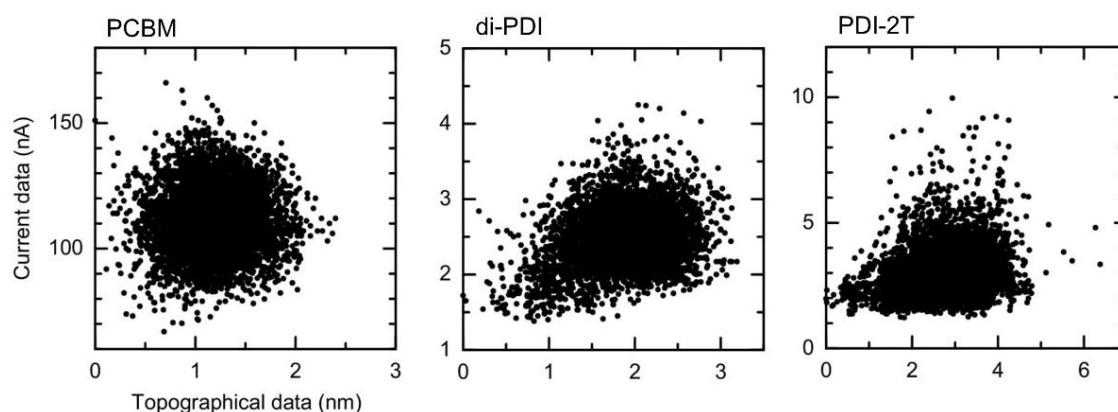
Figure 4-6. Correlation between current and topographic images

Figure 4-6 shows a correlation between surface topographic and current image shown in **Figure 4-4**. The current and topographic values of each point were plotted in the y- and x-axis, simultaneously. The figure showed there is no correlation between the current and the surface feature in the film. Therefore, it is indicated that local the current value is not affected by the surface structure at each point. The difference in the local currency instead reflects the difference in the conductive properties of the microstructure in the film.

Charge Transport in Micro- and Macroscopic Scale
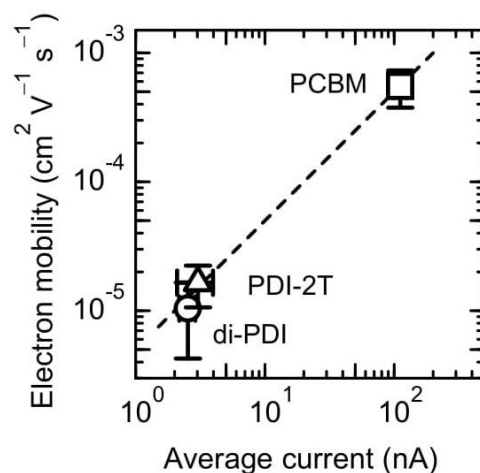
Figure 4-7. Correlation between average current from C-AFM current images and electron mobility extracted from macroscopic *J-V* characteristic: di-PDI (circle), P(PDI-2T) (triangle), and PCBM (square).

The average current measured by C-AFM current image and macroscopic *J-V* characteristics were plotted in **Figure 4-7.** The linear correlation between microscopic and macroscopic charge transport confirms that the C-AFM current images successfully depict the difference in electron-transporting abilities between acceptor materials.

4.3.3. Characteristics of electron transport in acceptor films
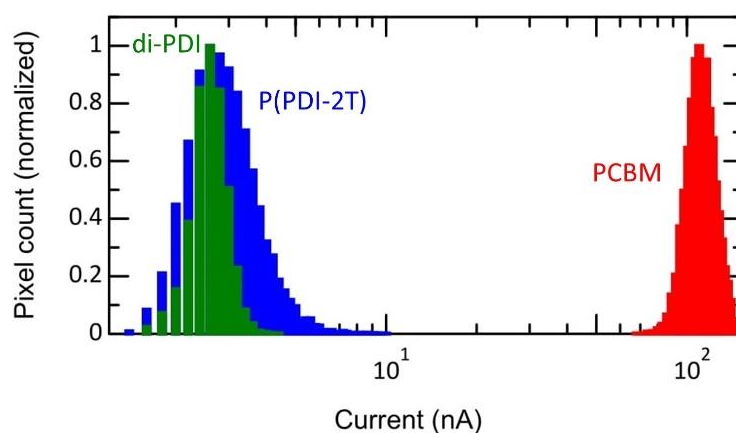
Figure 4-8. Histogram of the current images in **Figure 4-5**: PCBM in red, di-PDI in green, P(PDI-2T) in blue

Table 4-1 shows the histogram, minimum current (I_{min}), current at peak (I_{mode}), average current (I_{av}), maximum current (I_{max}), and relative standard deviation (RSD) of each current image (Figure 4-4). The current images of PCBM and di-PDI are relatively homogeneous, as can be judged from their low RSD values. On the other hand, the histogram of P(PDI-2T) is relatively broad, and the value of RSD is the highest among the three.

Table 4-1. Parameters from the current images

	Small-molecule PCBM	Dimer di-PDI	Polymer P(PDI-2T)
Minimum current I_{min} (nm)	-67.6	-1.4	-1.3
Current at the center of histogram I_{mode} (nm)	-108.5	-2.6	-2.7
Average current I_{av} (nm)	-111.5	-2.5	-3
Maximum current I_{max} (nm)	-166.7	-4.3	-10
Relative Standar Deviation (RSD)	11%	14%	31%

4.3.4. GIWAX measurements

GIWAXS was used to investigate the molecular packing and aggregation properties of the acceptor films. The 2D GIWAXS patterns and the in-plane and out-of-plane diffraction profiles are shown in **Figure 4-9**, and the results are summarized in **Table A4-1**. For each 2-D GIWAXS image of the films, out-of-plane and in-plane profiles were constructed by integrating the intensity at each q value over an azimuth range of 70–110° and 2–22°, respectively. The spacings d of molecular packing and stacking were calculated from the center positions q of the peaks according to the relationship $d = 2\pi/q$. The coherence length L_c was estimated from the Scherrer equation (**Equation 4.1**) using the full width at half maximum (FWHM) value determined from the fit and assuming the shape factor K to be 0.9.[33,34]

$$L_c = \frac{2\pi K}{\text{FWHM}}$$ **Equation 4.1**

For the PCBM film (**Figure 4-9 a and d**), three isotropic diffraction rings are observed at q_{xy} = 7.3 nm^{-1}, 13.9 nm^{-1}, 20.4 nm^{-1}, representing the aggregate behavior of the PCBM with randomly oriented on the substrate.[35] For the di-PDI film (**Figure 4-9 b and e**), two isotropic diffraction rings are observed at q_{xy} = 3.3 nm^{-1}, 14.1 nm^{-1}. The weak and broad diffraction patterns represent di-PDI were weakly interacted with each other and randomly oriented on the substrate. The diffraction peak at q_{xy} = 3.3 nm^{-1} (d = 1.9 nm, L_c = 3.3 nm) corresponds to alkyl chain stacking and a peak near q_{xy} = 14.1 nm^{-1} (d = 0.45 nm, L_c = 0.69 nm) corresponds to the π-π stacking interaction.[32] Typically, the π-π stacking distance of the PDI molecule has been reported q ~ 18 nm^{-1} (d ~ 0.35 nm)[32]. The lower q value of 14.1 nm^{-1} for the di-PDI indicates the π-π stacking was relative loose due to the dimer structure consisting of the twisted molecular configuration of PDIs. The stereochemical hindrance would hamper the di-PDI to self-organize in the solid-state. The 2D GIWAXS pattern for the P(PDI-2T) film is shown in **Figure 4-9c**. The diffraction profiles contain a lamellar (100) reflection peak at q_{xy} = 2.8 nm^{-1} (d = 2.24 nm, L_c = 3.57 nm) and a peak near q_z = 14.4 nm^{-1} (d = 0.44 nm, L_c = 0.95 nm), which corresponds to the π-π stacking interaction. They also contain (001) diffractions at q_{xy} = 5.1 nm^{-1} (d = 1.23 nm, L_c = 2.54 nm), which is related to diffractions along the polymer backbone direction.[12] Unlike the PCBM and di-PDI, the relatively strong (010) diffraction intensity distributed along the out-of-plane direction implies that the aggregation of the P(PDI-2T) was a weakly face-on orientation on the substrate.
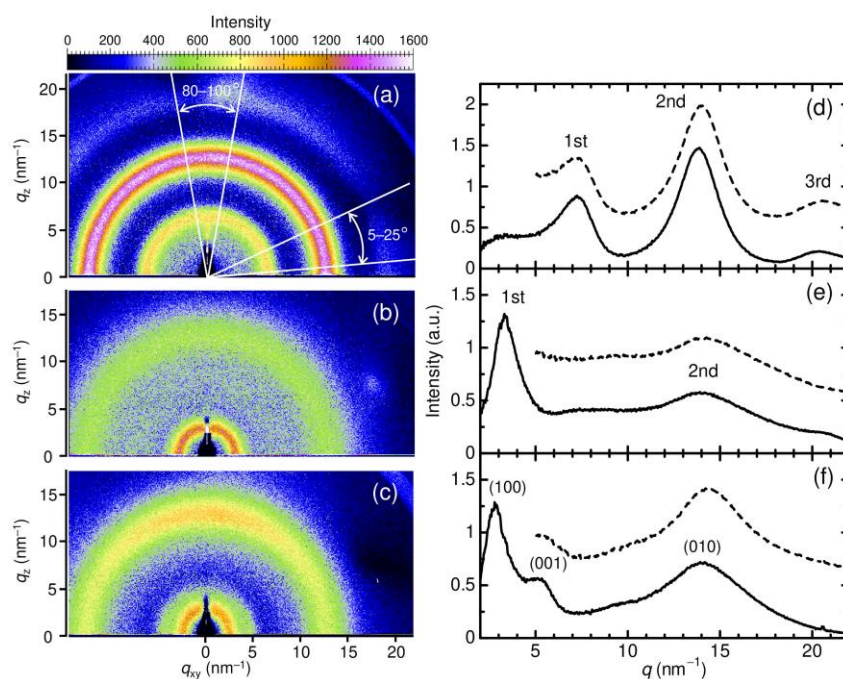
Figure 4-9. 2D GIWAXS patterns of (a) PCBM, (b) di-PDI, and (c) P(PDI-2T) films. In-plane (solid lines) and out-of-plane (dashed lines) 2D GIWAXS profiles of the (d) PCBM, (e) di-PDI, and (f) P(PDI-2T) films.

4.4. Discussion

To discuss the local conductive properties of the acceptors, the mode (I_{mode}) and mean (I_{av}) values of the current, and the values of relative standard deviation (I_{RSD}) were extracted from the current distribution histograms of the images. As shown in the histogram **Figure 4-8**, PCBM showed a much larger current than the PDI-based acceptors, and the spatial distribution of the current was relatively uniform since the RSD value is the lowest. For di-PDI, the spatial distribution of the current was as uniform as PCBM because of the nearly same value of RSD between them. For the P(PDI-2T), the distribution was much broader compared with both PCBM and di-PDI, since the RSD are the highest. The average current of PCBM is the highest, while the average current of P(PDI-2T) is a bit higher than di-PDI.

In P(PDI-2T), relatively high current regions appeared as indicated by circles in **Figure 4-4**. These conducting regions were characteristic in P(PDI-2T) and not observed in the image of

PCBM and di-PDI, which broadened the current histogram in a higher current direction and gave larger RSD value. Here, we define the region that yields current flow larger than -4.3 nA, which is the maximum current in the di-PDI film, as a "highly conducting region." **Figure 4-10c** reveals the spatial distribution of the highly conducting region formed in the P(PDI-2T) film. The typical size of the highly conducting regions was ~100 nm, and they occupied 4.4% of the scan area, and the current passing through the regions accounted for 8.5% of the total current flow through the scan area.

It is noted again that the current distributions in the images were not associated with the topographical features that appeared on the film surface. Therefore, the spatial variations in the local electron conductivity could relate to the microstructure in films. It has been reported that a thin-film of PCBM spin-coated from chlorobenzene consists of densely and homogeneously distributed PCBM nano-aggregates.[35] The good electronic connectivity between aggregates and isotropic charge transport owing to the spherical shape of the fullerene π-system provides efficient and spatially homogeneous electron transport throughout the film, consistent with the large I_{av} and small RSD values obtained. As to the di-PDI, the twisted dimeric structure weakens the intermolecular aggregation by π-π stacking of planar PDI units, resulting in the loosely packed and rough structure of di-PDI aggregates in the solid-state. Although the twisted conformation gives relatively homogeneous microstructure in the film, the lack of dense and ordered packing of the di-PDI molecules leads to lower electron transport. These behaviors produce charge transport properties of the di-PDI film characterized by I_{av} much smaller than PCBM and RSD similar to PCBM. It has been suggested that conjugated polymer chains form inter- and intra-chain aggregates in films, which play an essential role for efficient charge transport in conjugated polymer films.[36–39] The relatively high conductive domains shown in **Figure 4-10c** are expected to be the aggregate-rich regions, in which preferred pathways for charge transport are provided throughout the film.[21,23]

Finally, we focus on the charge transport of the relatively high conductive regions in the P(PDI-2T) film. The average current per pixel within the regions was still 37-times lower than the I_{av} in PCBM film, implying that charge transport in P(PDI-2T) film is intrinsically limited. To quantify the microstructure of P(PDI-2T) aggregate, the number of PDI-bithiophene repeat units in an ordered part of the chain backbone $N_{(001)}$, the number of stacks in the lamellar direction $N_{(100)}$, and π-π stacking direction $N_{(010)}$ were estimated respectively via $N = L_c/d$: the aggregate consists of one or two repeat units in the chain backbone and two chains in both the lamellar and π-π stacking directions on average (**Figure 4-10a**). The measured size of P(PDI-2T) aggregate is much smaller compared with that of a few exquisite polymer acceptors such as P(NDI2OD-T2) exhibiting μ_e of $\sim 1 \times 10^{-3}$ cm^2 V^{-1} s^{-1} similar to PCBM. Furthermore, the π-π stacking distance of 0.44 nm measured for P(PDI-2T) is longer than that reported for the high mobility polymer acceptors.[40] The limited charge transport in P(PDI-2T) film is thus ascribed to the weak inter- and intrachain aggregations of P(PDI-2T), which most probably originates in the steric hindrance the bulky, dovetailed alkyl chains at the imide nitrogen positions.

In summary, the electron current images were obtained by C-AFM, enabling a direct view of electron conductivity and its spatial distribution in nanoscale. The C-AFM current images bring it to light that local structural order and molecular packing in the film play a key role in overall electron transport in the acceptor films. These advantages underline the capability of C-AFM to electrically resolve nanostructures of semiconducting polymer films, contributing to further understanding of the mechanisms for the excellent electron transport and the creation of materials electrical functions.
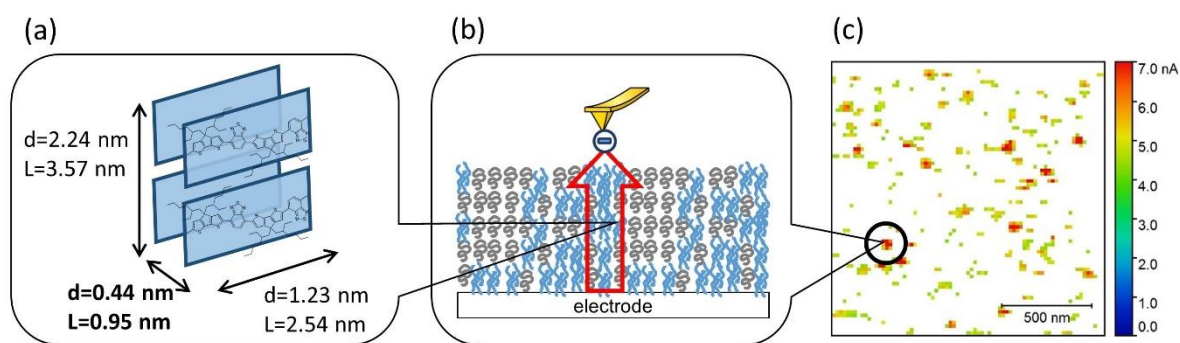
Figure 4-10. Structure-charge transport model of P(PDI-2T) polymer. (a) Aggregate structure expected from GIWAX result (**Table A4-1**); (b) Charge transport morphology expected from C-AFM current images; (c) Distribution maps of highly conducting regions in the P(PDI-2T) film based on **Figure 4-4**.

4.5. Conclusion

The local electrical conductivity was studied for thin-films of PCBM, and P(PDI-2T) acceptors by C-AFM, using a PEIE-coated ZnO substrate as an electron-injecting electrode. Densely and homogeneously distributed PCBM nano-aggregates leads to the excellent and uniform electron transport throughout the film. The introduction of the twisted dimeric structure of the di-PDI resulted in the uniform morphology for electron transport, but the weakened intermolecular stacking offsets the electron-transport ability in the PDI. On the other hand, polymer acceptor P(PDI-2T) formed spatially inhomogeneous electron-conducting morphology, which is composed of relatively high conductive domains with a typical size of 100 nm due to aggregation among conjugated polymer chains. The current distribution images successfully depicted the role of the local ordering and aggregation behavior of the acceptor molecules in the electrically conductive properties of the films on a macroscale.

4.6. Reference

(1)   Yang, J.; Zhao, Z.; Wang, S.; Guo, Y.; Liu, Y. Insight into High-Performance Conjugated Polymers for Organic Field-Effect Transistors. *Chem* **2018**, *4* (12), 2748–2785. https://doi.org/10.1016/j.chempr.2018.08.005.

(2)   Kim, M.; Ryu, S. U.; Park, S. A.; Choi, K.; Kim, T.; Chung, D.; Park, T. Donor–Acceptor-Conjugated Polymer for High-Performance Organic Field-Effect Transistors: A Progress Report. *Adv. Funct. Mater.* **2020**, *30* (20), 1–25. https://doi.org/10.1002/adfm.201904545.

(3)   Paterson, A. F.; Singh, S.; Fallon, K. J.; Hodsden, T.; Han, Y.; Schroeder, B. C.; Bronstein, H.; Heeney, M.; McCulloch, I.; Anthopoulos, T. D. Recent Progress in High-Mobility Organic Transistors: A Reality Check. *Adv. Mater.* **2018**, *30* (36), 1–33. https://doi.org/10.1002/adma.201801079.

(4)   Wang, G.; Melkonyan, F. S.; Facchetti, A.; Marks, T. J. All-Polymer Solar Cells: Recent Progress, Challenges, and Prospects. *Angew. Chemie - Int. Ed.* **2019**, *58* (13), 4129–4142. https://doi.org/10.1002/anie.201808976.

(5)   Lee, C.; Lee, S.; Kim, G. U.; Lee, W.; Kim, B. J. Recent Advances, Design Guidelines, and Prospects of All-Polymer Solar Cells. *Chem. Rev.* **2019**, *119* (13), 8028–8086. https://doi.org/10.1021/acs.chemrev.9b00044.

(6)   Benten, H.; Mori, D.; Ohkita, H.; Ito, S. Recent Research Progress of Polymer Donor/Polymer Acceptor Blend Solar Cells. *J. Mater. Chem. A* **2016**, *4* (15), 5340–5365. https://doi.org/10.1039/c5ta10759h.

(7)   Zhan, C.; Yao, J. More than Conformational "Twisting" or "Coplanarity": Molecular Strategies for Designing High-Efficiency Nonfullerene Organic Solar Cells. *Chem. Mater.* **2016**, *28* (7), 1948–1964. https://doi.org/10.1021/acs.chemmater.5b04339.

(8)   Kozma, E.; Kotowski, D.; Bertini, F.; Luzzati, S.; Catellani, M. Synthesis of Donor-

Acceptor Poly(Perylene Diimide-Altoligothiophene) Copolymers as n-Type Materials for Polymeric Solar Cells. *Polymer (Guildf).* **2010**, *51* (11), 2264–2270. https://doi.org/10.1016/j.polymer.2010.03.040.

(9)   Guo, Y.; Li, Y.; Awartani, O.; Zhao, J.; Han, H.; Ade, H.; Zhao, D.; Yan, H. A Vinylene-Bridged Perylenediimide-Based Polymeric Acceptor Enabling Efficient All-Polymer Solar Cells Processed under Ambient Conditions. *Adv. Mater.* **2016**, *28* (38), 8483–8489. https://doi.org/10.1002/adma.201602387.

(10)   Xiong, W.; Meng, X.; Liu, T.; Cai, Y.; Xue, X.; Li, Z.; Sun, X.; Huo, L.; Ma, W.; Sun, Y. Rational Design of Perylenediimide-Based Polymer Acceptor for Efficient All-Polymer Solar Cells. *Org. Electron.* **2017**, *50*, 376–383. https://doi.org/10.1016/j.orgel.2017.08.005.

(11)   Samanta, S. K.; Song, I.; Yoo, J. H.; Oh, J. H. Organic N-Channel Transistors Based on [1]Benzothieno[3,2- b]Benzothiophene-Rylene Diimide Donor-Acceptor Conjugated Polymers. *ACS Appl. Mater. Interfaces* **2018**, *10* (38), 32444–32453. https://doi.org/10.1021/acsami.8b10831.

(12)   Suranagi, S. R.; Singh, R.; Kim, J. H.; Kim, M.; Ade, H.; Cho, K. Molecular Engineering of Perylene-Diimide-Based Polymer Acceptors Containing Heteroacene Units for All-Polymer Solar Cells. *Org. Electron.* **2018**, *58* (November 2017), 222–230. https://doi.org/10.1016/j.orgel.2018.02.015.

(13)   Shen, Y.; Hosseini, A. R.; Wong, M. H.; Malliaras, G. G. How to Make Ohmic Contacts to Organic Semiconductors. *ChemPhysChem* **2004**, *5* (1), 16–25. https://doi.org/10.1002/cphc.200300942.

(14)   Alexeev, A.; Loos, J.; Koetse, M. M. Nanoscale Electrical Characterization of Semiconducting Polymer Blends by Conductive Atomic Force Microscopy (C-AFM). *Ultramicroscopy* **2006**, *106* (3), 191–199.

https://doi.org/10.1016/j.ultramic.2005.07.003.

(15) Groves, C.; Reid, O. G.; Ginger, D. S. Heterogeneity in Polymer Solar Cells: Local Morphology and Performance in Organic Photovoltaics Studied with Scanning Probe Microscopy. *Acc. Chem. Res.* **2010**, *43* (5), 612–620. https://doi.org/10.1021/ar900231q.

(16) Mativetsky, J. M.; Loo, Y. L.; Samorì, P. Elucidating the Nanoscale Origins of Organic Electronic Function by Conductive Atomic Force Microscopy. *J. Mater. Chem. C* **2014**, *2* (17), 3118–3128. https://doi.org/10.1039/c3tc32050b.

(17) Moerman, D.; Sebaihi, N.; Kaviyil, S. E.; Leclère, P.; Lazzaroni, R.; Douhéret, O. Towards a Unified Description of the Charge Transport Mechanisms in Conductive Atomic Force Microscopy Studies of Semiconducting Polymers. *Nanoscale* **2014**, *6* (18), 10596–10603. https://doi.org/10.1039/c4nr02577f.

(18) Lin, H. N.; Lin, H. L.; Wang, S. S.; Yu, L. S.; Perng, G. Y.; Chen, S. A.; Chen, S. H. Nanoscale Charge Transport in an Electroluminescent Polymer Investigated by Conducting Atomic Force Microscopy. *Appl. Phys. Lett.* **2002**, *81* (14), 2572–2574. https://doi.org/10.1063/1.1509464.

(19) Douhéret, O.; Swinnen, A.; Breselge, M.; Van Severen, I.; Lutsen, L.; Vanderzande, D.; Manca, J. High Resolution Electrical Characterisation of Organic Photovoltaic Blends. *Microelectron. Eng.* **2007**, *84* (3), 431–436. https://doi.org/10.1016/j.mee.2006.10.056.

(20) Dante, M.; Peet, J.; Nguyen, T. Q. Nanoscale Charge Transport and Internal Structure of Bulk Heterojunction Conjugated Polymer/Fullerene Solar Cells by Scanning Probe Microscopy. *J. Phys. Chem. C* **2008**, *112* (18), 7241–7249. https://doi.org/10.1021/jp712086q.

(21) Chen, M. C.; Hung, W. C.; Su, A. C.; Chen, S. H.; Chen, S. A. Nanoscale Ordered Structure Distribution in Thin Solid Film of Conjugated Polymers: Its Significance in Charge Transport across the Film and in Performance of Electroluminescent Device. *J.*

Phys. Chem. B **2009**, *113* (32), 11124–11133. https://doi.org/10.1021/jp901644m.

(22)   Osaka, M.; Benten, H.; Lee, L. T.; Ohkita, H.; Ito, S. Development of Highly Conductive

Nanodomains in Poly(3-Hexylthiophene) Films Studied by Conductive Atomic Force

Microscopy.   *Polymer   (Guildf).   **2013**,   *54*   (14),   3443–3447.

https://doi.org/10.1016/j.polymer.2013.04.061.

(23)   Osaka, M.; Benten, H.; Ohkita, H.; Ito, S.; Ogawa, H.; Kanaya, T. Nanostructures for

Efficient Hole Transport in Poly(3-Hexylthiophene) Film: A Study by Conductive

Atomic Force Microscopy. *J. Phys. Chem. C* **2015**, *119* (43), 24307–24314.

https://doi.org/10.1021/acs.jpcc.5b08237.

(24)   Kondo, Y.; Osaka, M.; Benten, H.; Ohkita, H.; Ito, S. Electron Transport Nanostructures

of Conjugated Polymer Films Visualized by Conductive Atomic Force Microscopy. *ACS*

Macro Lett. **2015**, *4* (9), 879–885. https://doi.org/10.1021/acsmacrolett.5b00352.

(25)   Chen, Z.; Zheng, Y.; Yan, H.; Facchetti, A. Naphthalenedicarboximide- vs

Perylenedicarboximide-Based Copolymers . Synthesis and Semiconducting Properties

in   Bottom-Gate   N-Channel   Organic   Transistors.   **2009**,   8–9.

https://doi.org/10.1021/ja805407g.

(26)   Milia´n-Medina, B.; Wykes, M.; Chen, Z.; Facchetti, A.; Gierschner, J. Materials

Chemistry   C.   *J.   Mater.   Chem.   C*   **2016**,   *4*,   9405–9410.

https://doi.org/10.1039/c6tc03056d.

(27)   Sun, Y.; Seo, J. H.; Takacs, C. J.; Seifter, J.; Heeger, A. J. Inverted Polymer Solar Cells

Integrated with a Low-Temperature-Annealed Sol-Gel-Derived ZnO Film as an Electron

Transport   Layer.   *Adv.   Mater.*   **2011**,   *23*   (14),   1679–1683.

https://doi.org/10.1002/adma.201004301.

(28)   Zhou, Y.; Fuentes-hernandez, C.; Shim, J.; Meyer, J.; Giordano, A. J.; Li, H.; Winget,

P.; Papadopoulos, T.; Cheun, H.; Kim, J.; et al. For Organic Electronics. **2012**, *873*

(April), 327–332. https://doi.org/10.1126/science.1218829.

(29) Mihailetchi, V. D.; Van Duren, J. K. J.; Blom, P. W. M.; Hummelen, J. C.; Janssen, R. A. J.; Kroon, J. M.; Rispens, M. T.; Verhees, W. J. H.; Wienk, M. M. Electron Transport in a Methanofullerene. *Adv. Funct. Mater.* **2003**, *13* (1), 43–46. https://doi.org/10.1002/adfm.200390004.

(30) Stolz, S.; Scherer, M.; Mankel, E.; Lovrinčić, R.; Schinke, J.; Kowalsky, W.; Jaegermann, W.; Lemmer, U.; Mechau, N.; Hernandez-Sosa, G. Investigation of Solution-Processed Ultrathin Electron Injection Layers for Organic Light-Emitting Diodes. *ACS Appl. Mater. Interfaces* **2014**, *6* (9), 6616–6622. https://doi.org/10.1021/am500287y.

(31) Courtright, B. A. E.; Jenekhe, S. A. Polyethylenimine Interfacial Layers in Inverted Organic Photovoltaic Devices: Effects of Ethoxylation and Molecular Weight on Efficiency and Temporal Stability. *ACS Appl. Mater. Interfaces* **2015**, *7* (47), 26167–26175. https://doi.org/10.1021/acsami.5b08147.

(32) Singh, R.; Lee, J.; Kim, M.; Keivanidis, P. E.; Cho, K. Control of the Molecular Geometry and Nanoscale Morphology in Perylene Diimide Based Bulk Heterojunctions Enables an Efficient Non-Fullerene Organic Solar Cell. *J. Mater. Chem. A* **2017**, *5* (1), 210–220. https://doi.org/10.1039/C6TA08870H.

(33) Smilgies, D. M. Scherrer Grain-Size Analysis Adapted to Grazing-Incidence Scattering with Area Detectors. *J. Appl. Crystallogr.* **2009**, *42* (6), 1030–1034. https://doi.org/10.1107/S0021889809040126.

(34) Rivnay, J.; Mannsfeld, S. C. B.; Miller, C. E.; Salleo, A.; Toney, M. F. Quantitative Determination of Organic Semiconductor Microstructure from the Molecular to Device Scale. *Chem. Rev.* **2012**, *112* (10), 5488–5519. https://doi.org/10.1021/cr3001109.

(35) Kim, J. Y.; Frisbie, C. D. Correlation of Phase Behavior and Charge Transport in Conjugated Polymer/Fullerene Blends. *J. Phys. Chem. C* **2008**, *112* (45), 17726–17736.

https://doi.org/10.1021/jp8061493.

(36) Noriega, R.; Rivnay, J.; Vandewal, K.; Koch, F. P. V.; Stingelin, N.; Smith, P.; Toney, M. F.; Salleo, A. A General Relationship between Disorder, Aggregation and Charge Transport in Conjugated Polymers. *Nat. Mater.* **2013**, *12* (11), 1038–1044. https://doi.org/10.1038/nmat3722.

(37) Wang, S.; Fabiano, S.; Himmelberger, S.; Puzinas, S.; Crispin, X.; Salleo, A.; Berggren, M. Experimental Evidence That Short-Range Intermolecular Aggregation Is Sufficient for Efficient Charge Transport in Conjugated Polymers. *Proc. Natl. Acad. Sci. U. S. A.* **2015**, *112* (34), 10599–10604. https://doi.org/10.1073/pnas.1501381112.

(38) Noriega, R. Efficient Charge Transport in Disordered Conjugated Polymer Microstructures. *Macromol. Rapid Commun.* **2018**, *39* (14), 1–9. https://doi.org/10.1002/marc.201800096.

(39) Gu, K.; Loo, Y. L. The Polymer Physics of Multiscale Charge Transport in Conjugated Systems. *J. Polym. Sci. Part B Polym. Phys.* **2019**, *57* (23), 1559–1571. https://doi.org/10.1002/polb.24873.

(40) Rivnay, J.; Toney, M. F.; Zheng, Y.; Kauvar, I. V.; Chen, Z.; Wagner, V.; Facchetti, A.; Salleo, A. Unconventional Face-on Texture and Exceptional in-Plane Order of a High Mobility n-Type Polymer. *Adv. Mater.* **2010**, *22* (39), 4359–4363. https://doi.org/10.1002/adma.201001202.

Chapter 5.

General Conclusion

5.1. General conclusion

In chapter 2, the effect of aggregates on the charge transport of the weakly-ordered conjugated polymer donor has been cleared. The fraction of aggregate has been estimated by analyzing UV-vis spectra of PSBTBT neat films prepared by various spin-coating conditions and the resulting I_1/I_2 ratio. The fraction of aggregate and I_1/I_2 ratio have a positive correlation, where an increase of ratio from 1.0 to 1.2 indicates an increase of the fraction of aggregate from 0.26 to 0.34. Hole mobility extracted from the *J-V* characteristic also shows a positive correlation with the fraction of aggregate. The increase of the fraction of aggregate leads to an increase of hole mobility from 1.89×10^{-5} to 1.53×10^{-4} cm^2/Vs. This positive correlation indicates that aggregates are an essential structure for charge transport, where a higher fraction of aggregates in the films leads to better charge transport.

In chapter 3, the change in the short-range ordered structure (aggregates) of the weakly-ordered conjugated polymer in the blend film has been investigated. The aggregates of PCPDTBT were increased in the fraction and the size gradually after blending with the P3M4HT matrix. The fraction of aggregates gradually increases from 0.51 in the neat film to 0.84 in the blend film. The size of aggregates in neat films is about ~ 4 repeat units and ~3 stacks in the backbone and lamellar stacking direction, respectively. In comparison, in the 10 wt.% of PSBTBT blend film, the aggregates are about ~7 repeat units and ~4 stacks in the backbone and lamellar stacking direction. The

C-AFM current images showed that the enhanced aggregation of weakly-ordered conjugated polymers (PSBTBT) result in the larger current flow through PSBTBT in the blend film than in the neat film.

In chapter 4, the microstructures and electron transport of the small molecule conjugated polymer acceptor thin film were discussed. Firstly, a shallow work-function electrode was fabricated by using PEIE. The local electrical conductivity was visualized for thin films of PCBM, di-PDI, and P(PDI-2T) by C-AFM, using a PEIE-coated ZnO substrate as an electron-injecting electrode. Densely and homogeneously distributed PCBM nano-aggregates leads to the excellent and uniform electron transport throughout the film. The twisted dimeric structure of the di-PDI resulted in the uniform morphology for electron transport, but the weakened intermolecular stacking offsets the electron-transport ability. On the other hand, polymer acceptor P(PDI-2T) formed spatially inhomogeneous electron-conducting morphology, which is composed of relatively high conductive domains with a typical size of 100 nm due to aggregation among conjugated polymer chains. The current distribution images successfully depicted the role of the local ordering and aggregation behavior of the acceptor molecules in the electrically conductive properties of the films on a macroscale.

5.2. The implication of the findings

Chapter 2 shows the importance of the fraction of aggregates for charge transport. The fraction of aggregates (or degree of aggregation[1]) refers to the density of aggregated structure inside the polymer film. In this viewpoint, UV-vis spectra have potential because it measures electrical interactions between segments of conjugated polymer chains and able to reveal the shape of polymer structure[2–4]. Chapter 2 realize the potential

of using UV-vis spectra to observe aggregates of the weakly-ordered conjugated polymer. The implication of a higher fraction of aggregates to the higher hole-transporting mobility also has been shown in chapter 2.

Chapter 3 clears the structural change of aggregates by blending with other polymers, short-range ordering of weakly-ordered conjugated polymer is enhanced. This short-range ordering enhancement would be significant for the design of efficient charge carrier transport in thin-film devices such as polymer/polymer blend solar cells that use low-bandgap donor-acceptor conjugated polymer with various blend ratios as a hole- and electron-transport materials.

Chapter 4 shows that ZnO/PEIE electrode can be widely and successfully applied for the C-AFM characterization of acceptor films. Also, the current images combined with GOWAX data suggest that not only aggregate formation but also closed stacking of planarized polymer chains is necessary to obtain better charge transport

Reference

(1)   Traiphol, R.; Potai, R.; Charoenthai, N.; Srikhirin, T.; Kerdcharoen, T.; Osotchan, T. Effects of Chain Conformation and Chain Length on Degree of Aggregation in Assembled Particles of Conjugated Polymer in Solvents-Nonsolvent: A Spectroscopic Study. *J. Polym. Sci. Part B Polym. Phys.* **2010**, *48* (8), 894–904. https://doi.org/10.1002/polb.21976.

(2)   Köhler, A.; Hoffmann, S. T.; Bässler, H. An Order-Disorder Transition in the Conjugated Polymer MEH-PPV. *J. Am. Chem. Soc.* **2012**, *134* (28), 11594–11601. https://doi.org/10.1021/ja302408a.

(3)   Panzer, F.; Bässler, H.; Köhler, A. Temperature Induced Order-Disorder Transition in Solutions of Conjugated Polymers Probed by Optical Spectroscopy. *J. Phys. Chem. Lett.* **2017**, *8* (1), 114–125. https://doi.org/10.1021/acs.jpclett.6b01641.

(4)   Scharsich, C.; Fischer, F. S. U.; Wilma, K.; Hildner, R.; Ludwigs, S.; Köhler, A. Revealing Structure Formation in PCPDTBT by Optical Spectroscopy. *J. Polym. Sci. Part B Polym. Phys.* **2015**, *53* (20), 1416–1430. https://doi.org/10.1002/polb.23780.

(5)   Wang, S.; Fabiano, S.; Himmelberger, S.; Puzinas, S.; Crispin, X.; Salleo, A. Experimental Evidence That Short-Range Intermolecular Aggregation Is Sufficient for Efficient Charge Transport in Conjugated Polymers. **2015**. https://doi.org/10.1073/pnas.1501381112.

(6)   Yu, K.; Park, B.; Kim, G.; Kim, C. H.; Park, S.; Kim, J.; Jung, S.; Jeong, S.; Kwon, S.; Kang, H.; et al. Optically Transparent Semiconducting Polymer Nanonetwork for Flexible and Transparent Electronics. *Proc. Natl. Acad. Sci. U. S. A.* **2016**, *113*

(50), 14261–14266. https://doi.org/10.1073/pnas.1606947113.

List of Publications

1. Scientific Papers

Chapter 2

"Microstructures and Hole Transport of Weakly-Ordered Conjugated Polymer Film"

Anjar Taufik Hidayat, Hiroaki Benten, Hirotaka Kojima, Min-Cherl Jung, Masakazu Nakamura

In preparation

Chapter 3

Anjar Taufik Hidayat, Hiroaki Benten, Noboru Ohta, Yunju Na, Azusa Muraoka, Hirotaka Kojima, Min-Cherl Jung, Masakazu Nakamura

"Enhancement of Short-Range Ordering of Low-Bandgap Donor-Acceptor Conjugated Polymer in Polymer/Polymer Blend Films"

Macromolecules DOI: 10.1021/acs.macromol.0c00623

Chapter 4

*"**Morphology and Electron Transport of Conjugated Polymer Thin Film Visualized by Conductive Atomic Force Microscopy"***

Anjar Taufik Hidayat, Hiroaki Benten, Noboru Ohta, Hirotaka Kojima, Min-Cherl Jung, Masakazu Nakamura

In preparation

2. Scientific Conferences

a. Domestic Conference

1) Oral Presentation

Anjar Taufik Hidayat*, Shoto Shigita, Hirotaka Kojima, Min-Cherl Jung, Hiroaki Benten, Masakazu Nakamura:

"Hole Transport in Conjugated Polymer Blends Studied by C-AFM"

The 15th Thin Film Materials & Devices Meeting (Rykoku University Avanti Kyoto Hall, Kyoto),

2018.11.9 ~ 10, (2018.11.10), 10a-O01.

Anjar Taufik Hidayat*, Hirotaka Kojima, Min-Cherl Jung, Hiroaki Benten, Masakazu Nakamura:

"Local Electron Transport Structures of Organic Semiconductor Thin Films Visualized by Conductive Atomic Force Microscopy"

The 64th Annual Kobe Polymer Research Symposium (Hyogo Prefecture Citizens' Hall, Kobe, Hyogo),

2018.7.13 (2020.7.13), C-6

Yuji Yamagata*, Anjar Taufik Hidayat, Hirotaka Kojima, Masakazu Nakamura, Hiroaki Benten:

"Nanoscale Photovoltaic Characteristics of Polymer/Polymer Blend Solar Cells Revealed by Photoconductive AFM"

The 66th Annual Kobe Polymer Research Symposium (Hyogo Prefecture Citizens' Hall, Kobe, Hyogo),

2020.7.10 (2020.7.10), D-13

Hiroaki Benten*, <u>Anjar Taufik Hidayat</u>, Noboru Ohta, Hirotaka Kojima, Min-Cherl Jung, Masakazu Nakamura:

"Improvement in Ordering of Conjugated Polymer Chains Observed in Polymer/Polymer Blend Films"

The 80th JSAP Autumn Meeting 2019 (Sapporo Campus, Hokkaido University, Sapporo), 2019.9.18 ~ 21, (2019.9.21), 21a-E101-6.

Hiroaki Benten*, Yuji Yamagata, <u>Anjar Taufik Hidayat</u>, Masakazu Nakamura:

"Photocurrent Generation in Donor/Acceptor Conjugated Polymer Blend Films Visualized by Photoconductive AFM"

2020 Online Annual Meeting on Photochemistry (Online Virtual Meeting)

2020.9.9 ~ 11, (2020.9.11), 3D02

Yuji Yamagata*, <u>Anjar Taufik Hidayat</u>, Masakazu Nakamura, Hiroaki Benten:

"Photocurrent Generation of All-Polymer Blend Solar Cells Studied by Photoconductive AFM"

The 81th JSAP Autumn Meeting 2020 (Online Virtual Meeting)

2020.9.8 ~ 11, (2020.9.10), 10p-Z11-10

 2) Poster Presentation

Hiroaki Benten*, <u>Anjar Taufik Hidayat</u>, Hirotaka Kojima, Min-Cherl Jung, Masakazu Nakamura:

"Local Electron Transport Characteristics of n-Type Conjugated Polymer Films Visualized by Conductive AFM"

The 69th SPSJ Annual Meeting (Fukuoka Convention Center, Fukuoka), 2020.5.27 ~ 29, (2020.5.28), 2Pd074.

Yunju Na*, <u>Anjar Taufik Hidayat</u>, Noboru Ohta, Hirotaka Kojima, Min-Cherl Jung, Masakazu Nakamura, Hiroaki Benten:

"Enhancement of Molecular-Level Ordering of π-Conjugated Polymer Chains in Polymer/Polymer Blend Films",

The 69th SPSJ Annual Meeting (Fukuoka Convention Center, Fukuoka),

2020.5.27 ~ 29, (2020.5.28), 2Pc073.

Yuji Yamagata*, <u>Anjar Taufik Hidayat</u>, Hirotaka Kojima, Min-Cherl Jung, Masakazu Nakamura, Hiroaki Benten:

"Nanoscale Photovoltaic Characteristics of Polymer Solar Cells Revealed by Photoconductive AFM",

The 69th SPSJ Annual Meeting (Fukuoka Convention Center, Fukuoka),

2020.5.27 ~ 29, (2020.5.28), 2Pc075.

b. International Conference

1) Poster Presentation

<u>Anjar Taufik Hidayat</u>*, Hiroaki Benten, Hirotaka Kojima, Min-Cherl Jung, Masakazu Nakamura:

"Enhanced Aggregation of Low-Bandgap Polymer in Polymer/Polymer Blend Films",

2019 MRS Fall Meeting (Boston, Massachusetts),

2019.12.1 ~ 6, (2019.12.5), EN12.15.29.

Acknowledgments

Finally, The author would like to thank his wife and parents, Imas Siti Aisyah, Suparni, and Agus Sugiyarto, sincerely, for their support, excellent assistance, and encouragement.

August 2020,

Anjar Taufik Hidayat

Appendix

A2. Appendix for Chapter 2

Spectral decomposition
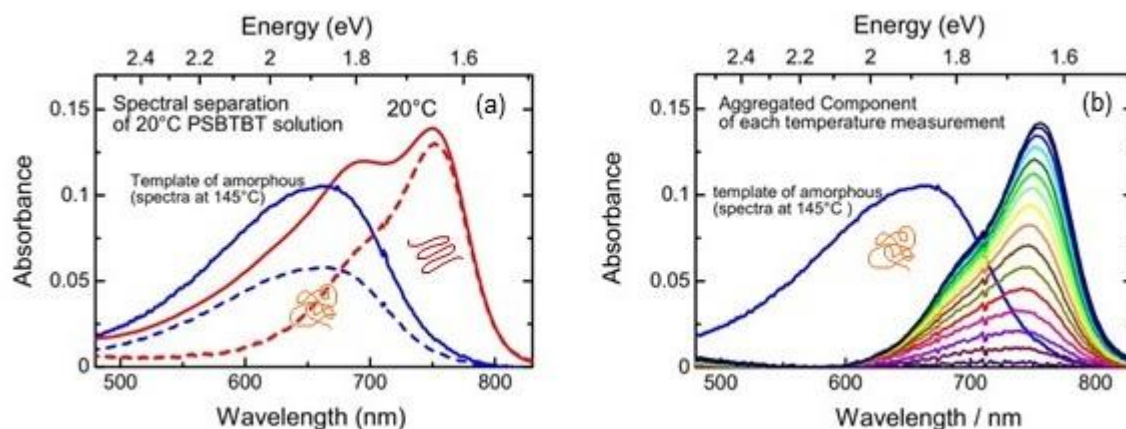
Figure A2-1. (a) An example of the spectral decomposition of PSBTBT solution measured at 20 ºC into disordered and aggregated components. (b) Absorption of aggregated components from each spectrum measured at -5 to 145 ºC (or from 145 to -5 ºC)

Figure A2-1(a) shows ~~one~~ an example of a spectral decomposition process for the PSBTBT solution. For this chapter, the PSBTBT solution absorption spectrum measured at 145 ºC (solid blue line) was used as a disordered (amorphous) template. The disordered template was used to separate the absorption two components, the disordered (blue-dashed line) and the aggregates (red-dashed line).

The same process of spectral decomposition was applied to another absorption from -5 to 145 ºC temperature measurement. The resulting spectra of aggregated component for each temperature are shown in **Figure A2-1(b)**. The intensity of the aggregated component is increasing, ~~along~~ with the decreasing measurement temperature. The change in the intensity in **Figure A2-1(b)** reflects the change in the number of aggregated chains.

The oscillator strength ~~constant~~
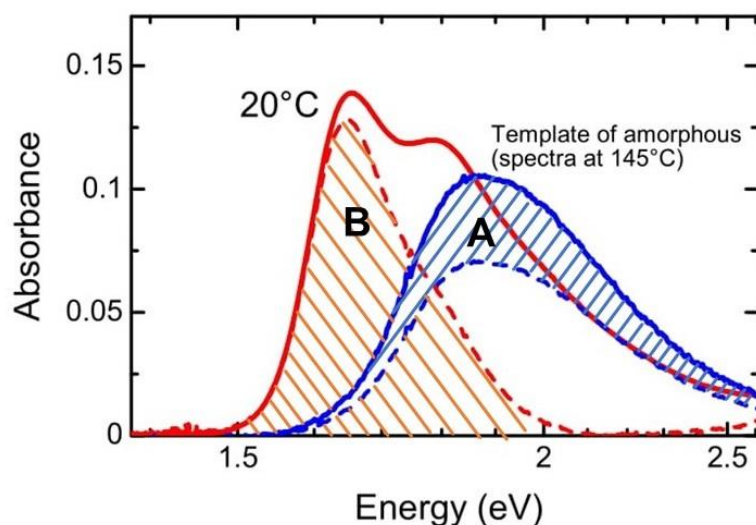
Figure A2-2. The area which represents chains transformation from disordered (A) to aggregate (B).

Figure A2-2 shows two areas that correlate with the transformed polymer chains. The solid blue and red lines are the absorption of PSBTBT solutions measured at 145 and 20 °C, respectively. The blue and red dashed lines are the absorption of the disordered and ordered component of a solid red line. If the measurement temperature were decreased from 145 to 20 °C, some disordered chains in the solid blue line became ordered in the solid red line. The number of disordered chains and ordered chains was reflected in the A and B areas, respectively.

Figure A2-2 shows that the A and B areas are different in size. The size difference of absorption indicates the different oscillator strength between two structures, disordered and ordered. The ratio of the two areas, A and B, is defined as the oscillator strength parameter:

$$F = \frac{\Delta A_{aggregate}}{\Delta A_{amorphous}}$$

Equation A2-1

The calculated value of *F* from **Equation A2-1** is 1.53. This value was then applied to the next equation (**equation A2-2**).

Fraction of aggregate
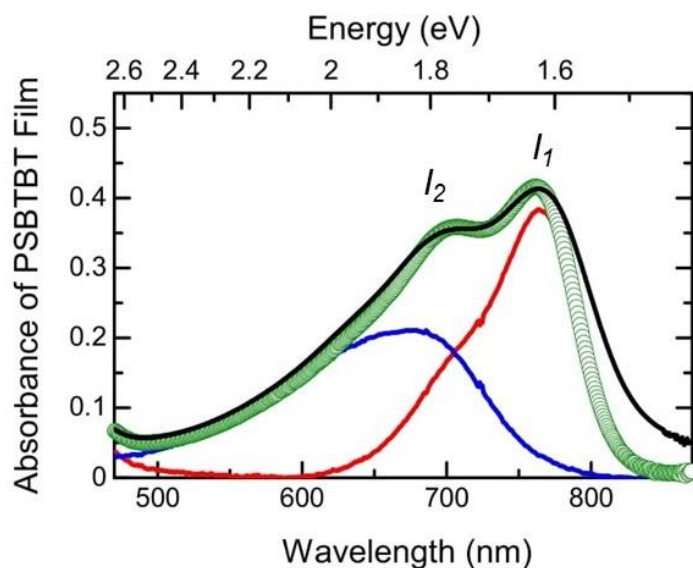
Figure A2-3. An example of spectral decomposition for PSBTBT film into the amorphous and aggregated component.

Figure A2-3 is an example of the spectral decomposition of PSBTBT film absorption by using an amorphous template. The solid black line is the real absorption of PSBTBT film. The blue and red solid lines are the amorphous and aggregated component of the film, respectively. Circle green line is the generated spectrum from both components. The area bellows the spectrum of aggregate, and amorphous components represent aggregate and amorphous chains.[2] Therefore, the relative ratio of aggregated chains to the entire chains in the film was calculated by **Equation A2-2**:

$$\text{Fraction of aggregate} = \frac{\Delta A_{\text{aggregate}}}{\Delta A_{\text{aggregate}}+1.53(\Delta A_{\text{amorphous}})} \qquad \textbf{Equation A2-2}$$

Macroscopic hole-mobility
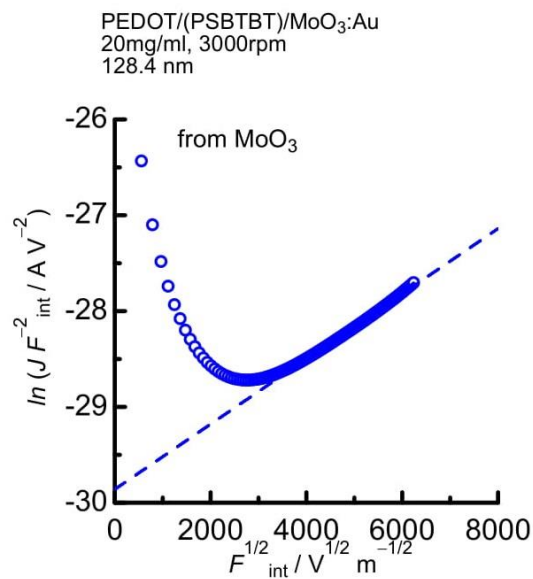
Figure A2-4. An example of a field-effect SCLC line model fitting from the J-V characteristics of PSBTBT film prepared from 20 mg/ml DCB solution spun at 3000 rpm.

Figure **A2-4** shows an example of a *J-V* fitting process to extract hole mobility from the *J-V* characteristic of PSBTBT film. For the *J-V*, the electric field effect SCLC model from **Equation 1-4.** was applied, and the value of μ_0 was obtained gamma, by:

$$J = \frac{9}{8}\varepsilon\mu_0\frac{V_0^2}{L^3}e^{\left(0.89\gamma\sqrt{E}\right)}$$ **Equation 1-4**

A3.   Appendix for Chapter 3

Absorption coefficients (α) of PCPDTBT and P3M4HT films

Figure A3-1 shows absorption coefficients (α) of PCPDTBT (solid line) and P3M4HT (broken line) neat films, spin-coated from chlorobenzene solution. The α of PS and PMMA neat films at the studied wavelength ranges (300 – 1000 nm) was negligibly small. The absorption of PCPDTBT in PCPDTBT/polymer blend films was obtained by subtracting the absorption spectrum of the matrix polymer neat film (P3M4TH, PS, or PMMA) from the total absorption spectrum of the PCPDTBT/polymer blend film. The absorption of PCPDTBT shown in **Figure 3-2(b)** and **Figure 3-8** in the main text are the results after the subtraction of the absorption of a matrix polymer.
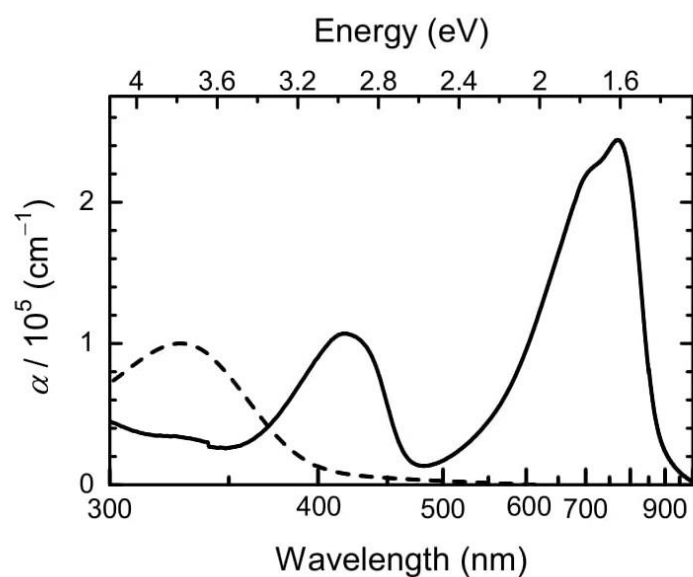
Figure A3-1. Absorption coefficients (α) of PCPDTBT (solid line) and P3M4HT (broken line) films, spin-coated from chlorobenzene solution.

Concentration dependence of the absorption spectrum of PCPDTBT in chlorobenzene
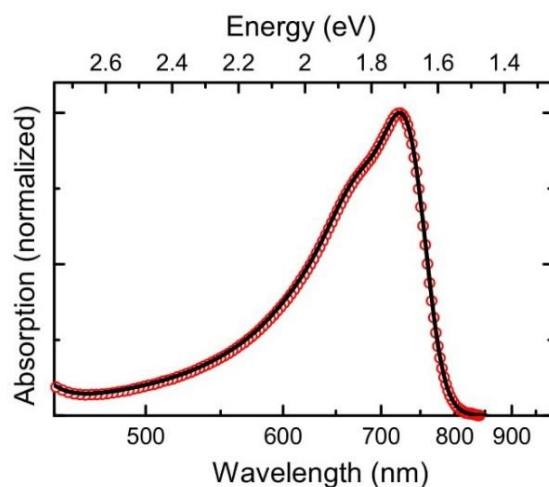
Figure A3-2. UV-vis absorption spectra of PCPDTBT in chlorobenzene solutions. The PCPDTBT concentrations shown are 0.005 mg ml^{-1} (black solid line) and 0.001 mg ml^{-1} (red open circles).

The absorption spectrum of aggregated PCPDTBT phase

In Ref. 1, Scharsich et al. obtained the absorption spectra of the aggregated PCPDTBT phase using a multi-mode Franck-Condon (FC) analysis of PCPDTBT neat film absorption.[1] The solid black line in Figure S3, the resulting absorption spectrum of the aggregated phase at 298 K in the PCPDTBT neat film spin-coated from a CB and 1,8-diiodooctane mixed solution (this data was provided from Ref. (1). The red open circles show the absorption spectrum of PCPDTBT measured for the 5 wt.% PCPDTBT/P3M4HT blend film.
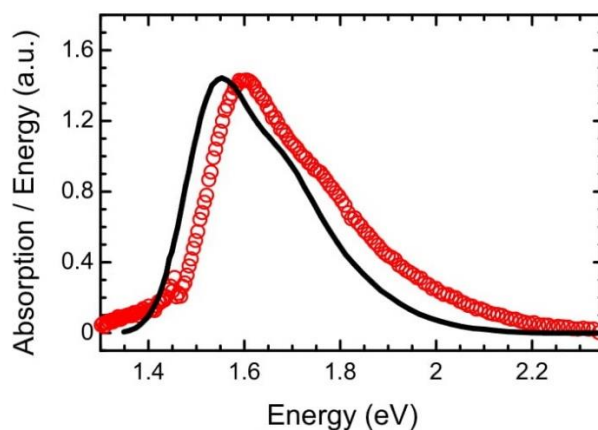
Figure A3-3. The solid black line shows the absorption spectrum of the aggregated PCPDTBT phase reported by Scharsich et al.[1] The red open circles show the absorption spectrum of PCPDTBT in the PCPDTBT/P3M4HT blend film containing 5 wt.% PCPDTBT. The absorption of PCPDTBT was obtained by subtracting the absorption of the P3M4TH from the total absorption of the PCPDTBT/P3M4HT blend film.

Spectral decomposition

The red open circles in **Figure A3-4** show the absorption spectrum of PCPDTBT that was experimentally determined for the blend films; this represents a mixture of absorption from both the disordered and the aggregated PCPDTBT phase. The solid black line shows the absorption of the aggregated PCPDTBT phase. The absorption spectrum of the aggregated phase was shifted from the original spectrum (which is reported by Scharsich et al. in Ref. (1) towards higher-energy wavelengths by 0.05 eV, such that the wavelength of its absorption peak coincided with that of the primary 770-nm peak of the PCPDTBT absorption spectrum. By referring to the absorption shape of the aggregated PCPDTBT phase, the PCPDTBT absorption spectra were separated into superpositions of absorption from the aggregated and the disordered PCPDTBT phase. Subtracting the aggregated PCPDTBT absorption (solid black line) from the PCPDTBT absorption spectrum (red open circles) gives the absorption of the disordered PCPDTBT phase, as shown by the black broken lines. In Ref. (1), Scharsich et al. have shown that the oscillator strength of the aggregated PCPDTBT chains is 1.45-times greater than the oscillator strength of the disordered PCPDTBT chains.[1] The fraction of aggregated PCPDTBT in the mixture of the disordered and the aggregated PCPDTBT was then obtained according to **Equation A3-1**, where $\Delta A_{\text{aggregate}}$ and $\Delta A_{\text{disordered}}$ are the areas below the absorption spectra of the aggregated and disordered PCPDTBT phases, respectively.

$$\text{The fraction of aggregate} = \frac{\Delta A_{\text{aggregate}}}{\Delta A_{\text{aggregate}} + 1.45(\Delta A_{\text{disordered}})} \times 100 \qquad \text{Equation A3-1}$$
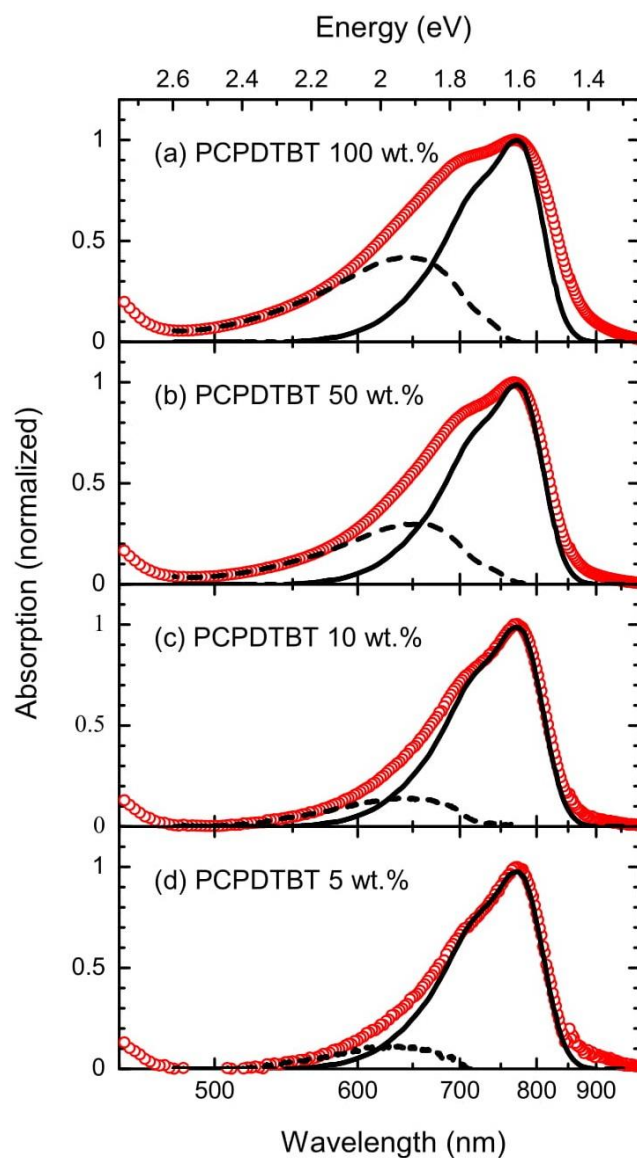
Figure A3-4. The red open circles show the absorption spectra of PCPDTBT in the PCPDTBT/P3M4HT blend films with varying amounts of PCPDTBT ranging from 100 to 5 wt.%. The absorption of PCPDTBT was obtained by subtracting the absorption spectrum of the P3M4TH from the total absorption spectrum of the PCPDTBT/P3M4HT blend film. The solid black lines show the absorption spectrum of the aggregated PCPDTBT phase reported by Scharsich et al.,[1] which was shifted by 0.05 eV from its original position towards higher-energy (i.e., shorter) wavelengths. The black broken lines show the absorption of the disordered PCPDTBT phase, as determined by subtracting the aggregated phase absorption (solid black line) from the PCPDTBT absorption (red open circles).

GIWAXS

Figures A3-5 (a) and (b) show 2-D GIWAXS images of PCPDTBT neat film and P3M4HT neat film, respectively. **Figures A3-5** (c–d) show 2-D GIWAXS images of PCPDTBT from PCPDTBT/P3M4HT blend films. These images were obtained by subtracting the background diffraction pattern containing amorphous P3M4HT from the total diffraction patterns of the blend films. 1-D profiles were then constructed for the 2-D images shown in **Figure A3-S5** (a, c–d) by integrating the intensity at each q value over an azimuth range of 70–110° for the out-of-plane profiles and 2–22° for the in-plane profiles. The spacings d were calculated from the center positions of the Lorentzian-shaped peaks q via $d = 2\pi/q$. The coherence length L_c was estimated from the Scherrer equation using the FWHM value determined from the fit and assuming the shape factor K to be 0.9. The fitting results are summarized in Tables S1 and S2. Here, the (100), (010), and (001) peaks refer to spacings d along the lamellar stacking direction, π-π stacking direction, and main-chain backbone direction, respectively.
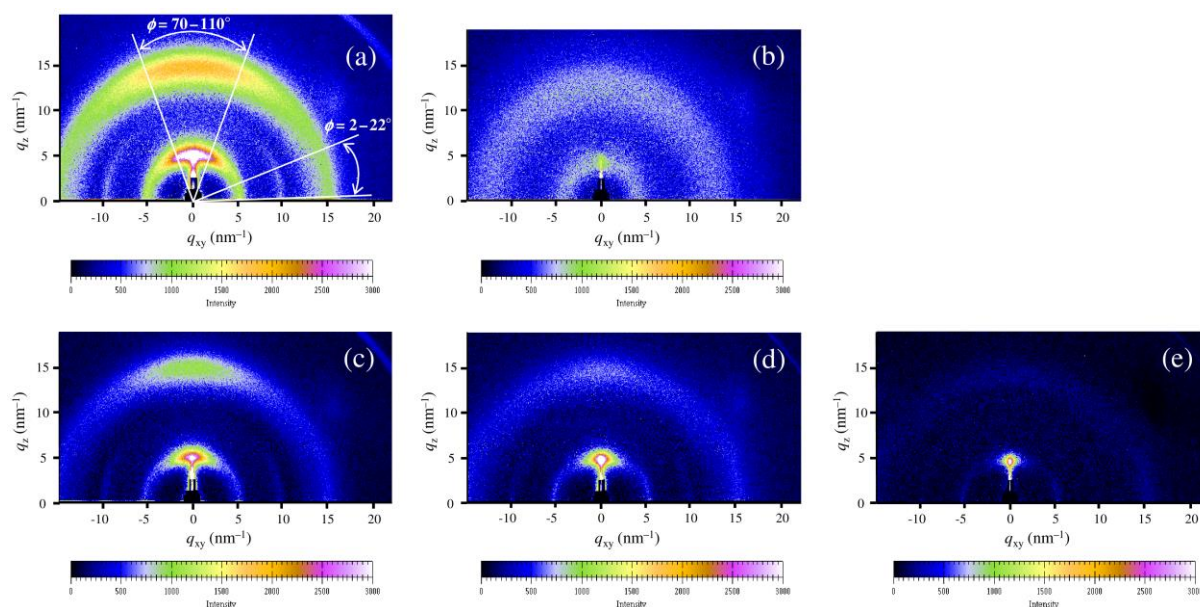
Figure A3-5. 2-D GIWAXS images of (a) PCPDTBT neat film and (b) P3M4HT neat film, and those of PCPDTBT from PCPDTBT/P3M4HT blend films containing (c) 50 wt.%, (d) 20 wt.%, and (e) 10 wt.% PCPDTBT. Out-of-plane and in-plane 1-D profiles were obtained by integrating the data from ϕ = 70 to 110° and from ϕ = 2 to 22°, respectively.

Table A3-1. Out-of-plane GIWAXS peaks for PCPDTBT in neat and blend films.

Concentration of	Index	q_z (nm^{-1})	d (nm)	FWHM	L_c
100	(100)	5.69	1.11	1.88	3.01
	(010)	16.50	0.38	3.42	1.65
50	(100)	5.64	1.12	1.69	3.35
	(010)	16.53	0.38	3.14	1.80
20	(100)	5.38	1.17	1.50	3.76
	(010)	15.96	0.39	4.27	1.32
10	(100)	5.20	1.21	1.27	4.44
	(010)	15.47	0.41	3.58	1.58

Table A3-2. In-plane GIWAXS peaks for PCPDTBT in neat and blend films.

Concentration of	Index	q_{xy}	d (nm)	FWHM	L_c (nm)
100	(001)	5.85	1.08	1.24	4.58
	(002)	10.61	0.59	1.19	4.75
	(010)	16.40	0.38	2.34	2.41
50	(001)	5.90	1.06	1.00	5.66
	(002)	10.62	0.59	1.04	5.46
	(010)	16.40	0.38	2.67	2.12
20	(001)	5.90	1.06	0.89	6.39
	(002)	10.71	0.59	0.81	7.11
	(010)	16.42	0.38	3.35	1.69
10	(001)	5.88	1.07	0.73	7.73
	(002)	10.67	0.59	0.85	6.66
	(010)	16.49	0.38	2.49	2.27

DFT calculation

We optimized the structure of PCPDTBT at ωB97XD/6-31G(d) using Gaussian16.[3] Considering the computational cost, the side chains were displaced to methyl groups. **Figure S6** shows the optimized structure of the PCPDTBT repeat unit. The length (l_a) of one repeat unit was 1.0709 nm. The highest occupied molecular orbital (HOMO) and lowest unoccupied molecular orbital (LUMO) are shown in **Figure S7**. The HOMO is spread throughout the main chain in the molecule. The LUMO is localized at 2,1,3-benzothiadiazole.

$l_a = 1.0709$ nm
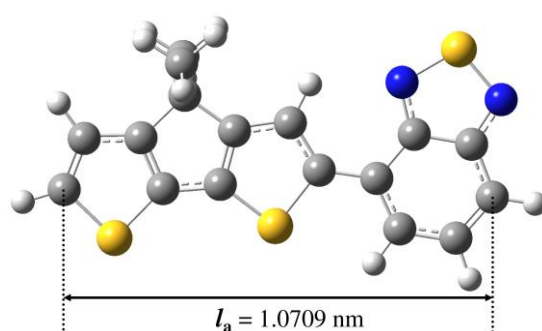
Figure A3-6. The optimized structure of the PCPDTBT repeat unit.

(a)   (b)
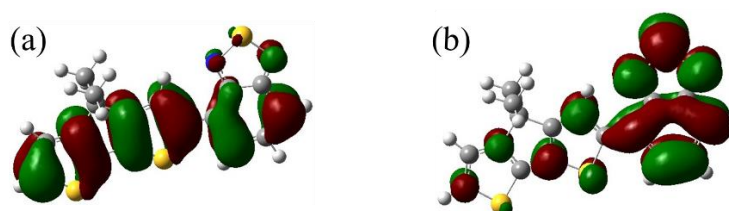
Figure A3-7. Molecular orbitals of PCPDTBT (a) HOMO (b) LUMO.

Comparation between PCPDTBT/ADS406PT and PSBTBT/ADS406PT

(a)

(b)
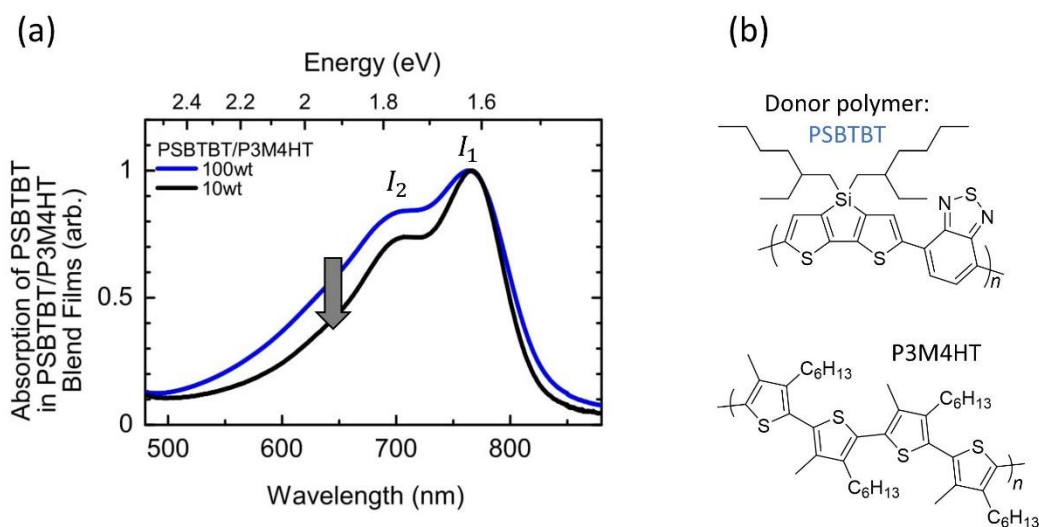
Figure A3-8. UV-visible spectra of, PSBTBT/P3M4HT

Figure A3-8 shows the UV-vis spectra of PSBTBT/P3M4HT blend films. The decrease in shorter wavelength indicates the decrease in amorphous contribution, which consequently increasing aggregate contribution by blending.

AFM images
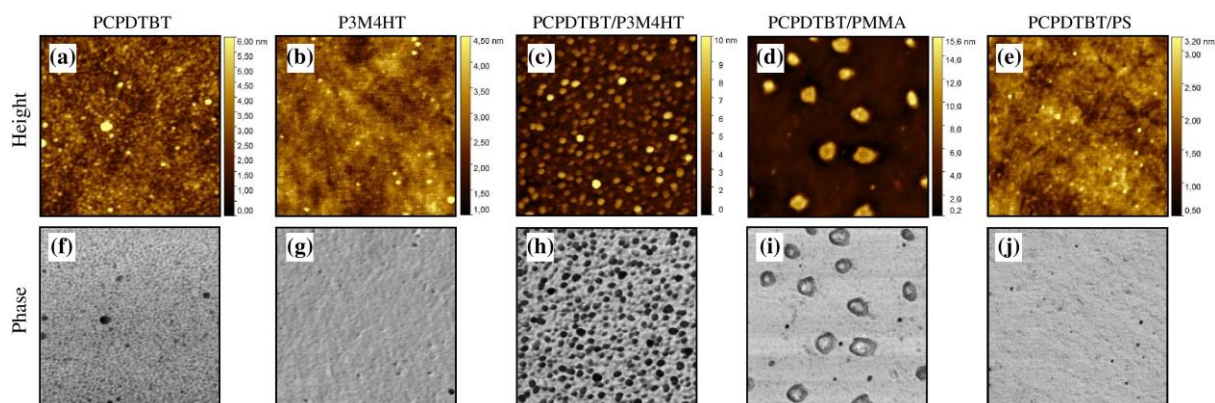
Figure A3-10. Tapping-mode AFM topographical (a-e) and phase (f-j) images (4 μm × 4 μm) of neat and blend films spin-coated from DCB solution. Neat films of PCPDTBT (a, f) and P3M4HT (b, g). 10 wt.% of PCPDTBT blend films with P3M4HT (c, h), PMMA (d, i), and PS (e, j).

A4. Appendix for Chapter 4

GIWAX results for PCBM, di-PDI, and PDI-2T

Table A4-1. GIWAXS results for PCBM, di-PDI, and PDI-2T films.

Film	Index	q (nm^{-1})		d (nm)		L_c (nm)	
		in-plane	out-of-plane	in-plane	out-of-plane	in-plane	out-of-plane
PCBM	1st	7.25	7.22	—	—	—	—
	2nd	13.90	13.95	—	—	—	—
	3rd	20.35	20.53	—	—	—	—
di-PDI	1st	3.35	—	1.88	—	3.31	—
	2nd	14.10	14.58	0.45	0.43	0.69	0.83
P(PDI-2T)	(100)	2.81	—	2.24	—	3.57	—
	(001)	5.10	4.96	1.23	1.27	2.54	1.64
	(010)	14.10	14.44	0.45	0.44	1.01	0.95

Reference of the appendices

(1)   Scharsich, C.; Fischer, F. S. U.; Wilma, K.; Hildner, R.; Ludwigs, S.; Köhler, A. Revealing Structure Formation in PCPDTBT by Optical Spectroscopy. J. Polym. Sci. Part B, Polym. Phys. **2015**, *53* (20), 1416–1430. https://doi.org/10.1002/polb.23780.

(2)   Clark, J.; Chang, J.; Spano, F. C.; Friend, R. H.; Silva, C. Determining Exciton Bandwidth and Film Microstructure in Polythiophene Films using Linear Absorption Spectroscopy. Appl. Phys. Lett. **2009**, *163306* (94). https://doi.org/10.1063/1.3110904.

(3)   Frisch, M. J. et al. *Gaussian 16 A.01*; Gaussian, Inc.: Wallingford, CT, 2009.